12-1997

Volcanology and Geochemistry of Pliocene and Quaternary Basalts on Citadel Mountain, Lunar Crater Volcanic Field, Pancake Range, Nevada

Loretta D. Dickson
University of Nevada, Las Vegas

Repository Citation

Dickson, Loretta D., "Volcanology and Geochemistry of Pliocene and Quaternary Basalts on Citadel Mountain, Lunar Crater Volcanic Field, Pancake Range, Nevada" (1997). *UNLV Theses, Dissertations, Professional Papers, and Capstones*. 1118.
http://dx.doi.org/10.34917/2494294

Volcanology and Geochemistry of Pliocene and Quaternary Basalts on Citadel Mountain, Lunar Crater Volcanic Field, Pancake Range, Nevada

by Loretta D. Dickson

A thesis submitted in partial fulfillment
of the requirements for the degree of

Master of Science

in

Geoscience

Department of Geoscience
University of Nevada, Las Vegas
December 1997

The thesis of Loretta D. Dickson for the degree of Master of Science in Geoscience is approved.

Chairperson, Eugene I. Smith, Ph.D.

Examining Committee Member, Rodney V. Metcalf, Ph.D.

Examining Committee Member, Terry L. Spell, Ph.D.

Graduate Faculty Representative, Steven Lepp, Ph.D.

Dean of the Graduate College, Ronald Smith, Ph.D.

University of Nevada, Las Vegas
December 1997

ABSTRACT

Alkali basalts on Citadel Mountain form the southern margin of the Lunar Crater Volcanic Field (LCVF) in the central Great Basin, Nevada. Citadel Mountain comprised of a faulted, north tilted section of Tertiary andesite and ash-flow tuff is capped by Pliocene and Quaternary alkali basalt flows that erupted from six major cinder cones. The basalt flows on Citadel Mountain can be divided into two groups (older and younger) based on age and isotopic signatures. The older basalt group is characterized by higher $^{87}Sr/^{86}Sr$ and lower ε_{Nd} and the younger group has lower $^{87}Sr/^{86}Sr$ and higher ε_{Nd}. Geochemical evidence suggeststhat the older basalt group is contaminated by a lithospheric mantle melt. A model is presented that shows contamination of the older alkali basalts by magma commingling/mixing of rising asthenospheric melts with lithospheric mantle veinlets in the mantle lithosphere. Fractional crystallization of olivine and clinopyroxene can explain the chemical variation in the older basalt group, and although small amounts of assimilation of upper crustal material are permissible, assimilation is not required in the models. The younger basalt group evolved solely by fractional crystallization of olivine and clinopyroxene and their isotopic signatures may reflect their asthenospheric mantle source.

TABLE OF CONTENTS

LIST OF FIGURES

LIST OF TABLES

CHAPTER 1

INTRODUCTION

Knowledge of small volume (<150 km^3) mafic volcanic fields is limited. Although the petrogenetic history of many of these fields has been studied, few geochemical studies focus on the evolution of individual volcanoes or the detailed history of entire fields. Expressing mafic volcanic systems as "small" may imply they are simple in nature, however, recent studies have shown that small volume mafic volcanic fields in the Basin and Range of the western U.S. are quite complex. For example, the Pliocene Crater Flat volcanic field, Nevada (Figure 1), a complex polycyclic and polygenetic system, evolved by the mixing of at least two mafic magmas. Red Cone, one of the volcanoes in the field, erupted lavas that represent the entire range of composition between the two mafic magmas (Bradshaw et al., 1994). The Sunset Crater Volcanic Chain (SCVC), Arizona (Figure 1) is a complex monogenetic volcanic system where older and younger groups of alkali basalts formed by different degrees of contamination by lower crustal mafic granulites, and by clinopyroxene and olivine fractionation (Blaylock et al., 1996). Mafic volcanism in the Reveille Range, Nevada (Figure 1) is also complicated and comprised of two episodes of basalt, the earliest episode having a history of carbonate assimilation while the later does not (Yogodzinski et al., 1996).

This thesis uses stratigraphy and geochemistry to determine magmatic processes and chemical evolution of mafic volcanic rocks in the Lunar Crater Volcanic Field (LCVF), a small volume alkali basalt volcanic field in the central part of the Great Basin (Figure 1). The LCVF is a 100 km long north-northeast trending belt of Pliocene to Recent alkali basalt cinder cones, maar craters and lava flows which extends across the Pancake and Reveille Ranges in Nye County, central Nevada (Trask, 1969; Scott and Trask, 1971; Bergman, 1982) (Figure 2). The total estimated volume of alkali basalt cinder cones and flows for the entire 100 km long LCVF is 100 km^3 (Bergman, 1982). This study focuses on alkali basalts on Citadel Mountain in the southern Pancake Range in the northern part of the LCVF. Specifically, the thesis area covers 150 km^2 and includes volcanic centers on and around Citadel Mountain (Figure 2). Citadel Mountain is an ideal location to study chemical variation of mafic volcanism because lava flows and their vent areas are well exposed; therefore providing the unique opportunity to trace lava flows to their vents and to establish the volcanic stratigraphy.

Although small in volume, the LCVF is one of the largest Pliocene to Recent volcanic fields in the Great Basin and is the site of some of the most recent volcanic activity. Because the lavas from individual cinder cones reflect comagmatic systems (see Chapter 5 and 6), the abundance of cinder cones in the LCVF provides an extensive data set to evaluate the chemical evolution of magma chambers with time. Lavas erupted from cinder cones are also used as probes into the mantle. Traditionally, alkali basalt magma is assumed to rise from its mantle source through the crust and to the surface without significant modification, yet this assumption has not been rigorously tested. This thesis will provide data that may help validate or invalidate the use of alkali basalt as mantle probes.

Several studies (Perry et al., 1987; Lum et al., 1989; Farmer et al., 1989; Daley and DePaolo, 1992; Feuerbach et al., 1993) focus on the role of the lithospheric and asthenospheric mantle and crustal contamination in producing alkali basalt magmas in the western United States. This study also addresses fundamental questions that pertain to the role of lithospheric and asthenospheric mantle in the petrogenesis of basaltic magma and changing mantle source of volcanic rocks with time. Using the chemistry and isotopic composition of continental basalts, characteristics of magma sources beneath the central Great Basin can be determined. Combining mantle source data with stratigraphy and the age of volcanic rocks constrains the timing of transitions from a lithospheric to an asthenospheric mantle source. Once this is accomplished, any correlation of mantle source transitions with extensional periods can be explored.

Another important reason for studying small volume mafic volcanic fields is to evaluate the hazard and risk associated with cinder cone eruptions. Many small volume mafic volcanic fields are located near populated regions or major transportation routes. Cinder cone eruptions may affect the safety of communities and domestic travel along major highways, railways and air travel routes. U.S. Highway 6, a major route between the Nevada towns of Ely and Tonopah, runs directly through the Pancake Range between sites of recent eruptions dated at 500 ka and 38 ka (Foland and Bergman, 1992; Shepard et al., 1995). Volcanic hazards are greatest in the western U.S., Hawaii, Mexico and Iceland as these areas are prime locations for future cinder cone eruptions (Simkin et al., 1981).

In summary, the purpose of the thesis is to determine the volcanic stratigraphy of the Pliocene and Quaternary lava flows on Citadel Mountain, to evaluate chemical variation of basaltic rocks with time, to examine the role of the lithospheric mantle and asthenospheric mantle in the petrogenesis of basaltic magma, and to identify and determine the timing of any mantle source transitions.

Geologic Background

Basaltic magmatism occurs along the margins and in the center of the Great Basin. Volcanic fields along the margins of the Great Basin are represented by the Big Pine Volcanic Field, California to the west and the Hurricane Volcanic Field, Utah (Figure 1) to the east. A north-northeast trending belt of mafic volcanism referred to as the Death Valley-Pancake Range Basalt Zone (Vaniman et al., 1982; Farmer et al., 1989) (Figure 3) is Pliocene to Recent in age and occurs along the axis of the Great Basin. The belt extends from Death Valley in the south through Crater Flat and the Reveille Range to the Pancake Range in the north. Small volume basaltic volcanism began at Crater Flat in the late Miocene to early Pliocene and ended with five cinder cones, Quaternary in age, aligned along NE-SW trending fault zones (Bradshaw et al., 1994). To the northeast of Crater Flat, Quaternary basalt (2.7 Ma) of Buckboard Mesa erupted mainly from a cinder cone but also from a 5 km long fissure (Crowe et al., 1995). Farther north, basaltic volcanism in the Reveille Range began at 14 Ma and continued until 3 Ma.

In the Pancake Range at the northern end of the belt, Proterozoic crystalline basement is overlain by a thick section of Paleozoic carbonate and clastic rocks (Lum et al., 1989). Oligocene and Miocene ash-flow tuffs that overlie the Paleozoic sedimentary sequences vary in composition from rhyolite to dacite (Ekren et al., 1972). Alkali basalts in the LCVF (Reveille and Pancake Ranges) erupted on this thick crustal assemblage during the Pliocene to late Quaternary and cover an area of more than 259 km^2 (Scott and Trask, 1971; Bergman, 1982; Lum et al., 1989; Foland and Bergman, 1992).

The Pliocene to Recent LCVF is composed of three maar volcanoes, 75 cinder cones and associated basaltic lava flows (Scott and Trask, 1971; Foland and Bergman, 1992). The LCVF has a vent density (3.45 vents/km^2) that is one of the highest in the world for basaltic volcanic fields, and it sits on the thinnest crust (25-30 km) in the western U.S. (Crowe et al., 1992). The youngest eruption (38 ka) in the LCVF produced the Marcath flow just to the north of U.S. Highway 6 (Trask, 1969; Scott and Trask, 1971; Shepard et al., 1995) (Figure 4). As suggested by Foland and Bergman (1992) volcanism migrated to the northeast in the LCVF. It began at 14 Ma in the Reveille Range to the south, averages about 4 Ma in the central LCVF (Rash, 1995 and this study) and terminates at 38 ka with the Marcath flow in the northern Pancake Range (Shepard et al., 1995).

The structural control of volcanism in the LCVF has been debated in previous studies. Many of the cinder cones form chains that appear to be controlled by northeast striking high-angle normal faults (Scott and Trask, 1971; Ekren et al., 1972), although structural control by caldera margins was also proposed (Ekren et al., 1974). The boundaries of the Lunar Lake caldera were located by geophysical (gravity, aeromagnetic, reflection seismographic) techniques (Ekren et al., 1974), however, structural control by caldera margins is difficult to evaluate because the proposed caldera is entirely buried by younger volcanic rocks. Crowe et al. (1992) concluded that vent locations of cinder cone clusters in the LCVF are strongly structurally controlled by northeast striking faults.

Citadel Mountain in the southern Pancake Range, a 9.3 km long north-tilted fault block comprised of Tertiary andesite and the Tuff of Buckwheat Rim is bounded on the south by a high-angle normal fault (Figure 5). The Tertiary andesite unit is Miocene in age and comprised of andesite lavas and flow breccias. Thirteen Pliocene and Quaternary basaltic cinder cones and associated lava flows produced over a three million year period are distributed from the top to the base of Citadel Mountain. The stratigraphy and chemistry of the lavas associated with these cinder cones are the primary focus of this thesis.

Distributed to the north and east of Citadel Mountain are three maar volcanoes (Figure 4). They include Lunar Crater maar, Easy Chair Crater maar and Lunar Lake maar. Lunar Crater and Easy Chair Crater are approximately 1.2 km and 0.5 km in diameter, respectively. Lunar Lake maar is 0.4 km in diameter. The three maars have steep inward facing slopes with country rock exposed on the crater walls. Three lava flows are exposed in the Lunar Crater maar above the Tuff of Buckwheat Rim. The rim of Easy Chair Crater maar is formed by surge deposits exposed on the steep inward facing walls. Each crater is surrounded by a deposit of country rock ejecta and pyroclastic deposits but no juvenile magma is associated with the maar eruptions. The floors of the craters are lower than the surrounding topography. All three exhibit progression in eruptive style from cinder cone to maar volcano. In each case, maar eruptions produced craters on the flanks of the pre-existing cinder cones.

Previous Work

Vitaliano and Harvey (1965) completed some of the earliest work in the LCVF and focused their studies on the petrography and mineralogy of the Marcath Flow in the northern part of the volcanic field. Scott and Trask (1971) made contributions to extraterrestrial research by using the LCVF as a terrestrial analog to craters and cones on the moon. They concentrated their studies on the morphology of the volcanic cones and lava flows and to a lesser extent on the petrography, stratigraphy, and geochemistry. Ekren et al. (1972) mapped the Lunar Crater quadrangle at a scale of 1:48,000. Ekren et al. (1974) later discussed the geologic history of the Lunar Lake caldera. Ekren proposed that the Lunar Lake caldera is the youngest caldera in the multiple cauldron complex of the central Nevada volcanic field. Bergman et al. (1981) focused on the origin of a mantle-derived peridotite nodule bearing an amphibole-rich vein from the Marcath flow, and later, Bergman (1982) discussed the general geology and petrology of the LCVF. Lum (1986) inferred the lithology and chemistry of the mantle beneath the LCVF by examining the basalt flows and ultramafic nodules. Kargel (1987) searched for genetic relationships between LCVF lavas and their mantle inclusions and compared mantle composition beneath the LCVF to the mantle beneath other parts of the Great

Basin. Lum et al. (1989) included LCVF basalts in a study questioning whether isotopic diversity in late Cenozoic basalts is caused by crustal contamination of magma during ascent or if such diversity reflects mantle heterogeneity. Foland et al. (1991) used oxygen isotopes to identify crustal contamination as a process involved in the petrogenesis of basaltic magma in the LCVF; he concluded that most of the magmas had been contaminated but failed to identify a contaminant. Foland et al. (1991) suggested that the only magmas not affected by crustal contamination were magmas that had short transit times through the crust. Most recently, Shepard et al. (1995) obtained ^{36}Cl and ^{10}Be cosmogenic exposure ages of two basalt flows in the LCVF. They dated the Black Rock flow (Marcath flow) in the northern LCVF at 38.1 ± 9.7 ka and the Lunar Crater flow (their unofficial designation due to the flow's proximity to Lunar Crater maar) at 600 ka.

Summary of Conclusions

The major contributions of this thesis are:

- Detailed stratigraphy of alkali basalt flows on Citadel Mountain is firmly established (Chapter 2).
- New ^{40}Ar/^{39}Ar dates for 4 flows on Citadel Mountain are presented (Chapter 2).
- A cinder cone, scoria-dike complex and two spatter ramparts discovered during field studies are described in detail along with new field evidence suggesting alternating Strombolian and Hawaiian style activity (Chapter 3).

- Three magma groups were identified that correspond to lava flows from individual cinder cones or closely spaced cinder cones (P1 and H-cone, C and R-cone and Qc and Lunar Crater cone (Chapter 5).
- The three magma groups defined by trace elements are divided into two groups of basalt with similar age and isotopic signatures. The older basalt group is characterized by higher $^{87}Sr/^{86}Sr$ and lower ε_{Nd} than the younger group which is typified by lower $^{87}Sr/^{86}Sr$ and higher ε_{Nd} (Chapter 5).
- Two contamination events may have affected the older basalt group; one event occurring in the lithosphere by magma commingling/mixing of rising asthenospheric melts with entrained melts in the lithospheric mantle and another possible event occurring near the surface during fractional crystallization (Chapter 6).
- The younger basalt group evolved solely by fractional crystallization and their isotopic ratios may reflect their asthenospheric mantle source (Chapter 6).
- The timing of a mantle source transition from a lithospheric to an asthenospheric mantle source for alkali basalts is constrained to have occurred between 21.79 Ma and 3.82 Ma (Chapter 7).
- Randomly collecting alkali basalts from a volcanic field without first understanding its stratigraphy and geochemistry is risky, because samples may be contaminated and magma commingling/mixing may alter isotopic ratios and fractional crystallization may change trace element signatures. In the LCVF, only the youngest lavas and those with ultramafic nodules directly reflect the isotopic and chemical composition of their mantle source (Chapter 8).

- A future eruption in the LCVF will likely occur in the vicinity of the Marcath flow in the northern Pancake Range. Based on the size and geometry of Quaternary and Recent lava flows, it is possible that U.S. Highway 6, a major transportation route through the Pancake Range, may be disrupted in the event of a future eruption (Chapter 8).

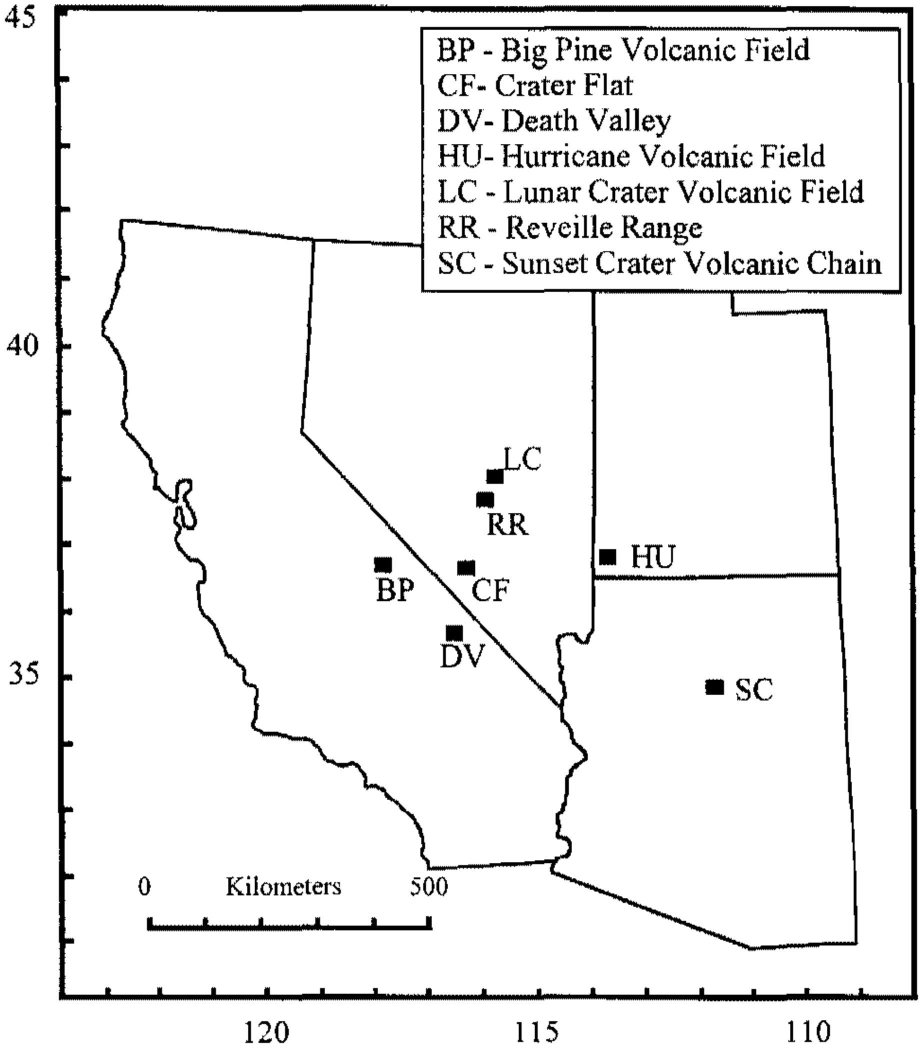

Figure 1. Map of the western United States showing the location of small volume mafic volcanic fields.

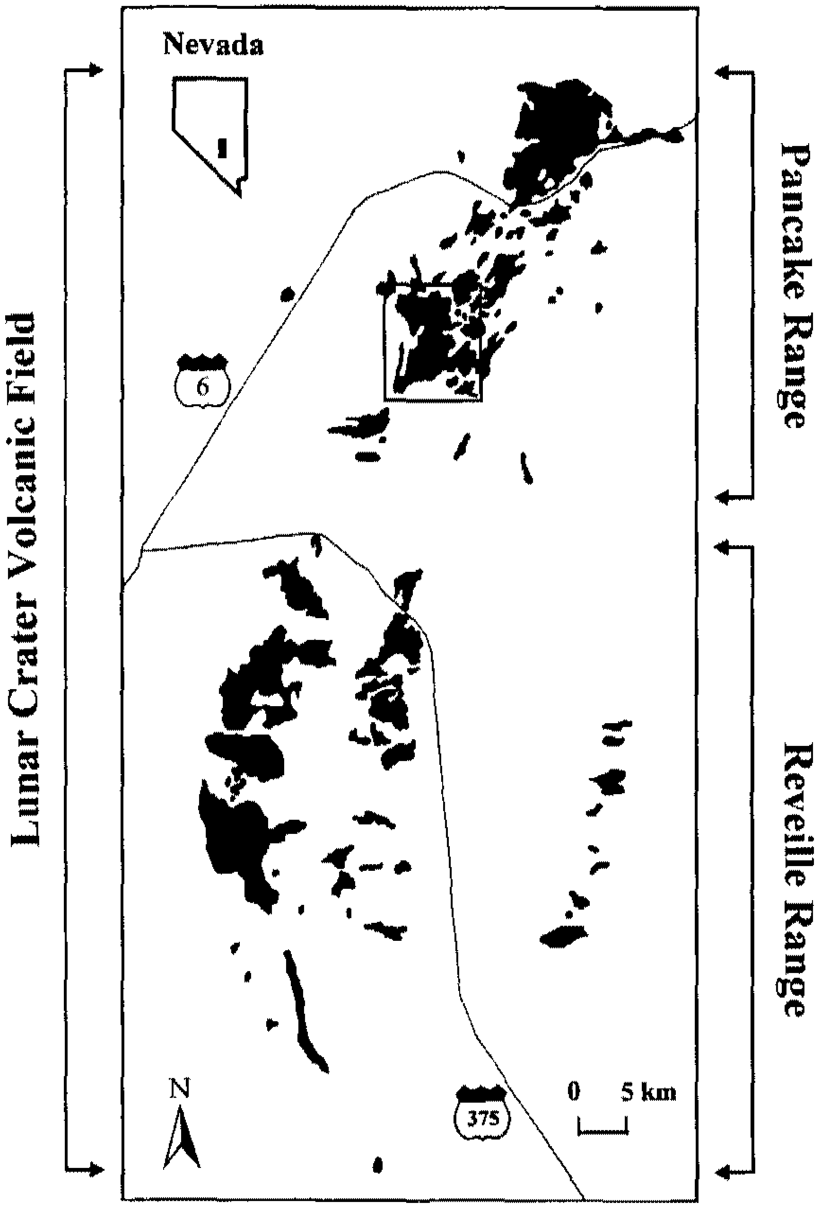

Figure 2. The 100 km long Lunar Crater Volcanic Field (LCVF) is divided into the Reveille Range in the south and the Pancake Range in the north. The location of Citadel Mountain in the southern Pancake Range is indicated by the box. Map is modified after Foland and Bergman (1992).

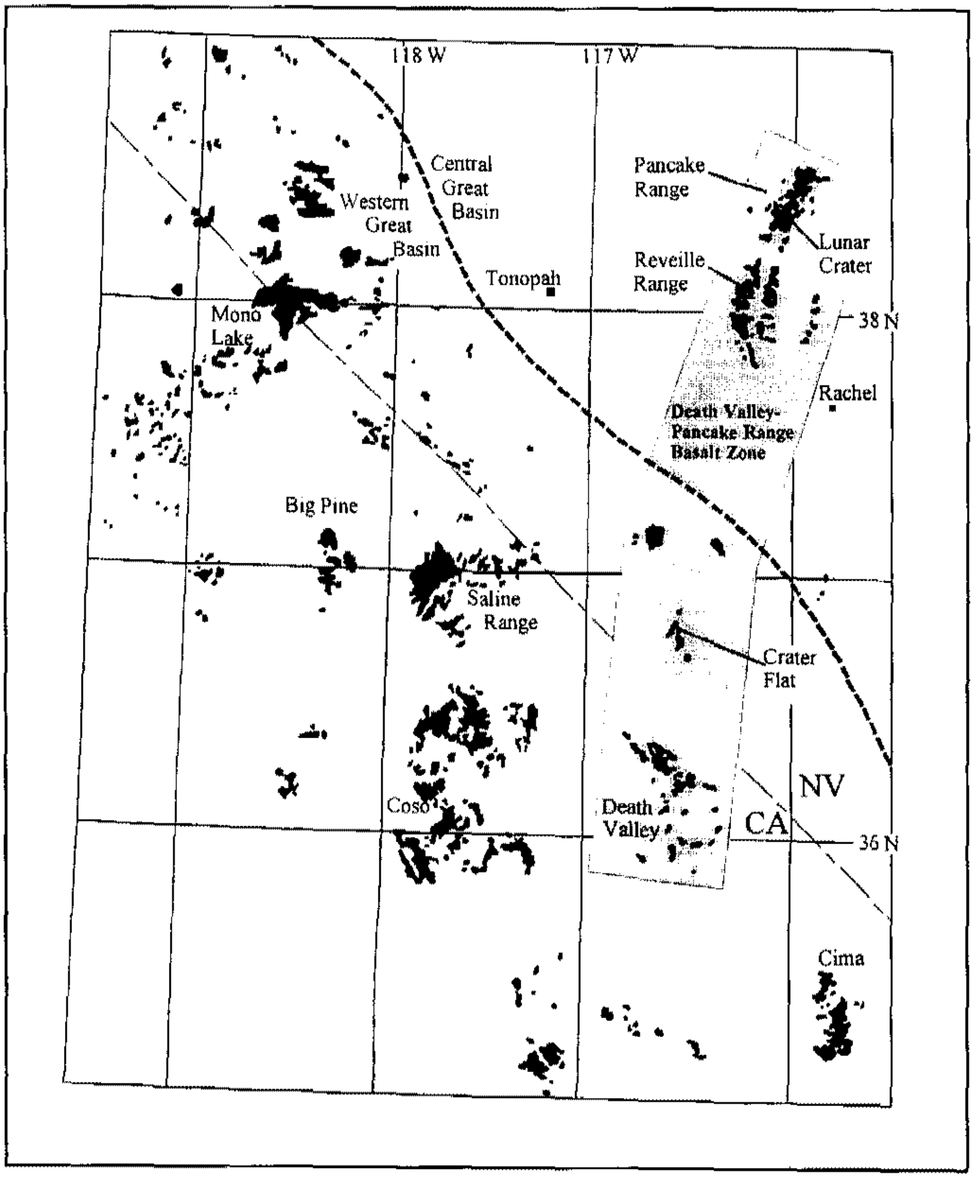

Figure 3. Location of mafic volcanic fields (in black) in the western and central Great Basin that are less than approximately 8 Ma. Highlighted is the Death Valley-Pancake Range Basalt Zone from Yogodzinski et al. (1996).

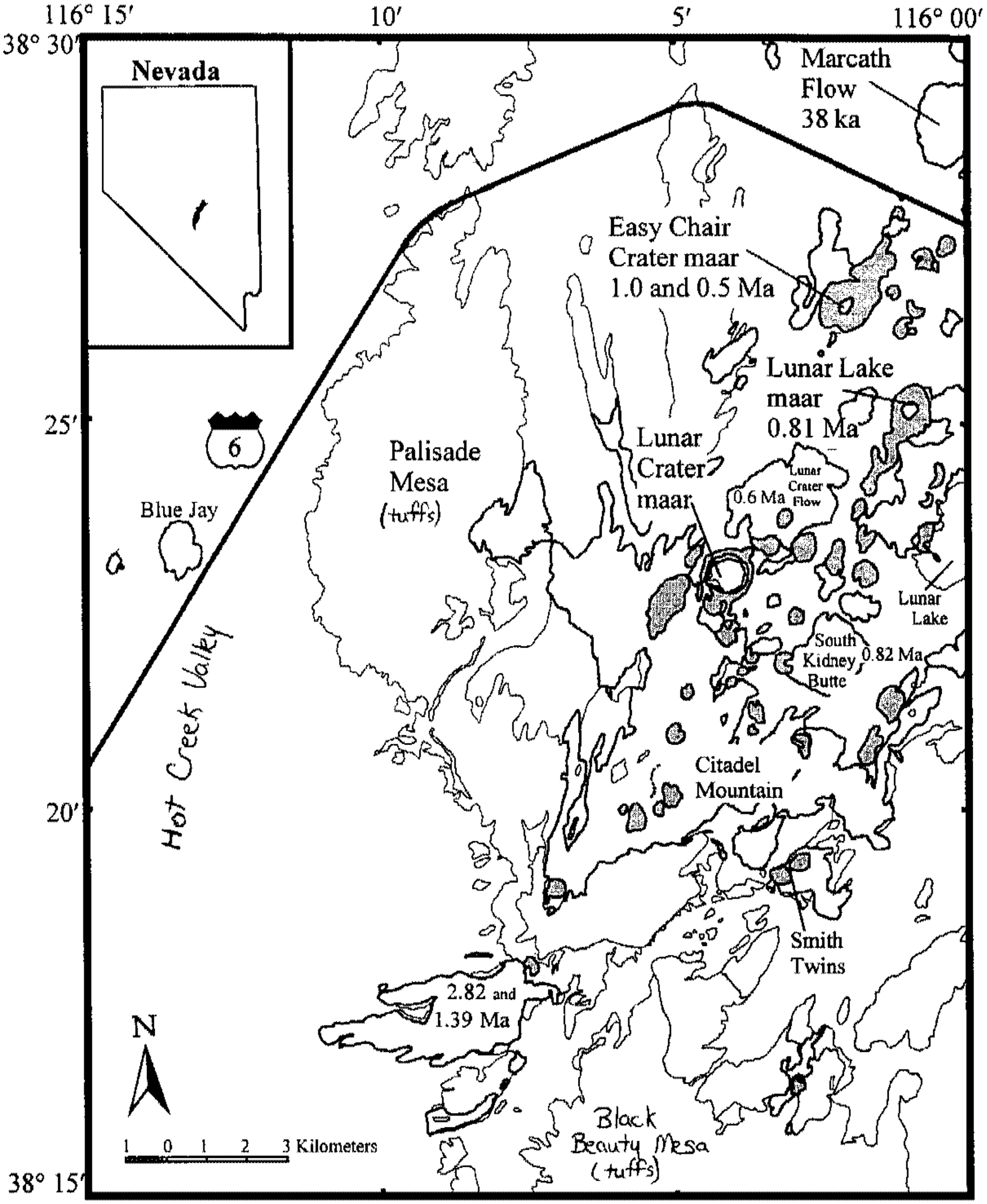

Figure 4. Index map shows the location of Lunar Crater maar, Easy Chair Crater maar and Lunar Lake maar. Map also shows location of the youngest flows in the LCVF; the Marcath Flow, flows associated with Easy Chair Crater and Lunar Lake maar, the South Kidney Butte flow, and flows erupted from a cone just below the escarpment forming the southern edge of Citadel Mountain: (from Ekren et al., 1972). Ages of the flows are discussed in Chapter 2.

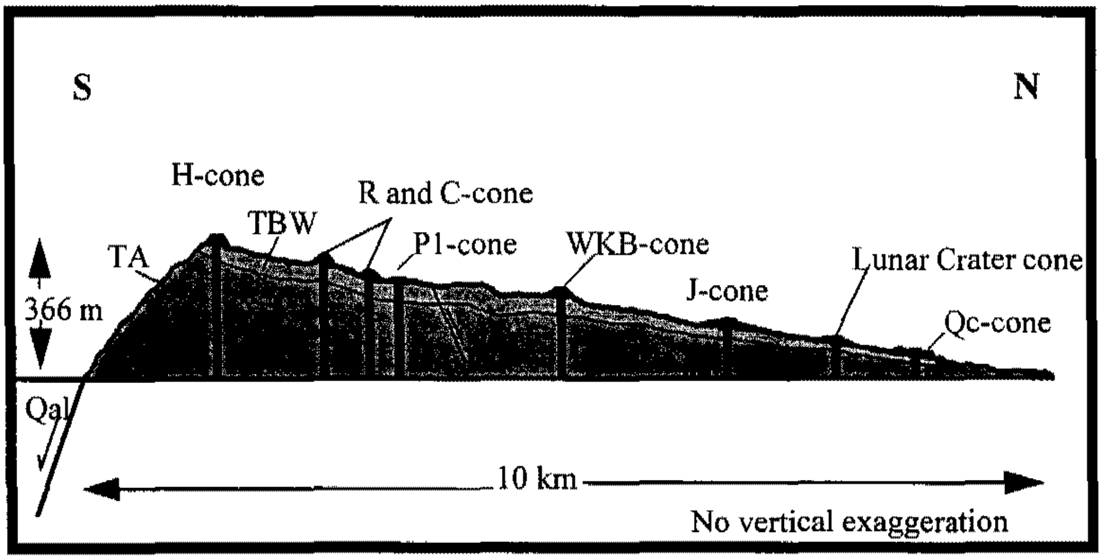

Figure 5. Cross-section shows the north-tilted Citadel Mountain fault block comprised of Tertiary andesite (TA) and the Tuff of Buckwheat Rim (TBW). Basaltic cinder cones erupted through the Tertiary andesites and are distributed from the top to the base of the mountain.

CHAPTER 2

SEQUENCE OF EVENTS AND GEOCHRONOLOGY

The stratigraphy presented in this chapter was established during field studies on Citadel Mountain and represents the first detailed stratigraphy for any area of the LCVF. The cinder cones on and around Citadel Mountain were assigned letter, or letter and number designations for identification purposes (Figure 6). Units are described below from oldest to youngest (Figure 7). The volcanology of each unit is presented in Chapter 3 and petrography in Chapter 4. Geochronology data is tabulated on Table 1 and discussed in Appendix C.

The P1-cone erupted at 3.82 ± 0.06 Ma (Table 1) from a scoria-dike complex in the southern part of Citadel Mountain (Figure 8; Plate 1). The P1-cone flow covered 4.5 km^2 flowing to the north down the dip slope of Citadel Mountain to the future site of the Lunar Crater maar. The P1-cone flow is the stratigraphically lowest basalt flow exposed in the Lunar Crater maar. The P1-cone flow is 5-6 m thick and sits directly on exposures of Tuff of Buckwheat Rim. It provided a platform on which most of the other cinder cones and flows erupted.

The H-cone (Figure 9; Plate 1) formed at the high southernmost point on Citadel Mountain at 3.82 ± 0.05 Ma (Table 1); concurrent with the P1-cone. The age and chemistry of H-cone are first reported in this study. Flows from H-cone extend 4.8 km to the north and locally cascade over tuff on the western side of the mountain (see Chapter 3, Figure 17). H-cone is rather inconspicuous on aerial photographs compared to other cinder cones on Citadel Mountain; likely due to the lighter color of the rocks comprising the cone. In contrast, aerial photographs show the H-cone flow in bold detail compared to other flows on Citadel Mountain. A possible explanation for slightly bolder relief of H-cone flows is that H-cone basalt has the highest silica content of all the flows on the mountain (see Chapter 5) and may have been more viscous during eruption.

The Lunar Crater cone (Figure 10; Plate 1) erupted at 2.97 ± 0.06 Ma (Table 1). Lava from the Lunar Crater cone flowed approximately 1 km to the northeast and 2 km to the southwest. The Lunar Crater flow also covered the future site of the Lunar Crater maar and is now the middle flow exposed in the crater.

Qc-cone flows (Figure 11; Plate 1) extend to the north, west and east of their four vents that make up the Qc-cone cluster. Lava from Qc-cone flowed to the northeast and overlies the Lunar Crater flow and the P1-cone flow. The Qc-cone flows also covered the area of the Lunar Crater maar and are now the top flows exposed in the crater. The Qc-cone flow to the northwest of the vent was dated at 1.64 ± 0.14 Ma (K/Ar whole rock date; Kargel, 1987) (Table 1).

C-cone flows (Figure 12; Plate 1) extend 6 km to the northeast and east of the cone and cascade over exposures of tuff. The C-cone flows overlie the P1-cone flow and the

Tuff of Buckwheat Rim. The C-cone was dated at 1.15 ± 0.14 Ma (K/Ar whole rock date; Kargel, 1987) (Table 1).

R-cone (Figure 13; Plate 1) erupted at 0.66 ± 0.34 Ma (Table 1). Its flows extend to the north 2.5 km and flow down the same channel used by H-cone flows. R-cone flows cover the P1-cone flow, H-cone flow and exposures of the Tuff of Buckwheat Rim.

Other cinder cones on and around Citadel Mountain range in age from cones that are older than the C-cone to cones younger than the R-cone. A chain of 4 cinder cones, the 4G-cones are aligned to the northeast and may be older than C-cone (1.15 ± 0.14 Ma; Kargel, 1987) (Figure 6; Plate 1). This age relationship is suggested because C-cone lava flows on either side of the 4G-cones chain. Flows erupted from a cone just below the escarpment forming the southern edge of Citadel Mountain are dated at 2.82 ± 0.22 Ma and 1.39 ± 0.07 Ma (K/Ar whole rock date; Kargel, 1987) (see Chapter 1, Figure 4; Plate 1). Flows from the cone associated with Easy Chair Crater were dated at 1.0 and 0.5 Ma (K/Ar whole rock date; Foland and Bergman, 1992) and flows from the cone associated with Lunar Lake maar were dated at 0.81 ± 0.06 Ma (K/Ar whole rock date; Kargel, 1987) (Plate 1). South Kidney Butte (2.82 km^2) is dated at 0.82 ± 0.06 Ma (K/Ar whole rock date; Dohrenwend et al., 1987) (see Chapter 1, Figure 4; Plate 1).

Although volcanism in the LCVF generally becomes younger to the northeast with time (Foland and Bergman, 1992) this temporal migration is not recognized at the scale of Citadel Mountain.

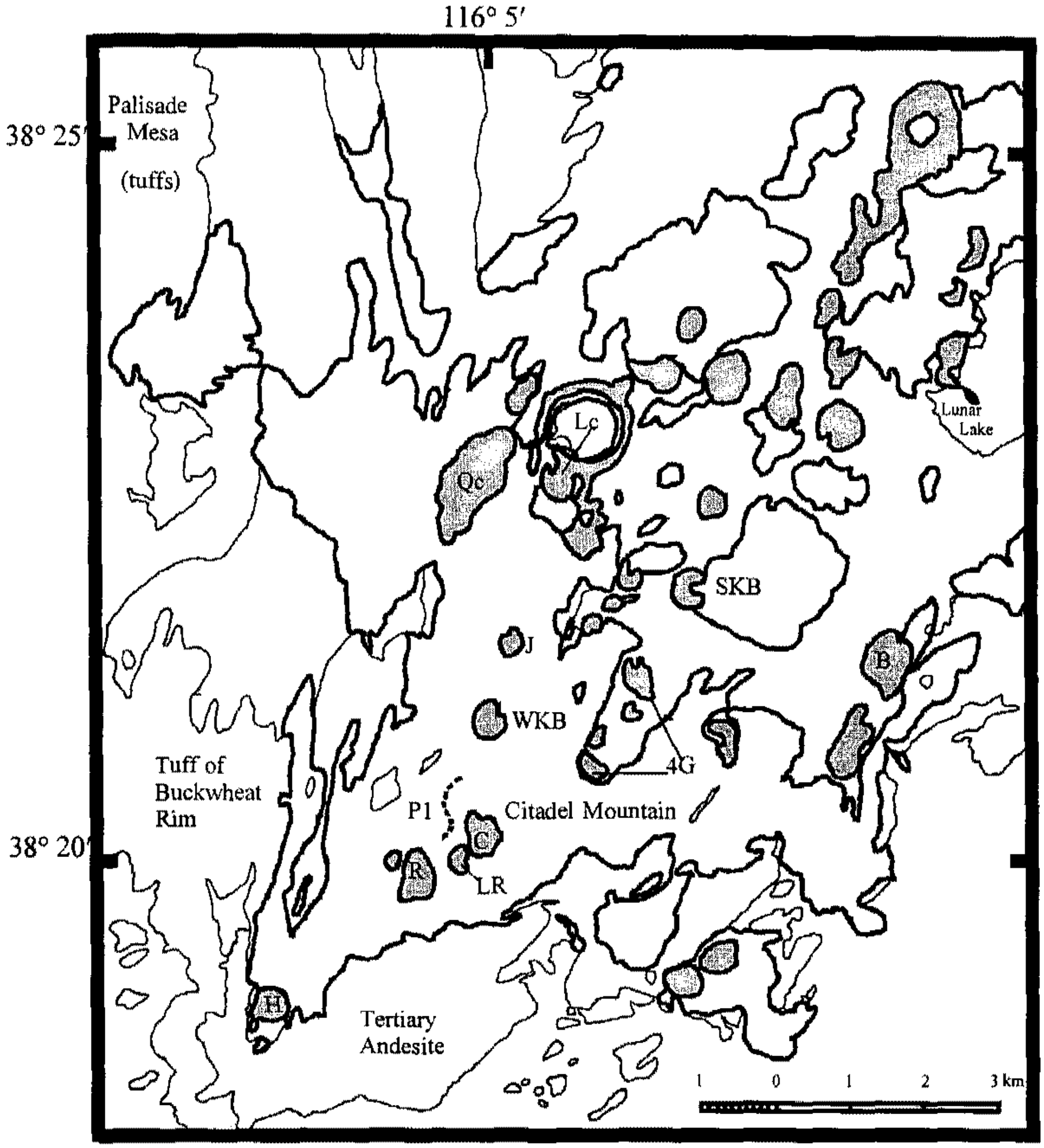

Figure 6. Index map shows letter or letter and number designations for cinder cones on and around Citadel Mountain. Cinder cones include Lc - Lunar Crater cone, Qc-cone, 4G-cones, J-cone, WKB - West Kidney Butte, SKB - South Kidney Butte, P1-cone, C-cone, LR-cone, R-cone, H-cone and B-cone. Cinder cones are shaded, basalt flows are outlined in thick black lines.

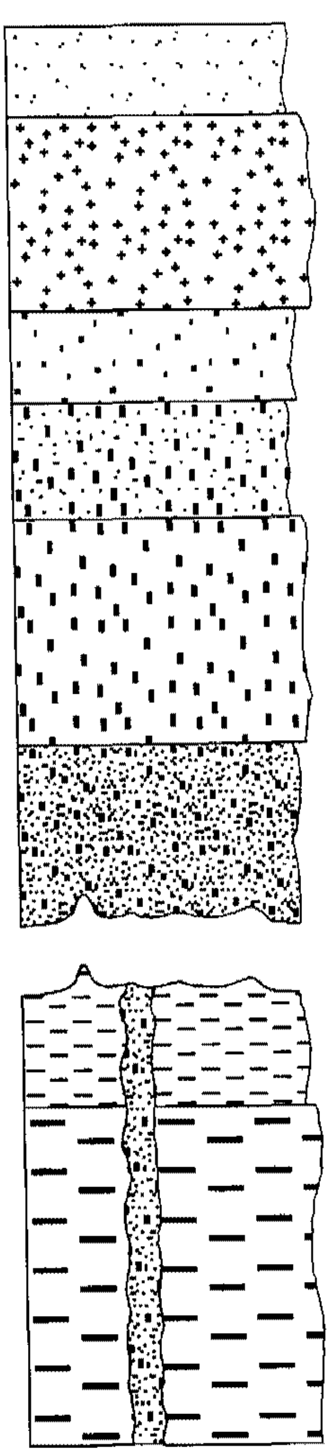

R-cone flow dated at 0.66 ± 0.34 Ma; 3.1 m thick. Unit is crystal-poor with few phenocrysts of plagioclase, fresh olivine and clinopyroxene.

C-cone flow dated at 1.15 ± 0.14 Ma; Kargel (1987); 6.6 m thick. Unit is highly vesicular and contains abundant fresh olivine and lesser amounts of plagioclase and clinopyroxene.

Qc-cone flow dated at 1.61± 0.14 Ma; Kargel (1987); 3 m thick. Unit contains abundant large fresh olivine, few but large plagioclase phenocrysts and clinopyroxene. Unit also contains xenocrysts of olivine, hornblende and mica.

Lunar Crater flow dated at 2.97 ± 0.06 Ma; 4 m thick. Unit contains abundant large altered olivine, few but large plagioclase megacrysts and small clinopyroxene. Clinopyroxene also occurs as aglomeroporphyritic inclusions with plagioclase.

H-cone flow dated at 3.82 ± 0.05 Ma; 7.6 m thick. Unit is similar to P1-cone basalt, but contains less olivine. Unit also contains large plagioclase phenocrysts and large, abundant clinopyroxene.

P1-cone flow dated at 3.82 ± 0.06 Ma; 6 m thick. Unit contains abundant large plagioclase phenocrysts and megacrysts, small altered olivine and small clinopyroxene with almost no vesicles.

Tuff of Buckwheat Rim dated at 24 Ma; Best et al. (1989); 152 m thick. Unit contains phenocrysts of quartz, alkali feldspar, plagioclase, biotite, hornblende, clinopyroxene and orthopyroxene.

Tertiary andesite lavas and flow breccias (age unknown); 366 m thick. Unit contains phenocrysts of plagioclase, clinopyroxene, hornblende, and biotite.

Figure 7. Stratigraphic column showing the relative thickness and stratigraphy of basaltic lava flows on Citadel Mountain.

Table 1: Geochronology

Sample	*Age*	
P1-cone Basalt	3.82 ± 0.06 Ma	$^{40}Ar/^{39}Ar$ date (this study, refer to Appendix C for details)
H-cone Basalt	3.82 ± 0.05 Ma	$^{40}Ar/^{39}Ar$ date (this study, refer to Appendix C for details)
Lunar Crater cone Basalt	2.97 ± 0.06 Ma	$^{40}Ar/^{39}Ar$ date (this study, refer to Appendix C for details)
Qc-cone Basalt	1.61 ± 0.14 Ma	K/Ar wholerock date; Kargel (1987).
C-cone Basalt	1.15 ± 0.14 Ma	K/Ar wholerock date; Kargel (1987).
R-cone Basalt	0.66 ± 0.34 Ma	$^{40}Ar/^{39}Ar$ date (this study, refer to Appendix C for details)

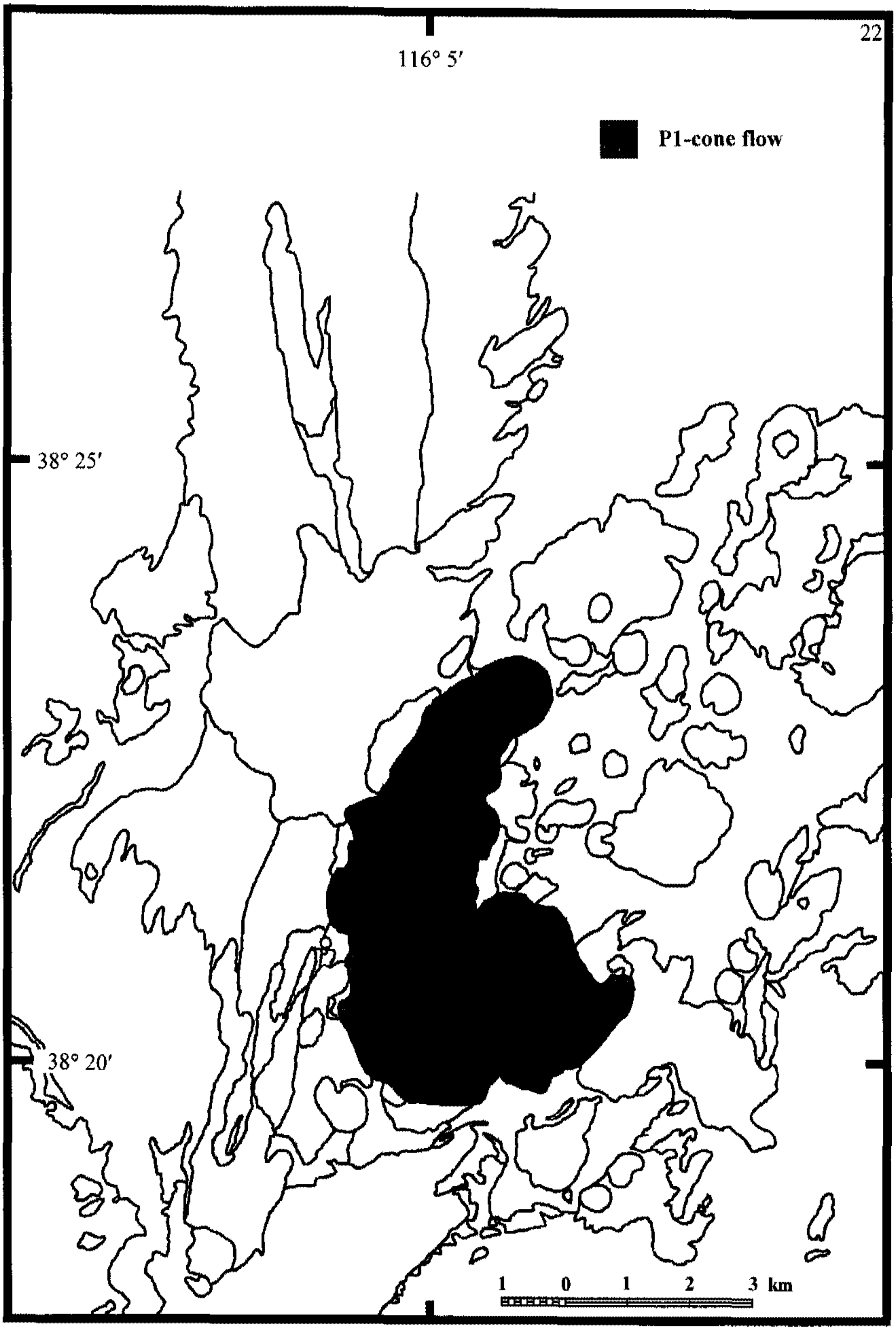

Figure 8. Distribution of P1-cone flows. P1-flows erupted from a scoria-dike complex at 3.82 Ma.

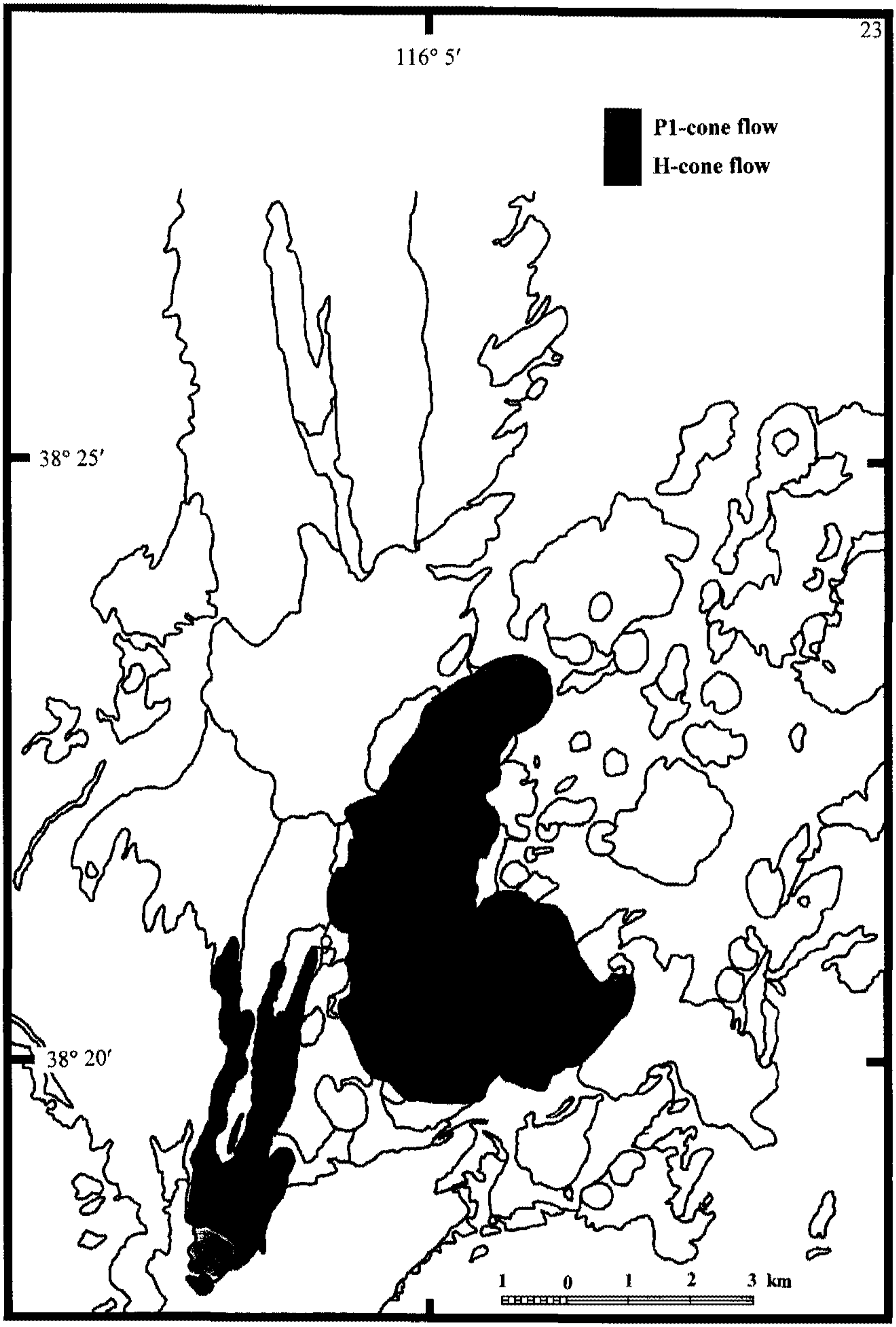

Figure 9. Distribution of H-cone flows. H-cone lavas erupted from a scoria cone (in red) at 3.82 Ma.

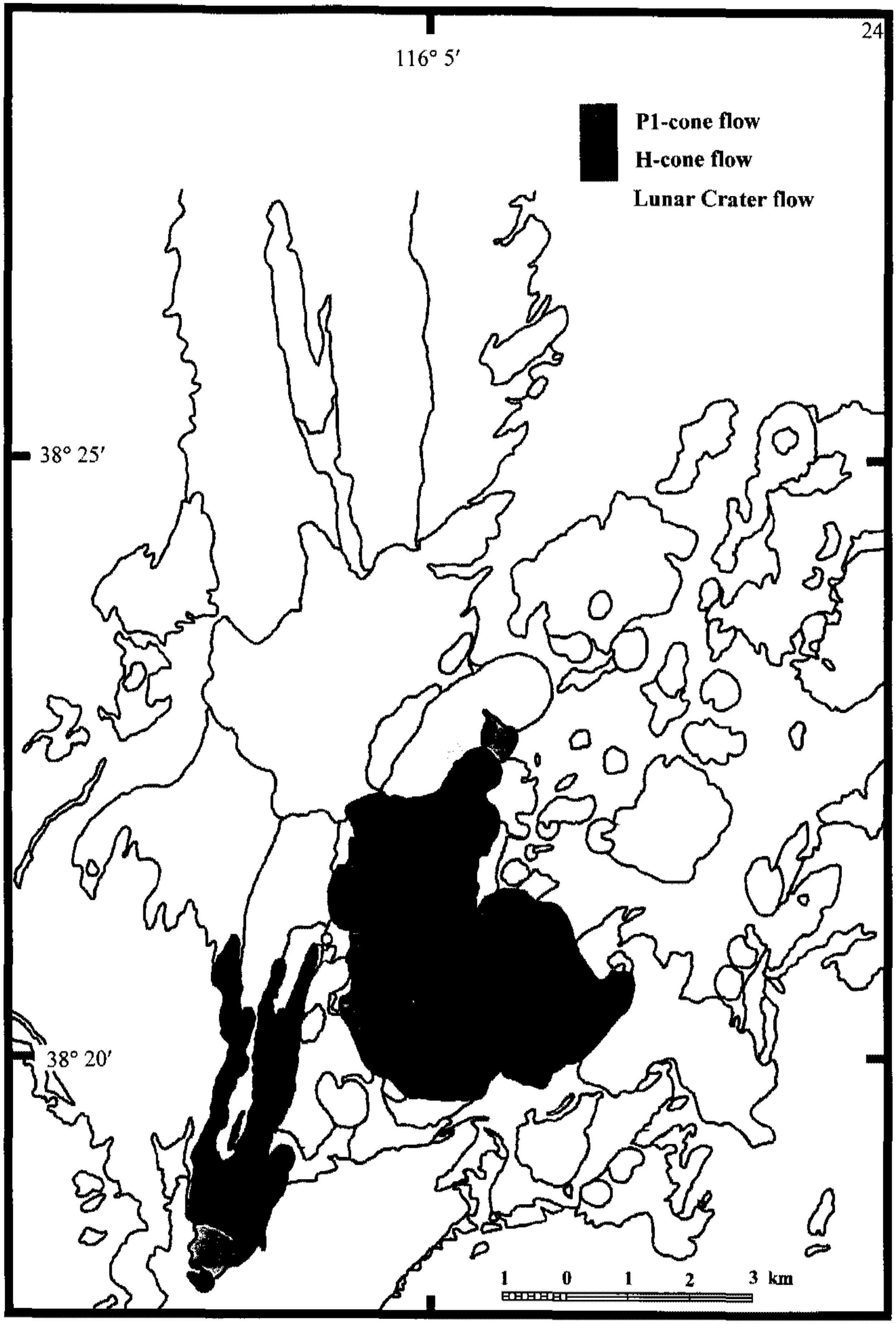

Figure 10. Distribution of Lunar Crater flows. Lunar Crater lavas erupted from a scoria cone (in red) at 2.97 Ma.

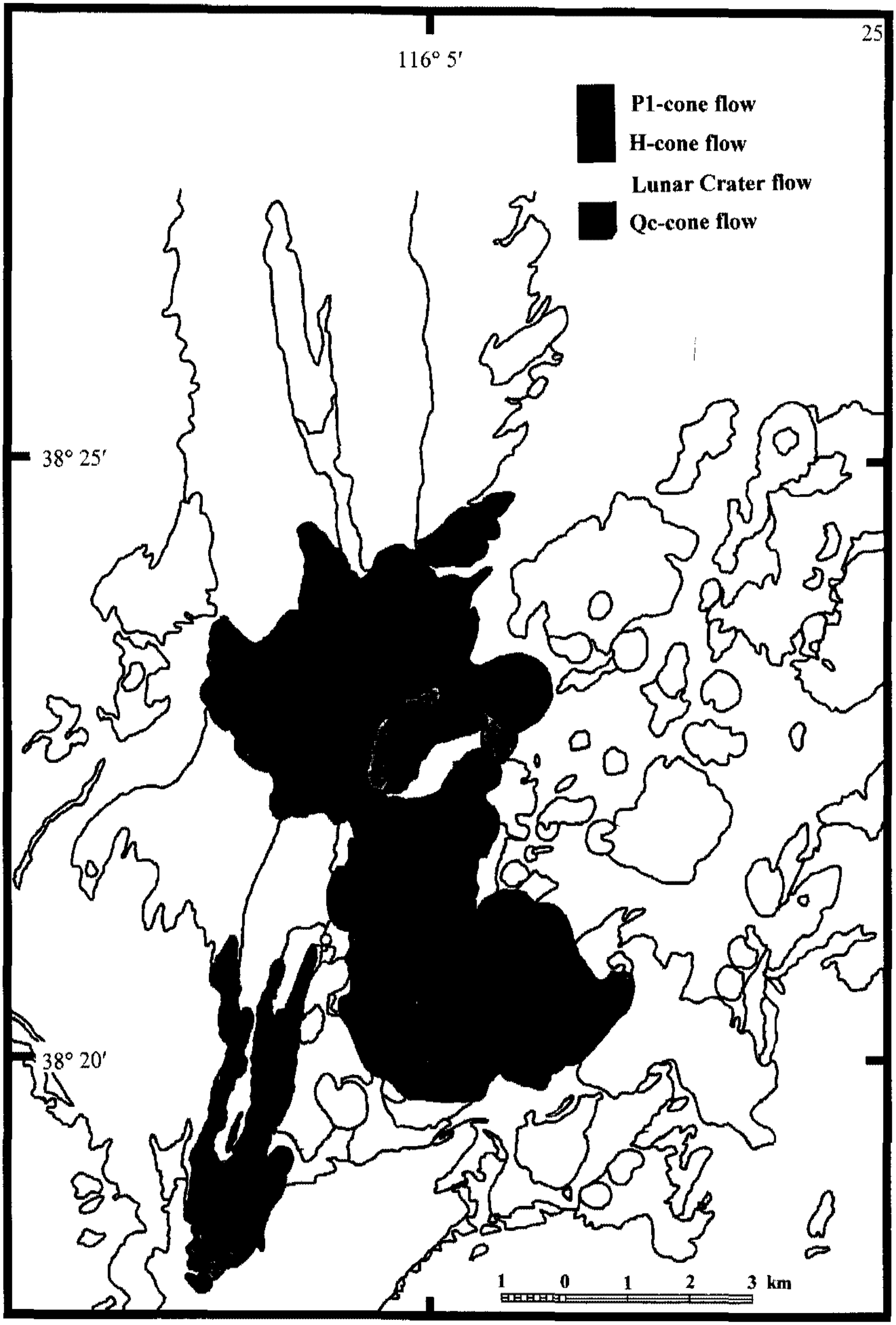

Figure 11. Distribution of Qc-cone flows. Qc-cone lavas erupted from a cluster of four scoria cones (in red) at 1.61 Ma.

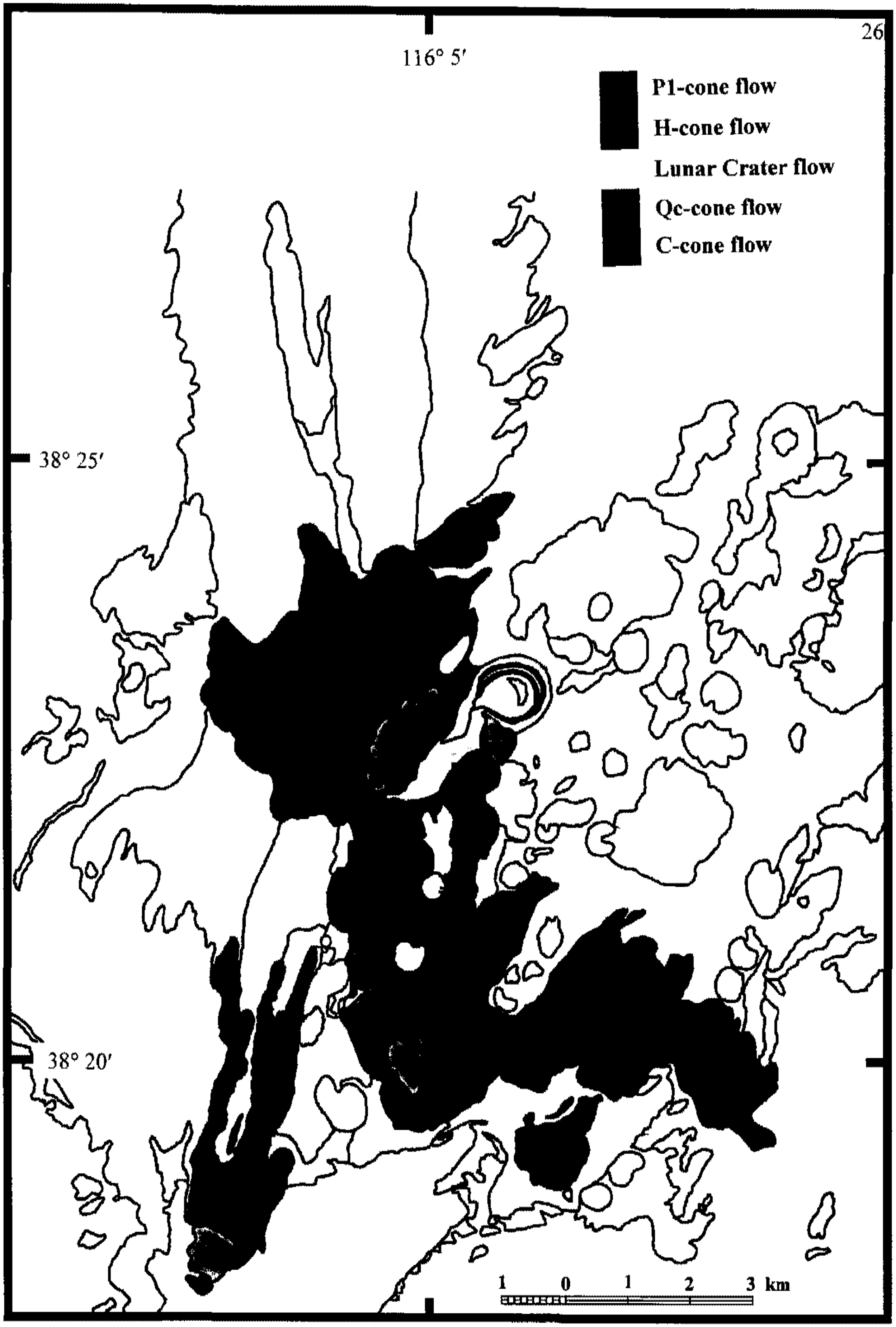

Figure 12. Distribution of C-cone flows. C-cone lavas erupted from a scoria cone (in red) at 1.15 Ma.

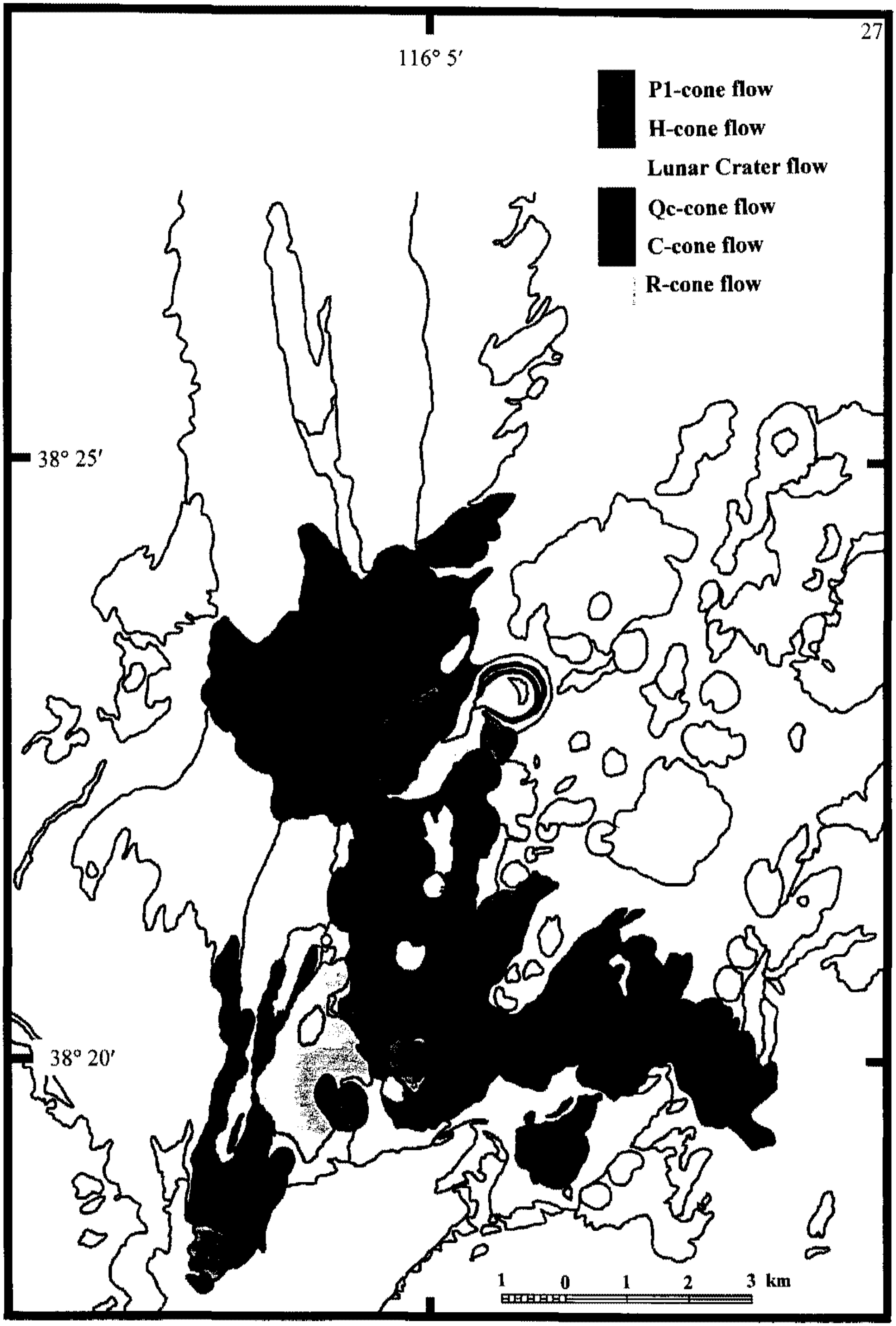

Figure 13. Distribution of R-cone flows. R-cone lavas erupted from a scoria cone (in red) at 0.66 Ma.

CHAPTER 3

PHYSICAL VOLCANOLOGY

Three major types of volcanic morphologies on and around Citadel Mountain are cinder cones and associated lava flows, spatter ramparts and maar craters. The three maar craters, Lunar Crater maar, Lunar Lake maar and Easy Chair Crater are described in the "Geologic Background" section in Chapter 1 and will not be considered further here. In general, cinder cones consist of block and lapilli-sized fragments of lava and welded scoria and often include thin dikes on the summits and flanks of the cones. Lava lake material occupies the summits of several cinder cones (e.g., H-cone and J-cone, Figures 14 and 15). Cinder cones have an average height of 70 meters but B-cone (Plate 1) exceeds 120 meters. The cones are moderately riled and commonly breached by lava flows. Lava flows are predominantly blocky a'a and range from 3 to 30 m thick (Foland and Bergman, 1992). With the exception of the P1 fissure flow, most lava flows erupted from small bocas at the base of the cones. Area and volumes of lava flows are variable (from 0.8 to 4.8 km^2 and 0.0025 to 0.027 km^3, respectively) and show no correlation of volume with location or age.

P1-cone is a scoria dike complex in the southern part of Citadel Mountain first discovered during field work for this thesis (Figure 16; Plate 1). It includes a sinuous dike 0.9 km in length surrounded by a low mound of red and black agglutinated scoria with individual scoria pieces up to 10 cm long with semi-elongated vesicles. Pieces of twisted scoria that were aerodynamically sculptured during flight occur on the flank of the cone and suggest that some fragments remained fluid during emplacement. The width of the P1-dike varies from more than 10 m to less than 1 m and has distinctive swell and pinch geometry. Though swells may be associated with locations of vents and pinches with connector dikes between vents, lava may have erupted from the entire length of the dike (i.e., it may be a fissure vent).

H-cone, the southernmost cone on Citadel Mountain, is 70 m high and was first discovered during field work for this thesis (Figures 14 and 17; Plate 1). H-cone is highly eroded and appears from a distance to have spines of lava projecting from its summit. The base of H-cone comprised predominately of red lapilli-sized scoria and small bombs also contains smaller amounts lapilli-sized fragments of black vesicular basalt and scoria. About half way up the flank of H-cone, scoria becomes predominantly red and the average size decreases to lapilli-size fragments, although bombs about 10 cm in length are still present. Toward the summit of H-cone the large "spines" of basalt contain few vesicles and may represent degassed fluid magma of a lava lake. Lava lake material is interbedded with agglutinated scoria and dips inward at 20° forming a saucer shaped structure. Interbedding of lava lake material with agglutinated scoria indicates alternating explosive Strombolian activity with calmer, gas poor, Hawaiian style lava lake activity.

C and R-cones (Figures 18 and 19, respectively; Plate 1), both approximately 70 m high, are rounded and symmetrical with steep slopes. C-cone comprised predominantly of red and black angular block-sized scoria with some lapilli also contains red sculptured scoria and small aerodynamically sculptured bombs. The flanks of R-cone comprised of bombs, blocks and lapilli (exceeding 7 cm) of red scoria is formed by material similar to that of C-cone but coarser material than that of H-cone. R-cone differs from C-cone by having agglutinated scoria near its top.

C-cone is associated with a nearby (0.1 km in distance) parasitic cone; the LR-cone (see Chapter 2; Figure 6). The LR-cone comprised of red agglutinated scoria is partially covered by black scoria from C-cone. The LR-cone forms an obstacle to lava flows from the R-cone (Plate 1). R-cone flows erupted from the north flank of R-cone but were turned to the south as they ran against the mound created by the P1 vent. Flows continued to the southeast toward the LR and C-cones but were diverted to the south when they reached the buttress created by the LR-cone. The contact between the R-flow and LR-cone is well exposed and preserves the only evidence for the relative age of R-cone and LR-cone. At the contact the R-flow contains large inclusions of agglutinated scoria from the LR-cone that were either incorporated by the R-flow as it moved over LR-cone debris or as LR-cone debris tumbled on top of R-flow (Figure 20).

J-cone is located in the northern half of Citadel Mountain (Figure 15; Plate 1). It is 40 m high and has remnants of a lava lake at its summit. Lava flows erupted at the base of J-cone and flowed to the north 0.8 km and abruptly terminates in exposures of blocky A'a lava.

The Lunar Crater cone is a steep, 60 m high cinder cone that sits on the southern rim of the Lunar Crater maar (Figure 21; Plate 1). Vertical dikes exposed on the northern and southern flanks of the cone extend from half-way up the cone to the summit. The cone is comprised of agglutinated scoria and 1-3 m long, welded blocks and bombs. The Lunar Crater cone pre-dates the maar eruption as indicated by large blocks (0.3 to 1 m long) of the Tuff of Buckwheat Rim ejected during the maar eruption on the summit and flanks of the cone. The explosive nature of a maar eruption is indicated by meter-sized blocks of tuff exposed on the south flank of the cone. These blocks were tossed over the 60 m high cone during the eruption.

Qc-cone, a cluster of four coalesced cinder cones 1.7 km in length, is aligned N30E and sits 1 km to the west of the Lunar Crater cone at the northern tip of Citadel Mountain (Figure 22; Plate 1). Flows from the cones spread radially to the north, east, and west. The largest of the cones, in the middle of the cluster, is breached on its west side.

The two spatter ramparts were discovered during field work for this thesis. The larger spatter rampart (50 m in diameter) erupted on a steep slope of the Tuff of Buckwheat Rim and is formed of red agglutinated scoria (Plate 1). It contains a 3 m thick inward dipping flow capped with red scoria. The smaller spatter rampart (30 m in diameter) comprised of a ring of red, welded, poorly vesicular scoria preserves remnants of a lava lake on its walls and floor (Figure 23; Plate 1). A thin (<1 m) lava flow breached the rim of the spatter rampart on the east side. Lava associated with the flow crops out on top of the breached rim and 20 m downslope to the east.

Compared to spatter ramparts formed during Hawaiian style eruptions, the example on Citadel Mountain is larger (about twice the diameter) and may be associated with more explosive Strombolian style eruptions. An excellent example of a spatter rampart occurs on the floor of Haleakal'a Crater at the summit of West Mau'i volcano, Hawai'i (Sinton et al., 1997) (Figure 24). The rampart approximately 15 m in diameter, is formed by 3 m high walls of welded spatter. Although, there are no detailed published studies of circular Hawaiian spatter ramparts, this feature appears to be typical in size and shape to other similar features produced by Hawaiian style eruptions (Sinton et al., 1997). The Citadel Mountain spatter rampart differs from the example in Haleakal'a Crater in that it is composed of welded vesicular scoria rather than fluid spatter. A possible explanation for this difference is the explosive Strombolian style of Citadel Mountain volcanism. Strombolian eruptions are cooler but more gas rich and explosive than Hawaiian eruptions; therefore the products are vesicular scoria rather than fluid, gas poor spatter. Because of the more explosive nature of Strombolian eruptions, ejecta travels farther from the vent; thus explaining the larger size of the Citadel Mountain example.

Figure 14. H-cone shows remnants of a lava lake at its summit. The lava lake deposits form a saucer shape but appear as spines from a distance.

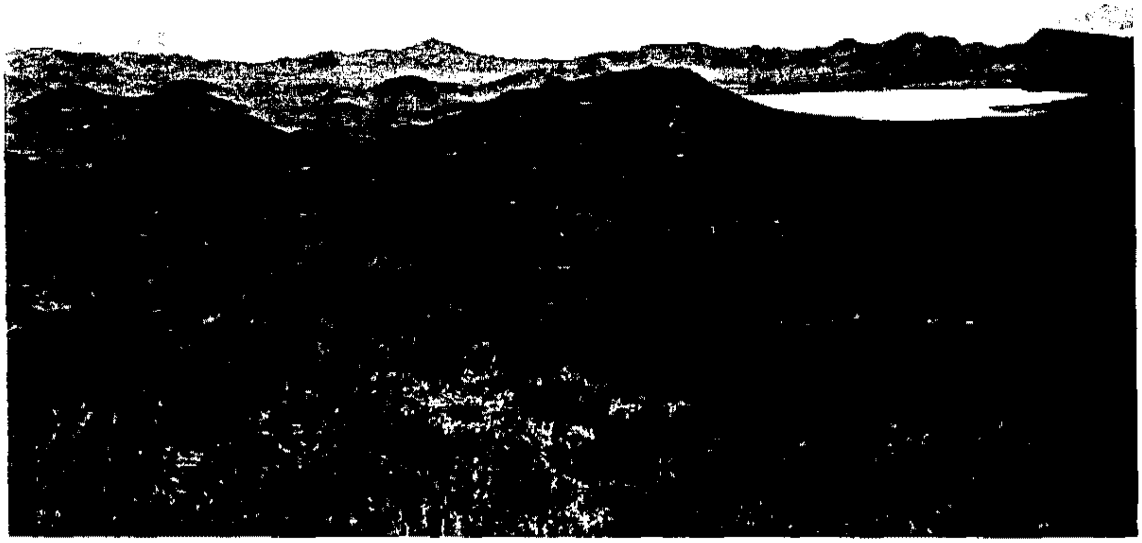

Figure 15. Photograph of J-cone viewed to the northeast toward the Lunar Lake playa. J-cone has inward dipping lava lake deposits at its summit.

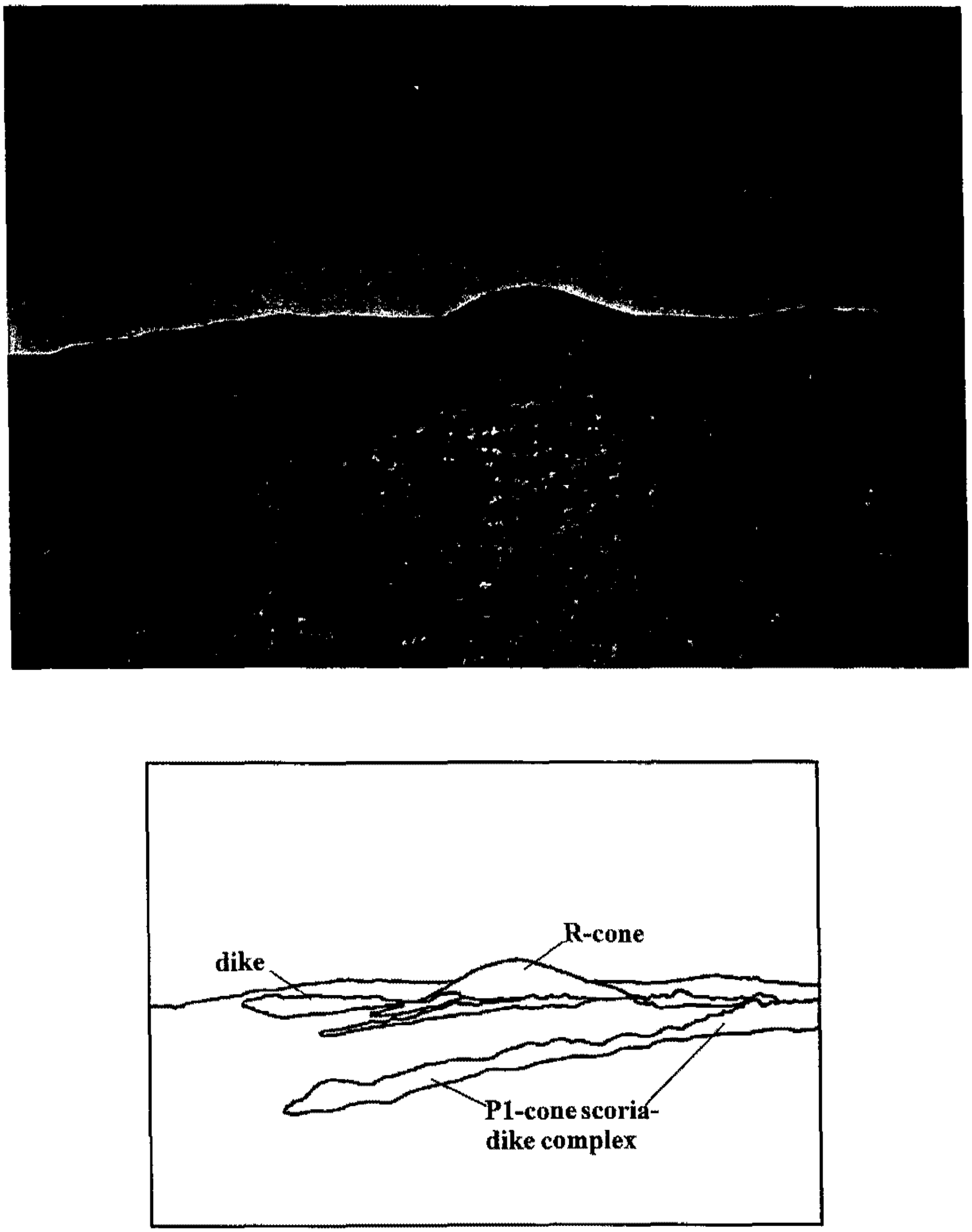

Figure 16. The P1-cone scoria-dike complex in the foreground shows the "S" curve of the dike. The dike crops out along the entire length of the P1-cone vent. The P1-cone itself is a low lying mound compared to the other cinder cones on Citadel Mountain and averages 24 meters high. R-cone appears in the background of this photograph.

Figure 17. Photograph of the H-cone flow cascading over an escarpment of the Tuff of Buckwheat Rim on the west side of Citadel Mountain. The vertical distance from the top of Citadel Mountain to the valley is approximately 300 meters.

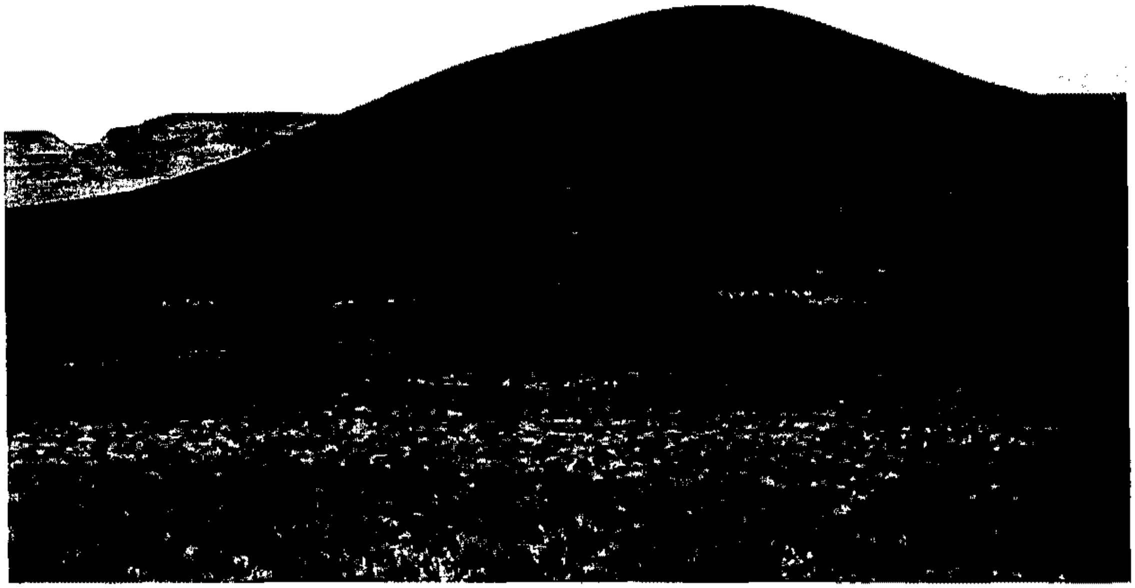

Figure 18. C-cone comprised of red and black scoria, lapilli and aerodynamically sculptured bombs is 70 meters high, rounded and symmetrical.

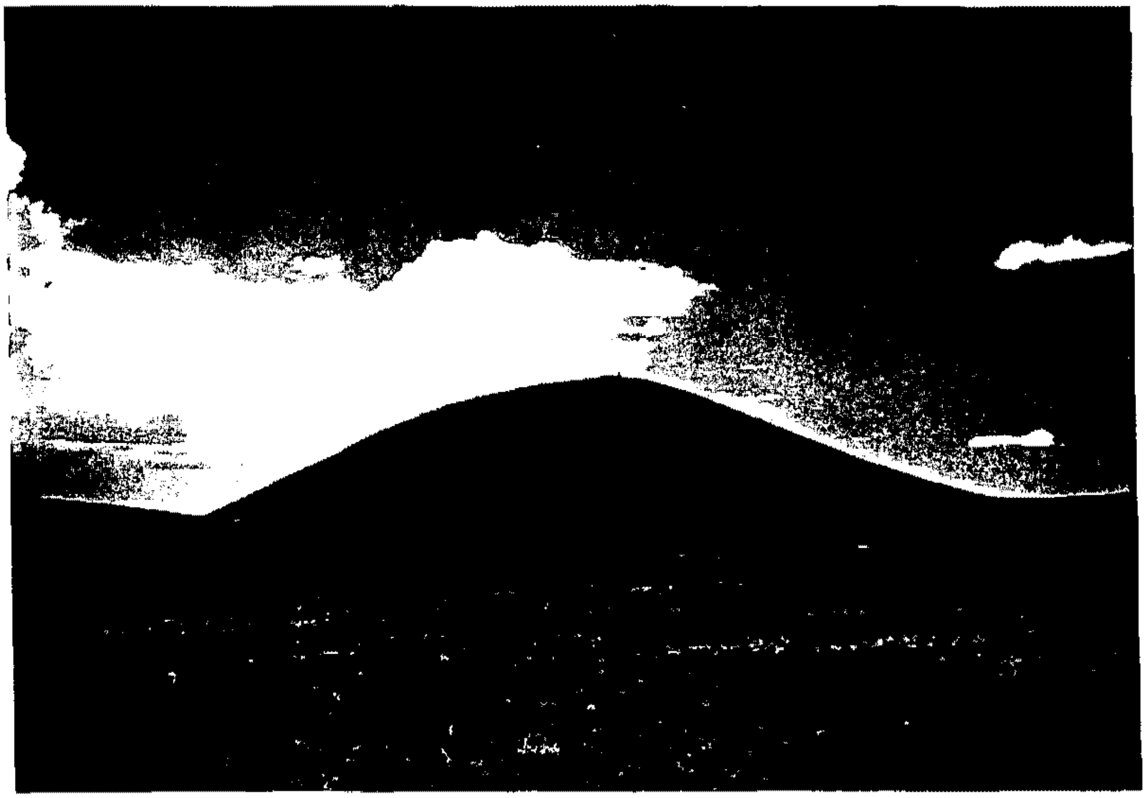

Figure 19. R-cone, comprised of red scoria, lapilli and bombs is 70 meters high, but differs from C-cone (see Figure 18) by having steeper slopes and agglutinated scoria near its top.

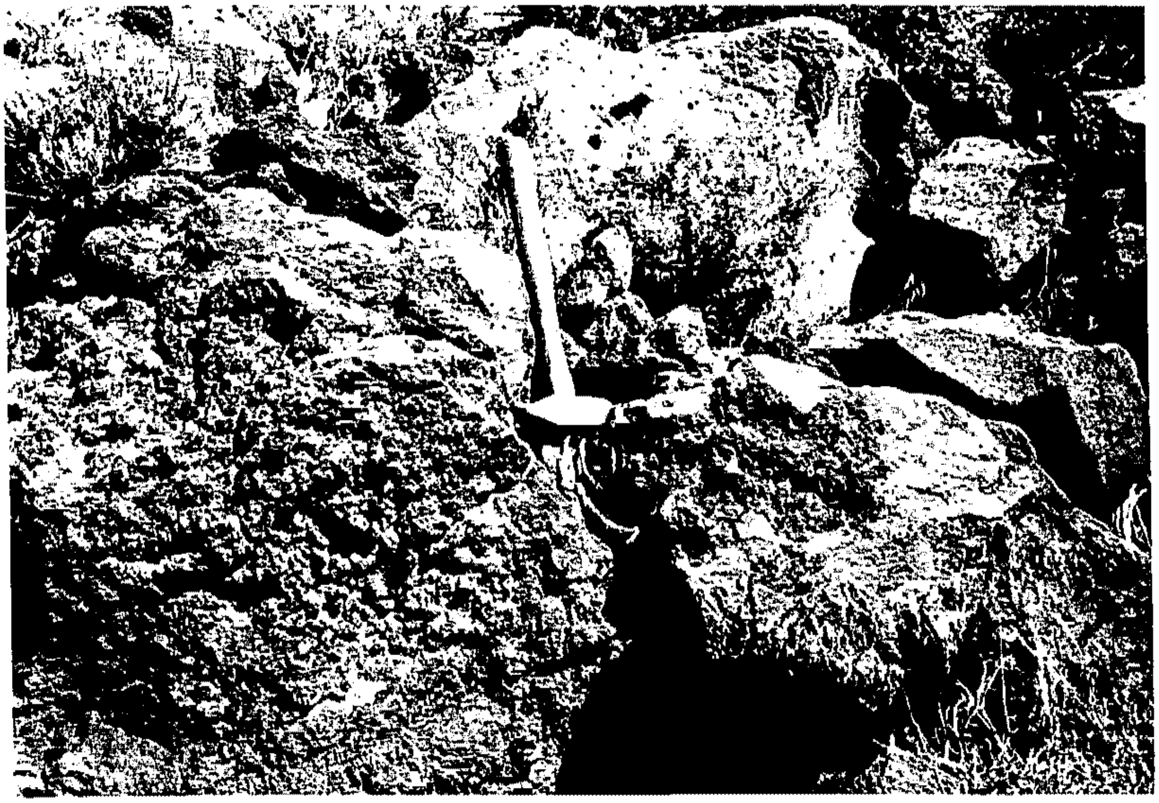

Figure 20. The contact zone between the R-cone flow and the LR-cone (near C-cone) shows large pieces of red agglutinated scoria from the LR-cone either fell into or were picked up by the R-cone flow as it passed by. The contact relationships indicate that the R-cone flow is younger than the LR-cone.

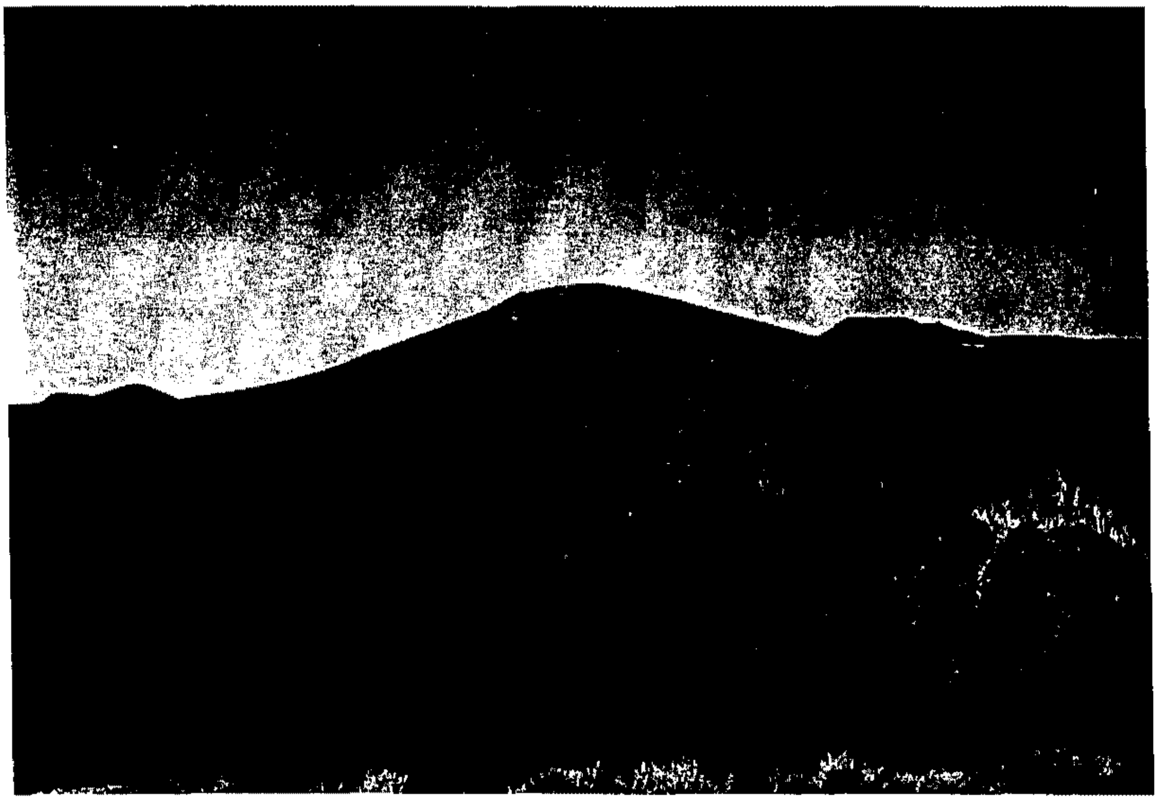

Figure 21. Lunar Crater cone sits on the southern rim of the Lunar Crater maar. The cone comprised of agglutinated scoria and welded blocks and bombs has three dikes exposed on its northern flank.

Figure 22. Qc-cone viewed to the west from Lunar Crater maar. The photograph shows the two northernmost cones of the Qc-cone cluster.

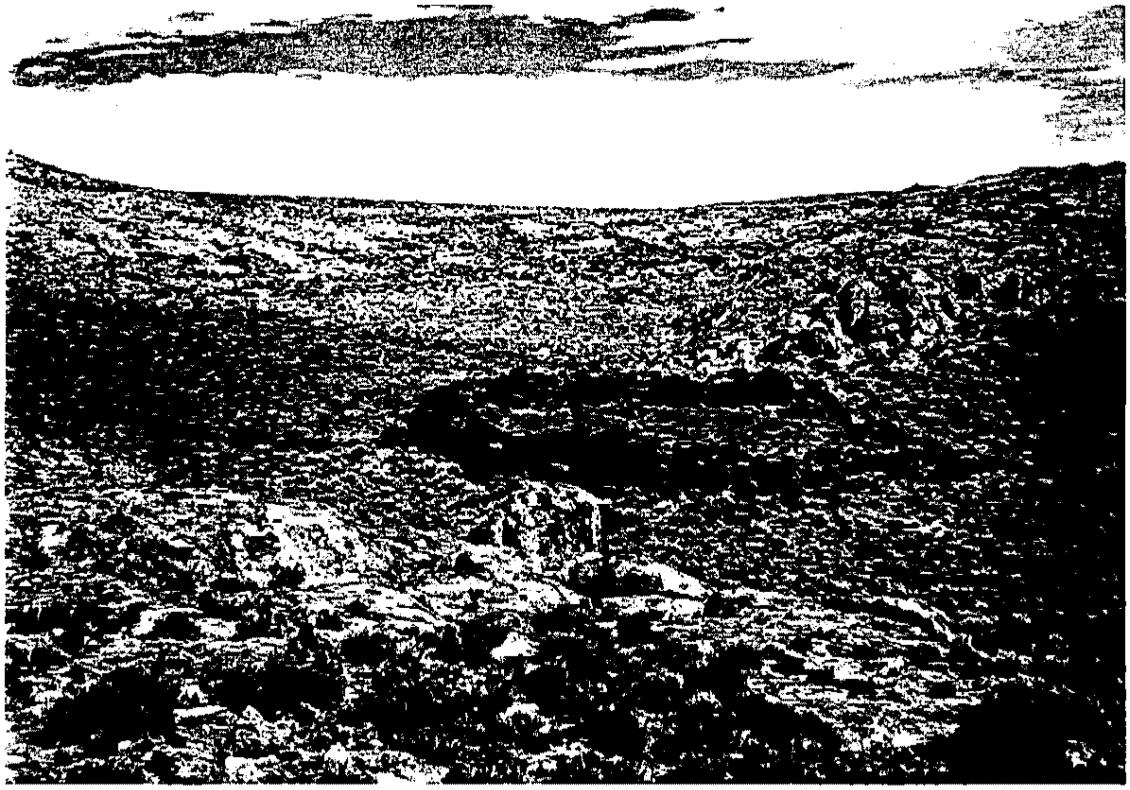

Figure 23. Small spatter rampart comprised of red, welded, poorly vesicular scoria is 30 meters in diameter with 1-2 meter high walls.

Figure 24. Spatter rampart located on the floor of Haleakal'a Crater at the summit of West Mau'i volcano, Hawai'i. The 15 m spatter rampart is an excellent example for comparison to spatter ramparts located on Citadel Mountain, Pancake Range, Nevada.

CHAPTER 4

PETROGRAPHY

Pliocene and Quaternary Basalts

Individual Pliocene and Quaternary basalt flows on Citadel Mountain range in total thickness from 3 to 61 meters. The basalts are vitric, aphanitic, porphyritic and range from dense to vesicular. The basalts are alkali olivine basalts containing phenocrysts of plagioclase, olivine, augite and hornblende. Some LCVF lavas and scoria in the northern Pancake Range contain peridotite, gabbro, anorthosite, amphibolite and syenite nodules (Kargel, 1987), however only one ultramafic nodule was discovered on Citadel Mountain in lavas from Qc-cone.

In this study, basalts from Citadel Mountain were closely examined in the field and divided into six groups. Each group has a characteristic mineralogy that was helpful in identifying flows in the field. Each group is associated with a specific cinder cone and flow.

<u>P1-cone Basalt:</u> P1-cone basalt is characterized by its abundance of plagioclase phenocrysts and megacrysts (12-21 mm). P1-cone porphyritic basalt contains 35% phenocrysts of plagioclase (67%), olivine (28%), clinopyroxene (3%) and iron oxide (2%). P1-cone basalt contains two types of plagioclase; the first is euhedral to

subhedral (5-8 mm) showing albite twinning. Some plagioclase crystals are zoned, fractured and locally filled with $CaCO_3$. The second type of plagioclase is rounded, anhedral and heavily pitted. Olivine is small (1-3 mm), subhedral to anhedral and is almost completely altered to iddingsite. Olivine is highly fractured and have somewhat corroded rims. Clinopyroxene is anhedral, light brown in color and highly fractured. Some clinopyroxene grains are twinned and size varies from <1 mm to 1.5 mm. The matrix of P1-cone basalt is composed of laths of plagioclase, subhedral olivine and small irregular grains of iron oxide. P1-cone basalt is medium gray in color and has almost no vesicles. P1-cone basalt forms the P1-dike and its surrounding scoria and the P1-cone flow.

H-cone Basalt: H-cone basalt is similar to P1-cone basalt except it contains less olivine and is more vesicular. H-cone porphyritic basalt contains 35% phenocrysts of plagioclase (69%), clinopyroxene (27%), olivine (2%) and iron oxide (2%). Plagioclase phenocrysts are euhedral to subhedral laths and blocky grains showing albite twinning. Some crystals are zoned, and intergrown clusters of plagioclase crystals occur. Size of plagioclase crystals grade from phenocrysts (7 mm) to matrix crystals. Clinopyroxene is abundant in the matrix, occurs in phenocryst phase (2-5 mm) and may have intergranular textures with plagioclase. Olivine occurs as large (2 mm), highly pitted grains with corroded margins and iron oxide occurs as small grains in the matrix. H-cone basalt also contains xenocrysts of rounded quartz. H-cone basalt is medium gray in color and erupted to form the H-cone and H-cone flow.

Lunar Crater cone Basalt: Lunar Crater cone basalt is characterized by its abundance of large altered olivine phenocrysts (1-4 mm) and few but large subhedral plagioclase megacrysts (12 mm). Lunar Crater porphyritic basalt contains 50% phenocrysts of olivine (60%), plagioclase (30%), clinopyroxene (8%) and iron oxide (2%). Olivine is subhedral, fractured and altered to iddingsite along fractures and margins of the grains. Plagioclase is subhedral and shows albite twinning. Two types of plagioclase are present; the first shows no evidence of corrosion and has sharp contacts with the matrix (1-2 mm). The second type of plagioclase is zoned and contains pits that are likely filled with glass. The glass-filled pits occur in the core of the crystal or as a distinct zone. Clinopyroxene is light brown in color and occurs as aglomeroporphyritic inclusions with plagioclase (1-4 cm) and also as isolated anhedral grains (1-3 mm). The matrix is composed of plagioclase laths, olivine altered to iddingsite and small iron oxide grains. There is no evidence for glass in the matrix. Lunar Crater cone basalt is medium dark gray in color and produced the Lunar Crater cone and Lunar Crater flow.

Qc-cone Basalt: Qc-cone basalt is characterized by large fresh olivine phenocrysts (3-10 mm) and few but large subhedral plagioclase phenocrysts (5 mm). Qc-cone porphyritic basalt contains 20% phenocrysts of olivine (75%), plagioclase (20%), clinopyroxene (2.5%) and iron oxide (2.5%). Olivine is fresh and occurs as subhedral, fractured grains; although, some are embayed and corroded. Qc-cone basalt shows strong alignment of plagioclase laths. Two types of plagioclase phenocrysts occur; the first are subhedral, rectangular grains showing albite twinning. The second type of plagioclase occur as rare anhedral, highly corroded grains up to 2 mm in size.

Clinopyroxene is anhedral and light brown in color. Several clinopyroxene grains contain numerous wormlike inclusions of iron oxide. The matrix contains aligned plagioclase laths, euhedral olivine and iron oxide. There is no evidence for glass in the matrix. Also present are large xenocrysts (15 mm) of olivine, hornblende and mica (phlogopite?). Qc-cone basalt is dark gray in color and makes up the four coalesced Qc-cones and the Qc-cone flows.

C-cone Basalt: C-cone basalt is highly vesicular and is characterized by its abundance of fresh olivine (although not as abundant as Qc-cone basalt). C-cone porphyritic basalt contains 40% phenocrysts of olivine (50%), plagioclase (37.5%), clinopyroxene (7.5%) and iron oxide (5%). C-cone basalt contains two types of plagioclase; the first is lath shaped, euhedral to subhedral and shows albite twinning (< 1 mm). The second type of plagioclase is large (3-7 mm) anhedral, highly corroded with embayed margins. Some crystals show extensive pitting along the margins. Olivine is fresh and subhedral (1-3 mm); some grains are embayed. Clinopyroxene is anhedral and contains wormlike inclusions of iron oxide (3-4 mm). Also present are xenoliths of olivine-plagioclase bearing basalt. C-cone basalt is dark gray in color and formed the C-cone and C-cone flow.

R-cone Basalt: R-cone basalt is characterized by being crystal-poor with small fresh olivine and a few phenocrysts of plagioclase (4-5 mm). R-cone porphyritic basalt contains 30% phenocrysts of plagioclase (50%), olivine (33%), clinopyroxene (10%) and iron oxide (7%). R-cone basalt shows alignment of plagioclase laths in the matrix. Two types of plagioclase are present; the first are small (<1 mm) euhedral to subhedral laths showing albite twinning. The second type of plagioclase are blocky anhedral grains 0.5 mm in size. One plagioclase grain (1 mm) is highly altered and clouded with iron oxide, yet the crystal still shows faint albite twinning. Olivine is small (1 mm) and euhedral to subhedral; few grains have moderate to strong alteration to iddingsite, although, most olivine grains are fresh. Clinopyroxene is subhedral, light brown in color and show alteration to iron oxide. The matrix is composed of plagioclase laths, olivine and small iron oxide grains. R-cone basalt is medium dark gray in color and formed the R-cone and R-cone flow.

Tertiary Intermediate and Felsic Rocks

Andesite lavas and flow breccias and the Tuff of Buckwheat Rim (Ekren et al., 1972) form Citadel Mountain. Monotony tuff, Shingle Pass Tuff and Tuff of Lunar Cuesta are inferred basement rocks (Ekren et al., 1972), but are not exposed on Citadel Mountain. The andesites may have erupted from the southwest extension of the same northeast trending faults used as conduits by the Pliocene to Recent alkali basalts (Ekren et al., 1974).

<u>Monotony Tuff:</u> The Monotony Tuff (27.3 ± 0.03 Ma; Best et al., 1989; 27.6 Ma, Rash, 1995) is a simple cooling unit of dacite ash-flow tuff approximately 305 m thick. The unit contains quartz (10-32%), alkali feldspar (5-12%), plagioclase (46-63%), biotite (10-20%) and trace amounts of clinopyroxene and hornblende (Ekren et al., 1972). The Monotony Tuff is the stratigraphically lowest unit in the Pancake Range and erupted from the Pancake Range caldera (Ekren et al., 1974).

Shingle Pass Tuff: The Shingle Pass Tuff is two cooling units of rhyolite ash-flow tuff approximately 61 m thick that contains quartz (0-15%), alkali feldspar (25-47%), plagioclase (30-65%), biotite (4-8%), hornblende (1-2%) and trace amounts of clinopyroxene (Ekren et al., 1972). The upper cooling unit is 25.35 ± 0.66 Ma (Rash, 1995). The Shingle Pass Tuff erupted from the Quinn Canyon Range caldera (Best et al., 1989).

Tuff of Lunar Cuesta: The Tuff of Lunar Cuesta is a 122 m thick, densely welded dacite to rhyolite cooling unit that contains quarts (12-20%), alkali feldspar (7-15%), plagioclase (45-75%), biotite (10-15%) and hornblende (3%) (Ekren et al., 1972). The Tuff of Lunar Cuesta is 22.5 ± 0.7 Ma (K/Ar date on sanidine) and is suggested to have erupted from the Lunar Lake caldera (Ekren et al., 1974).

Tertiary Basaltic Andesites: Basaltic andesites (Miocene) located 11 km to the east of Citadel Mountain are fine grained, medium dark gray in color, aphyric and contain 2% plagioclase phenocrysts (1-2 mm). The matrix is composed of aligned plagioclase laths (<0.5 mm) with intergranular clinopyroxene and iron oxide.

Tertiary Andesite Lavas and Flow Breccias: Andesite lavas and flow breccias are dark gray to black and porphyritic with 40% phenocrysts of plagioclase (50%), clinopyroxene (37.5%), hornblende (5%), biotite (5%) and iron oxide (2.5%). Plagioclase is either blocky or lath shaped and euhedral to subhedral. Some plagioclase grains are anhedral, highly fractured and altered to calcite. Clinopyroxene is subhedral and brown or light green in color. Clinopyroxene also occurs as aglomeroporphyritic inclusions with plagioclase. Aglomeroporphyritic inclusions of hornblende, biotite and plagioclase are also present. Hornblende is most likely oxyhornblende; it is pleochroic, light to dark brown and subhedral. Some hornblende crystals have corroded rims, but most are fresh. Biotite is pleochroic and light to dark brown. Biotite is euhedral to subhedral, forms small grains in the matrix and also occurs in inclusions. Iron oxide occurs as subhedral, blocky grains black in color. Some of the biotite and hornblende crystals are likely disaggregated crystals that have mechanically broken away from the aglomeroporphyritic inclusions. The matrix is glassy showing flow banding and flow alignment of iron oxide grains. The matrix varies in color from dark red brown to light red brown. The andesite lavas and flow breccias range in thickness from 0 to >366 meters. Tertiary andesite lava forms the entire 366 m high southern slope of Citadel Mountain.

<u>Tuff of Buckwheat Rim:</u> The Tuff of Buckwheat Rim is formed by two moderately welded cooling units of rhyolite ash-flow tuff approximately 152 m thick (Ekren et al, 1974). The lower rhyolite unit contains phenocrysts of quartz (13%), alkali feldspar (30-43%), plagioclase (35-47%), biotite (2.5%), hornblende (3.5%), clinopyroxene (1.5%) and trace amounts of orthopyroxene. The upper cooling unit is rich in lithic fragments and contains phenocrysts of quartz (10-19%), alkali feldspar (0-1%), plagioclase (50-60%), biotite (11-16%), hornblende (9-17%) and trace amounts of clinopyroxene (Ekren et al., 1972). The upper Tuff of Buckwheat Rim is dated at 24 Ma (K/Ar date; Best et al., 1989).

CHAPTER 5

GEOCHEMISTRY

Analytical Techniques

Fifty-eight samples were collected for geochemical analyses. Most samples were collected on Citadel Mountain located in the southern part of the Pancake Range in the northern LCVF. Samples were also collected from flows associated with cinder cones surrounding Citadel Mountain in the central and northern Pancake Range. Geochemistry of samples collected in the Reveille Range in the southern half of the LCVF is from Yogodzinski et al. (1996). Each sample comprised of fresh rock chips was bagged and labeled. Samples were crushed to pea size in a Bico chipmunk crusher and then powdered in a Bico shatterbox to about 200 mesh. The chipmunk crusher is equipped with tungsten-carbide jaws and the shatterbox uses a tungsten-carbide ring inside a tungsten-carbide lined stainless steel bowl. Fused glass disks were prepared at a flux/sample ratio of 5:1 using 8.50 g lithium tetraborate ($Li_2B_4O_7$), 0.2740 g ammonium nitrate (NH_4NO_3) and 1.70 g powdered rock sample. All chemicals and powdered rock samples were measured to ± 0.0002 g. The mixture was melted at 1100°C for 30 minutes in Au-Pt crucibles and quenched in Au-Pt molds. Fused disks prepared with the 5:1 ratio provide high enough concentrations of sample so that both major and trace element analyses are possible on a single disk. Fused glass disks were stored in paper envelopes in a dessicator preceding analysis.

Major and trace element (Zr, Ba, Nb, Y, Rb, Sr, Cr and Ni) analyses were done using a Rigaku 3030 XRF spectrometer at the University of Nevada, Las Vegas. Additional trace and rare-earth element (REE) analyses (La, Ce, Pr, Nd, Sm, Eu, Gd, Tb, Dy, Ho, Er, Tm, Yb, Lu, Th, Hf, Ta, U, Pb, Cs, and Sc) were done by Inductively Coupled Plasma - Mass Spectrometer (ICP-MS) at the Geoanalytical Laboratory at Washington State University. Precision and accuracy for XRF and ICP-MS analyses are reported in Appendix A.

Sr, Nd and Pb isotopes were analyzed at the Isotope Geochemistry Laboratory, University of Kansas. Feuerbach et al. (1993) provided a detailed description of methods of isotope analysis. Precision and accuracy are reported in Appendix B.

Geochemistry of Mafic Rocks

Major Elements

Mafic rocks on and around Citadel Mountain are alkali basalts, tephrite basanites and trachy-basalts with SiO_2 ranging from 43.0 to 51.5 wt.% (Figures 25a and 25b). In general, basanites have higher CaO and TiO_2 and lower Al_2O_3 than alkali basalts (Figure 26). Magnesium numbers (Mg#) vary from 44.8 to 60.6 showing they are somewhat evolved compared to the range of values of 68-75 for basalts in equilibrium with mantle olivine compositions (Wilson, 1989; p. 22). K_2O and MnO values do not vary significantly and P_2O_5 changes from 0.39 to 0.85 wt.% as SiO_2 increases (Figure

26). Na_2O and Al_2O_3 also increase but Fe_2O_3, MgO, CaO, and TiO_2 decrease with increasing SiO_2 (Figure 26). Alkali basalts on and around Citadel Mountain are chemically similar to basalts in the Reveille Range in the southern part of the LCVF (Yogodzinski et al., 1996). SiO_2, Fe_2O_3, K_2O and MnO overlap, but Al_2O_3, TiO_2, and Na_2O are slightly higher and CaO and MgO are lower for many samples (Figure 27).

Trace Elements and Isotopes

A plot of Sr vs. Cr defines three magma groups that correspond to lava flows from individual cinder cones or closely spaced cinder cones (P1 and H-cone, C and R-cone and Qc and Lunar Crater cone (Figure 28). The first group of data corresponding to the P1 and H-cone flows has low Cr (92 to 154 ppm) and low Sr (430 to 505 ppm). The second group corresponding to the C and R-cone flows has intermediate Cr (116 to 182 ppm) and high Sr (577 to 738 ppm). The third group corresponding to the Qc and Lunar Crater flows has high Cr (185 to 244 ppm) and intermediate Sr (380 to 669 ppm). The third group appears to be continuous with the second group on Sr vs. Cr plots but is considered as a separate group because of differences in Zr, Y and Ni (see below; Figure 29).

The P1 and H-cone flows of the first group are easily identified by higher silica (up to 49.2 and 51.5 wt. % SiO_2, respectively) and higher Y (49 ppm) and lower Ni (69 ppm) compared to other groups (Figure 29). The P1-cone flow has ε_{Nd} values that vary between +3.88 to +4.55 and $^{87}Sr/^{86}Sr$ between 0.7036 and 0.7039; $^{207}Pb/^{204}Pb$ varies between 15.663 and 15.668 (Figures 30 and 31). H-cone flow has ε_{Nd} of +2.49, $^{87}Sr/^{86}Sr$ of 0.7048 and $^{207}Pb/^{204}Pb$ of 15.664 (Figures 30 and 31).

The C and R-cone flows of the second group are identified by having the highest Sr (738 ppm) and Nb (66 ppm) (Figure 29). The C-cone flow group has ε_{Nd} values that range from +5.55 to +5.76 and $^{87}Sr/^{86}Sr$ between 0.7033 and 0.7034; $^{207}Pb/^{204}Pb$ (15.599 and 15.609) lies on the Northern Hemisphere Reference Line (NHRL) and is the lowest ratio compared to the other groups (Figures 30 and 31). The R-cone flow has an ε_{Nd} of +5.3, $^{87}Sr/^{86}Sr$ of 0.7034 and $^{207}Pb/^{204}Pb$ of 15.633 (Figures 30 and 31). C and R-cone lavas plot in the field of Basin and Range OIB basalts interpreted as partial melts of the asthenospheric mantle (Fitton et al., 1991). Cr and Ni decrease with increasing SiO_2 for both C and R-cone lavas (Figure 29).

The Qc-cone and Lunar Crater flows of the third group contain the lowest Zr (136 ppm), the lowest Y (27 ppm) and the highest Ni (212 ppm) (Figure 29). Qc-cone lavas also plot in the field of Basin and Range OIB basalts. Qc-cone flow has an ε_{Nd} of +5.49, $^{87}Sr/^{86}Sr$ of 0.7033 and $^{207}Pb/^{204}Pb$ of 15.621 and lies close to the NHRL (Figures 30 and 31). The Lunar Crater flow is distinguished from the other third group basalts by lower ε_{Nd} (+3.35) and higher $^{87}Sr/^{86}Sr$ (0.7047) and $^{207}Pb/^{204}Pb$ (15.653) (Figures 30 and 31).

The three groups show slight depletion in large ion lithophile elements (LIL), especially Cs, Rb and Pb, slight depletion in light rare earth elements (LREE) and slight heavy rare earth elements (HREE) enrichment compared to OIB (Figure 32). None of the groups show high field strength element (HFSE) anomalies. Alkali basalts are similar to OIB except for one sample (LC11-96) from the B-cone flow located to the east of Citadel Mountain which is depleted in LIL and LREE and is slightly depleted in HREE.

Alkali basalts on Citadel Mountain are for the most part lower in Sr and Zr when compared to other alkali basalt fields (Reveille Range and Crater Flat) in the central Great Basin (Figure 33). Citadel Mountain alkali basalts have 380 to 738 ppm Sr and 136 to 229 ppm Zr. Episode 1 basalts in the Reveille Range contain 527 to 1098 ppm Sr and 298 to 505 ppm Zr. Episode 2 basalts have comparable Sr and Zr contents to Citadel Mountain lavas (584 to 724 ppm Sr and 186 to 366 ppm Zr). Crater Flat alkali basalts have the highest Sr (1204 to 1990 ppm) and Zr (363 to 435 ppm) (Bradshaw et al., 1994) of the three fields.

Geochemistry of Miocene Intermediate and Felsic Rocks

Major Elements

Miocene basaltic andesites located 11 km to the east of Citadel Mountain range from 54.4 to 54.9 wt. % SiO_2. Tertiary andesites (dacites*) that comprise Citadel Mountain range from 64.3 to 65.5 wt.% SiO_2 (Figures 34a and 34b). Both basaltic andesites and andesites are subalkaline and have lower Fe_2O_3, TiO_2, CaO, MnO, P_2O_5, and MgO and have higher Al_2O_3 and K_2O than the Pliocene alkali basalts. The basaltic andesites located to the east of Citadel Mountain differ from those in the Reveille Range (Rash,

---

* The dacitic rocks were originally mapped and classified as Tertiary andesites (Ekren et al., 1972) but are chemically dacites. To prevent confusion they will be referred to as the Tertiary andesites for the remainder of this thesis.

1995) by having slightly higher Fe_2O_3, Al_2O_3, TiO_2, Na_2O, P_2O_5, and slightly lower MgO, MnO, CaO and K_2O.

Trace Elements

Miocene basaltic andesites and andesites (Tertiary andesites) show LIL enrichment (1 to 8 x OIB), higher LREE, higher HREE and lower Ta, Sc, Cr, Ni, and Nb compared to Pliocene alkali basalts in the LCVF. Basaltic andesites and andesites (Tertiary andesites) have strong negative Nb and Ti anomalies and positive Pb anomalies compared to OIB (Figure 35). Basaltic andesites to the east of Citadel Mountain have similar trace element abundances to those in the Reveille Range. The only major difference between basaltic andesites east of Citadel Mountain and Reveille Range basaltic andesites is higher Sr (250 ppm higher) in Reveille Range basaltic andesites.

Isotopes

Basaltic andesites have ε_{Nd} -7.27 to -7.63 and $^{87}Sr/^{86}Sr$ between 0.7076 and 0.7077; $^{207}Pb/^{204}Pb$ varies slightly from 15.626 to 15.645 and $^{206}Pb/^{204}Pb$ (18.75) is the lowest measured in the Pancake or Reveille Range. Tertiary andesites have a ε_{Nd} value of -7.03 and $^{87}Sr/^{86}Sr$ of 0.7084; $^{207}Pb/^{204}Pb$ is 15.69, the highest value of all samples collected in this study.

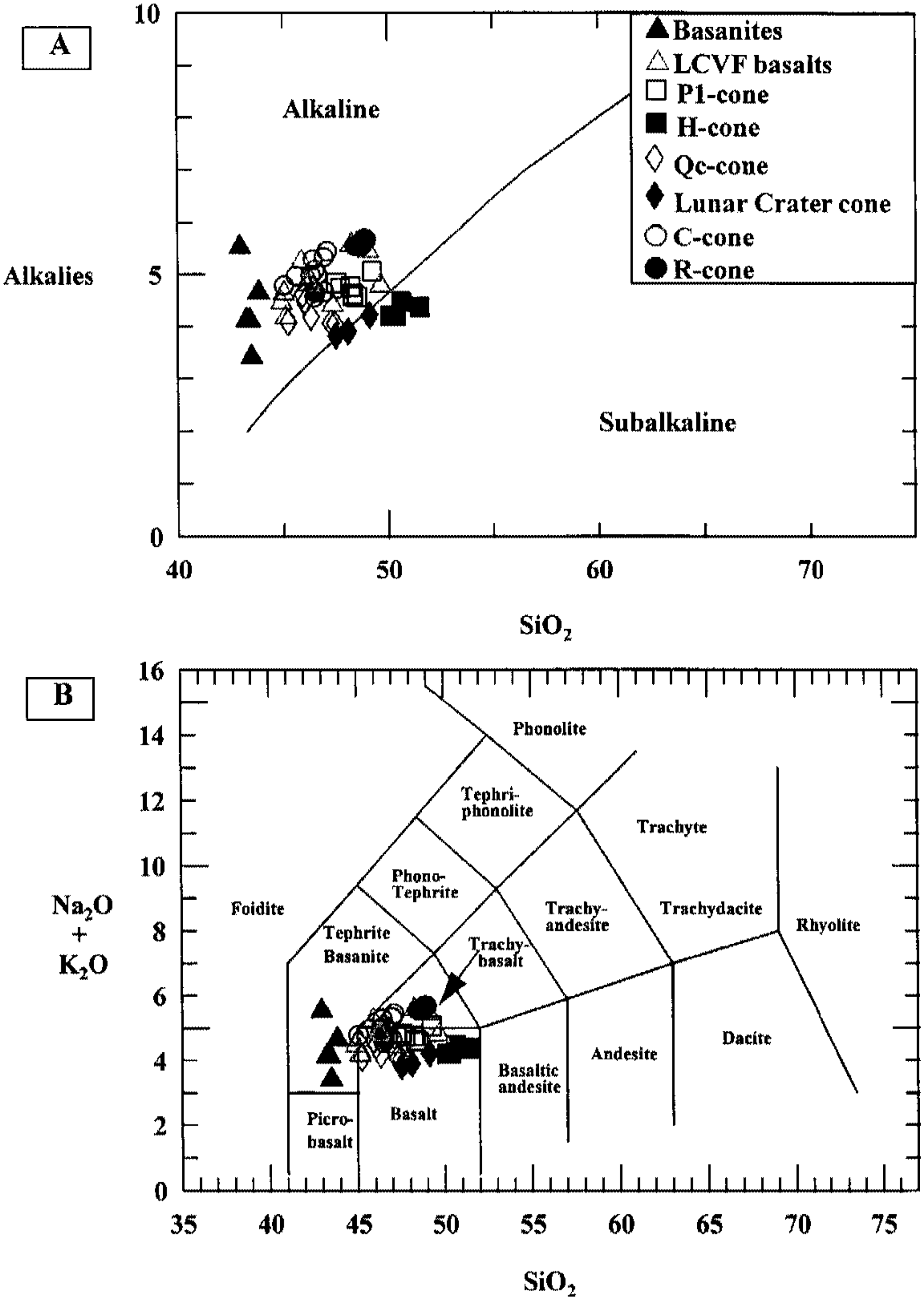

Figure 24a. LCVF basalts are predominantly alkali basalts on the alkalies vs. SiO$_2$ plot. **Figure 24b.** The alkali basalts in the LCVF are tephrite basanites, trachy-basalts and basalts using the classification of Lebas et al. (1986). Samples collected around Citadel Mountain and analyzed as part of this study are included for comparison. Sample locations are shown on Figures D1 and D2.

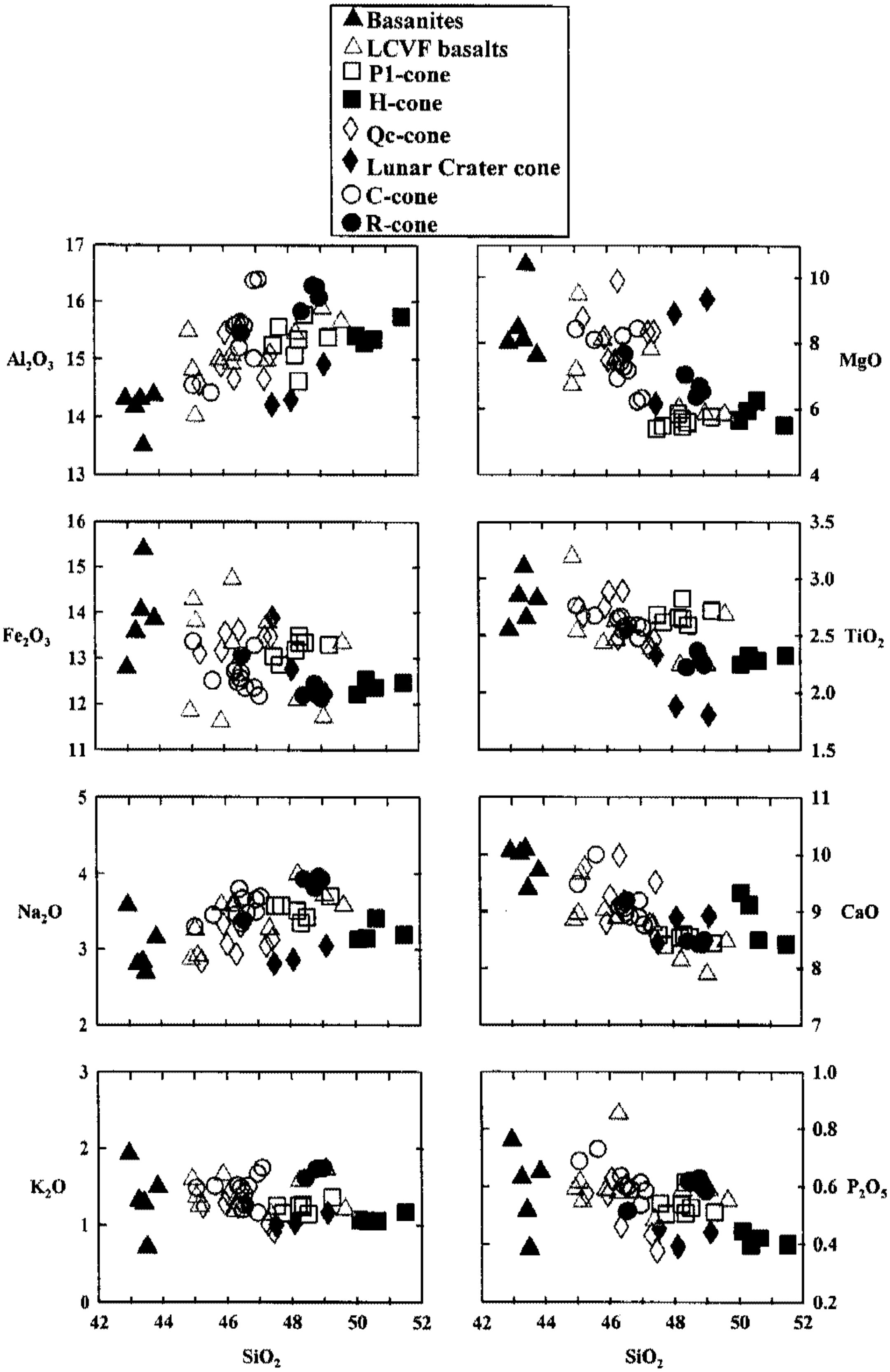

Figure 26. Harker variation diagrams show chemical variation in alkali basalts in the LCVF. Samples collected around Citadel Mountain are included for comparison. Sample locations are shown on Figures D1 and D2.

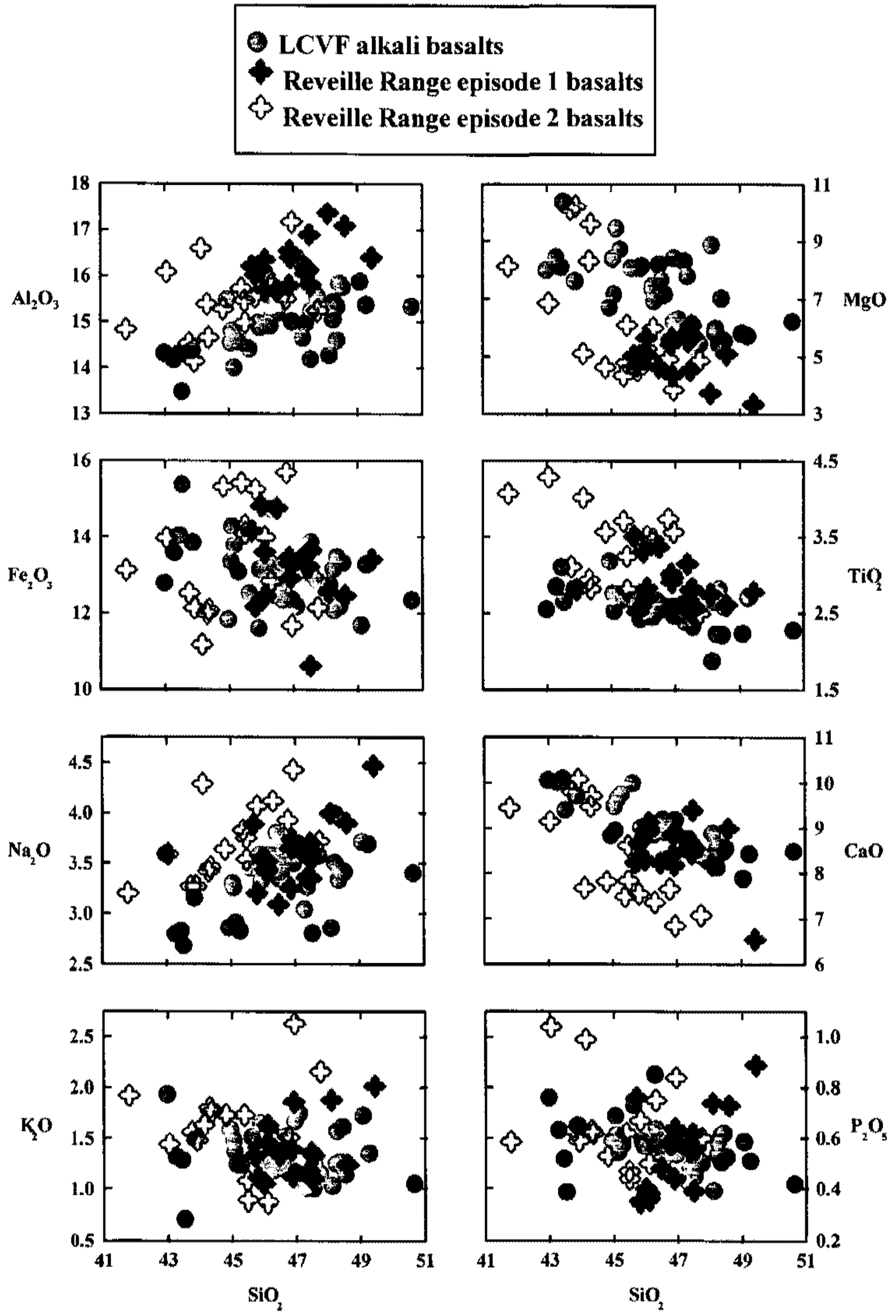

Figure 26. Harker variation diagrams compare alkali basalts in the LCVF with those in the Reveille Range. Data for Reveille Range episode 1 and episode 2 basalts is from Yogodzinski et al. (1996).

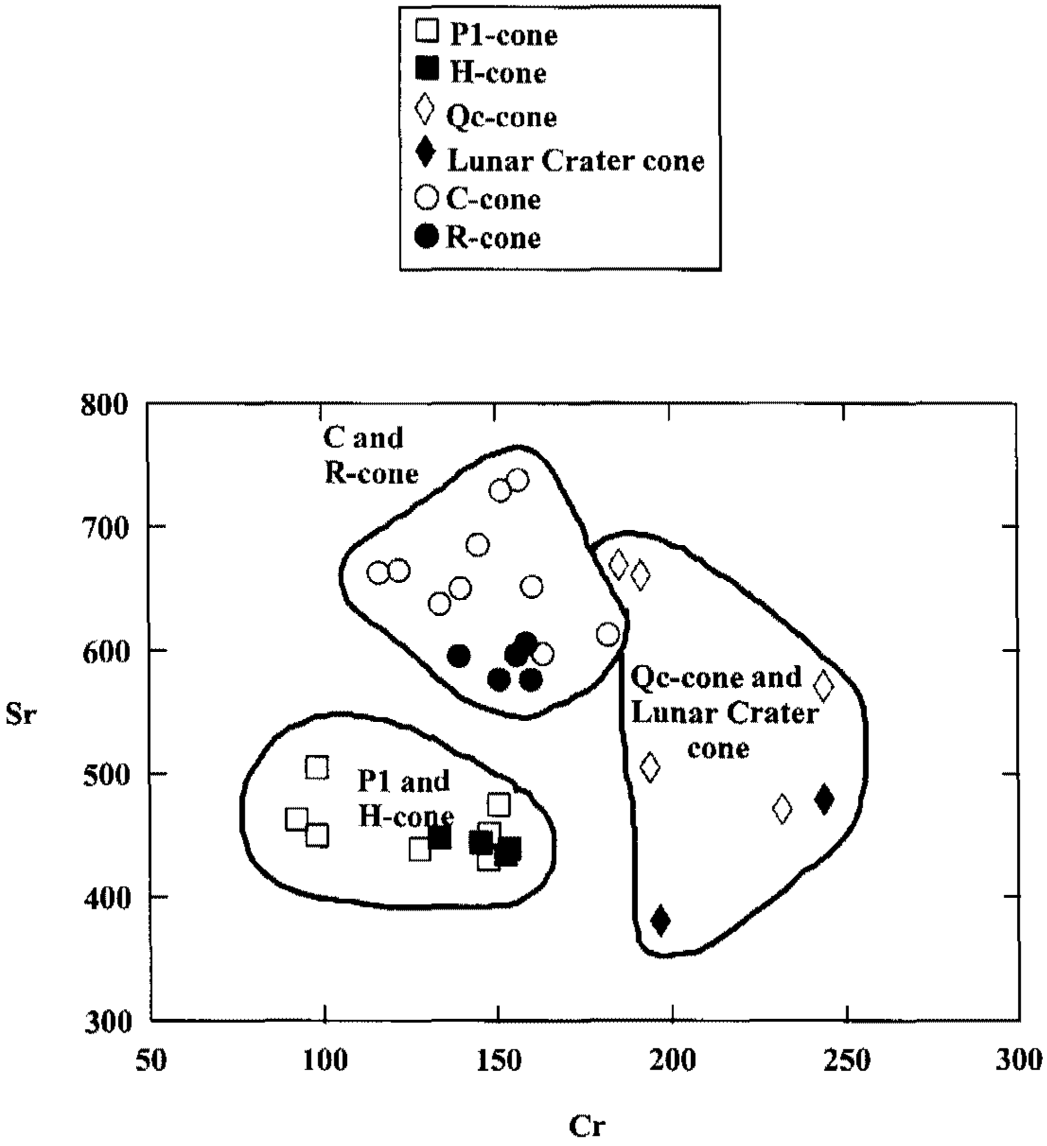

Figure 28. Citadel Mountain basalts divide into three groups on a Sr vs. Cr plot.

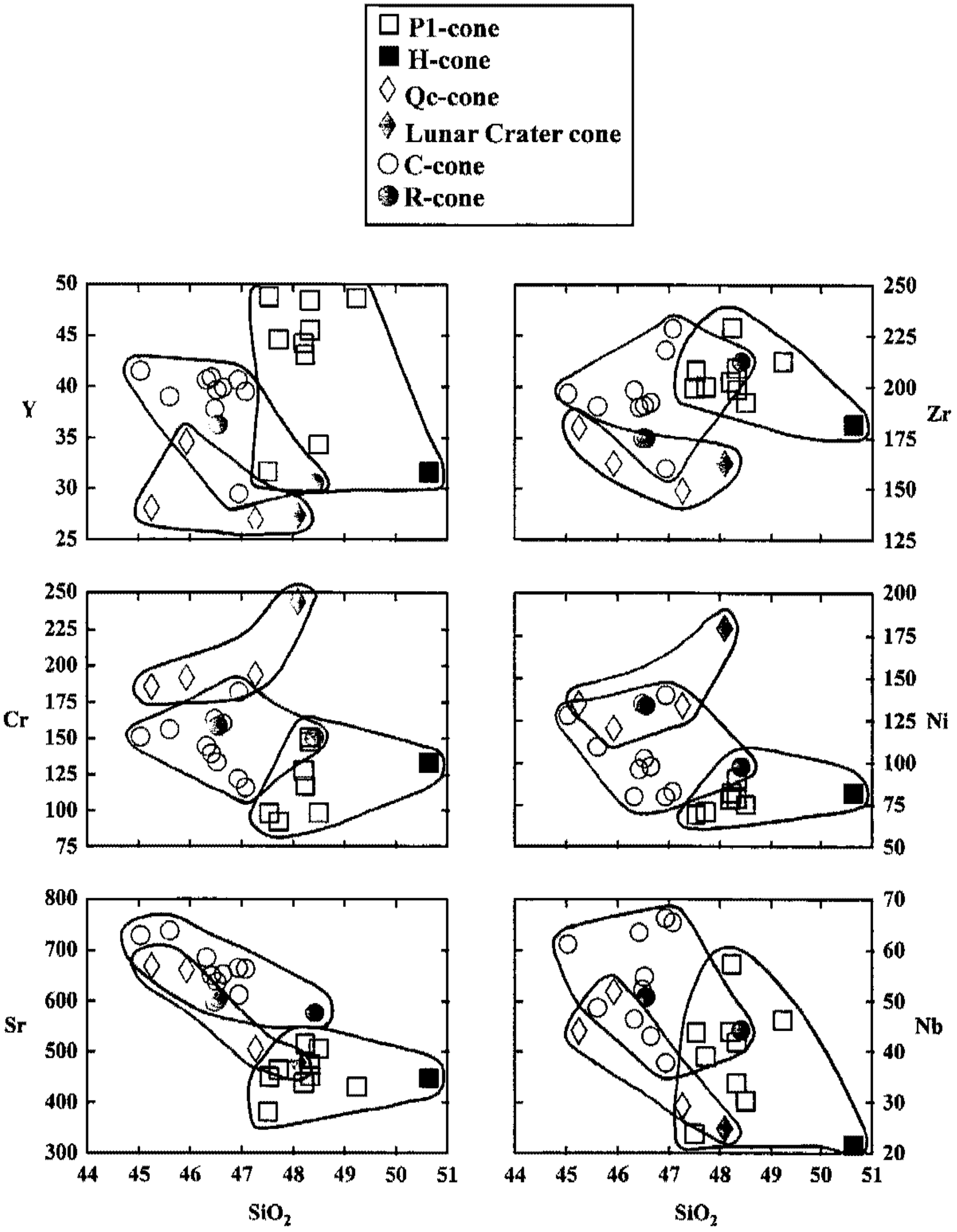

Figure 29. Harker variation diagrams show the three chemical groups differ in trace elements Y, Zr, Cr, Ni, Sr and Nb.

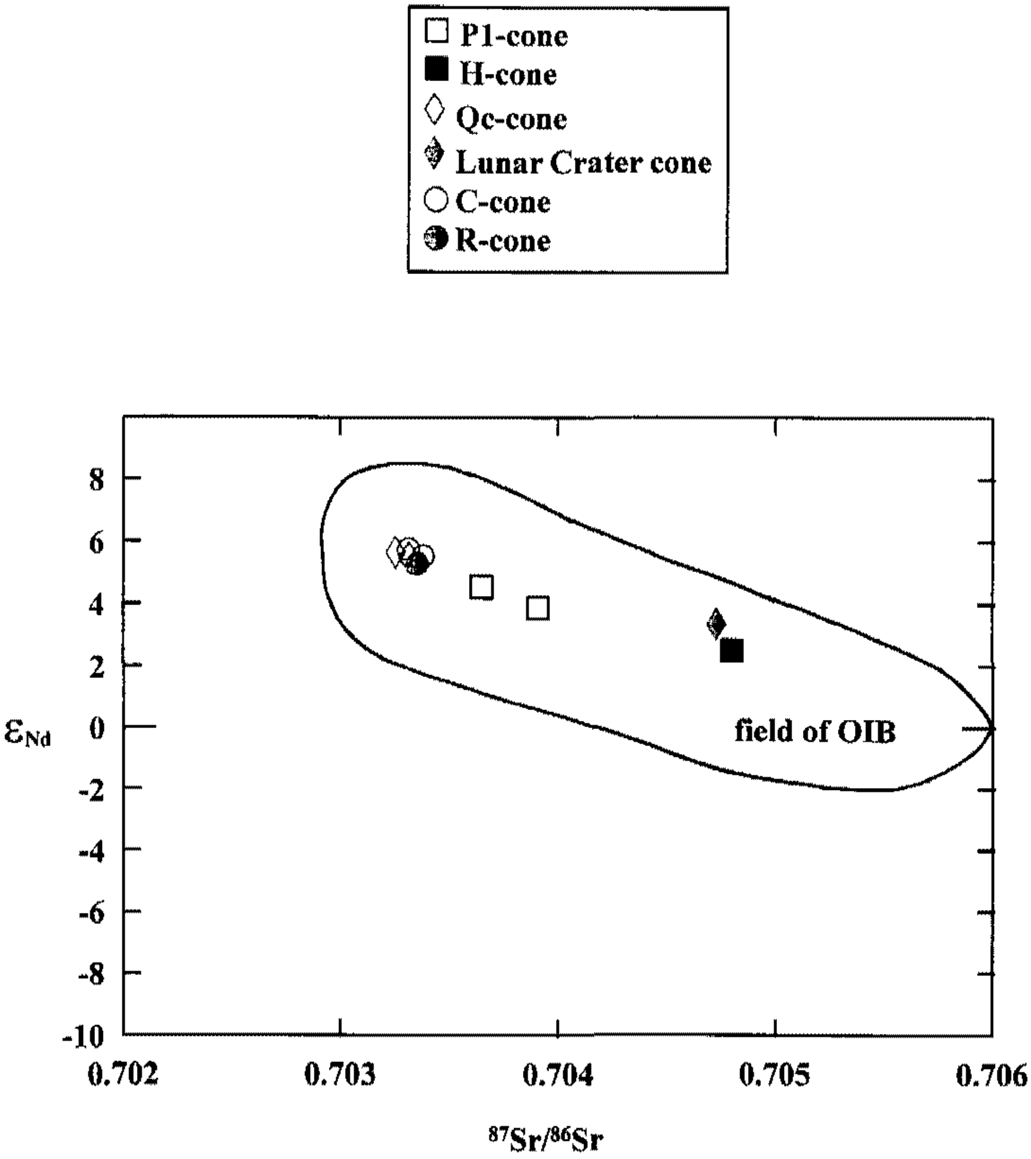

30

Figure [redacted]. Nd and Sr isotopic ratios for alkali basalts on Citadel Mountain show that all samples fall within the field of ocean island basalts (OIB) as defined by Feuerbach et al. (1993). P1, H and Lunar Crater cone basalts trend toward higher $^{87}Sr/^{86}Sr$ and lower ε_{Nd}.

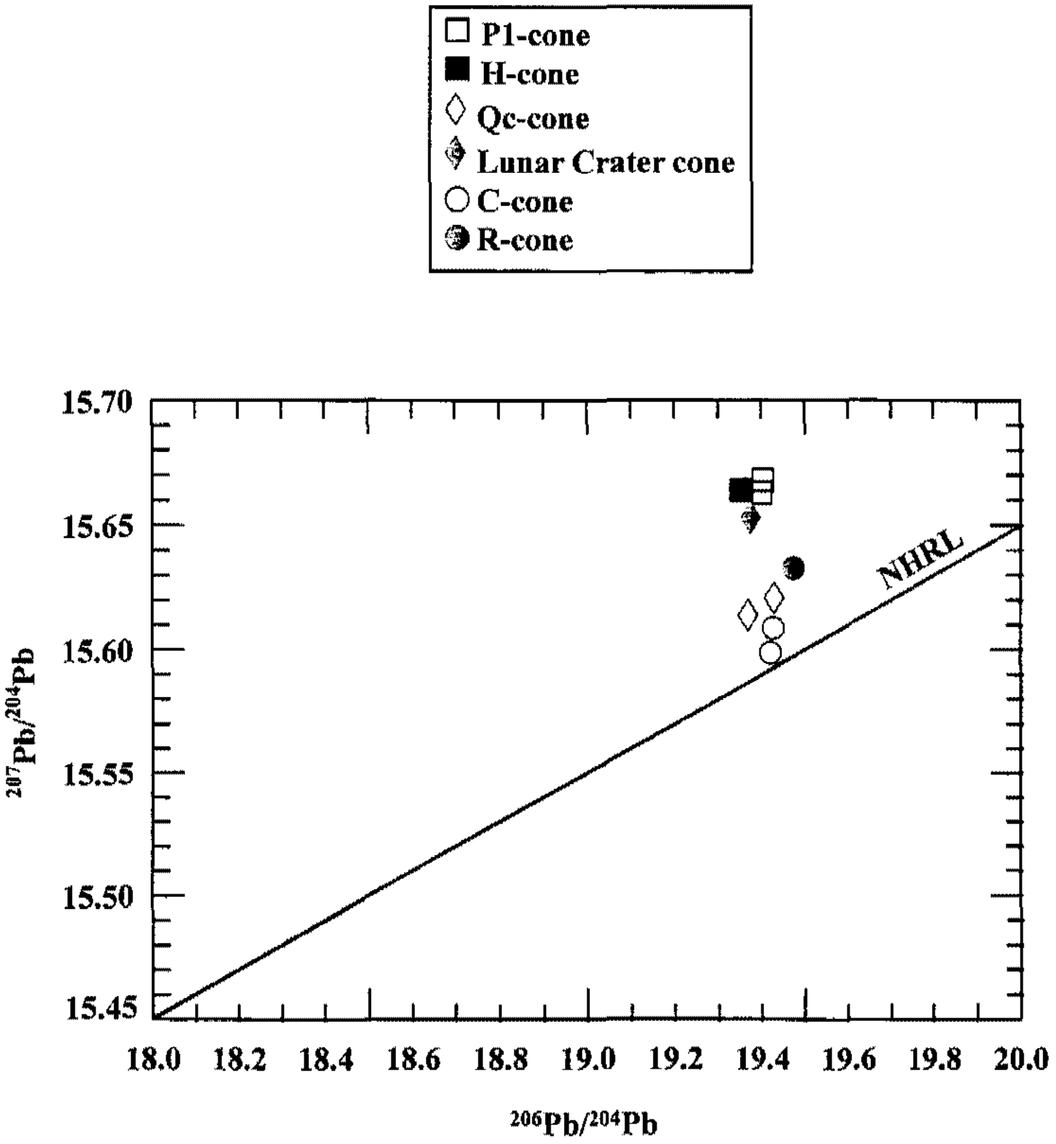

31

Figure [redacted]. Pb isotopic ratios of alkali basalts on Citadel Mountain show that Qc, C and R-cone basalts fall just above the Northern Hemisphere Reference Line (NHRL). P1, H and Lunar Crater cone basalts trend toward higher $^{207}Pb/^{204}Pb$.

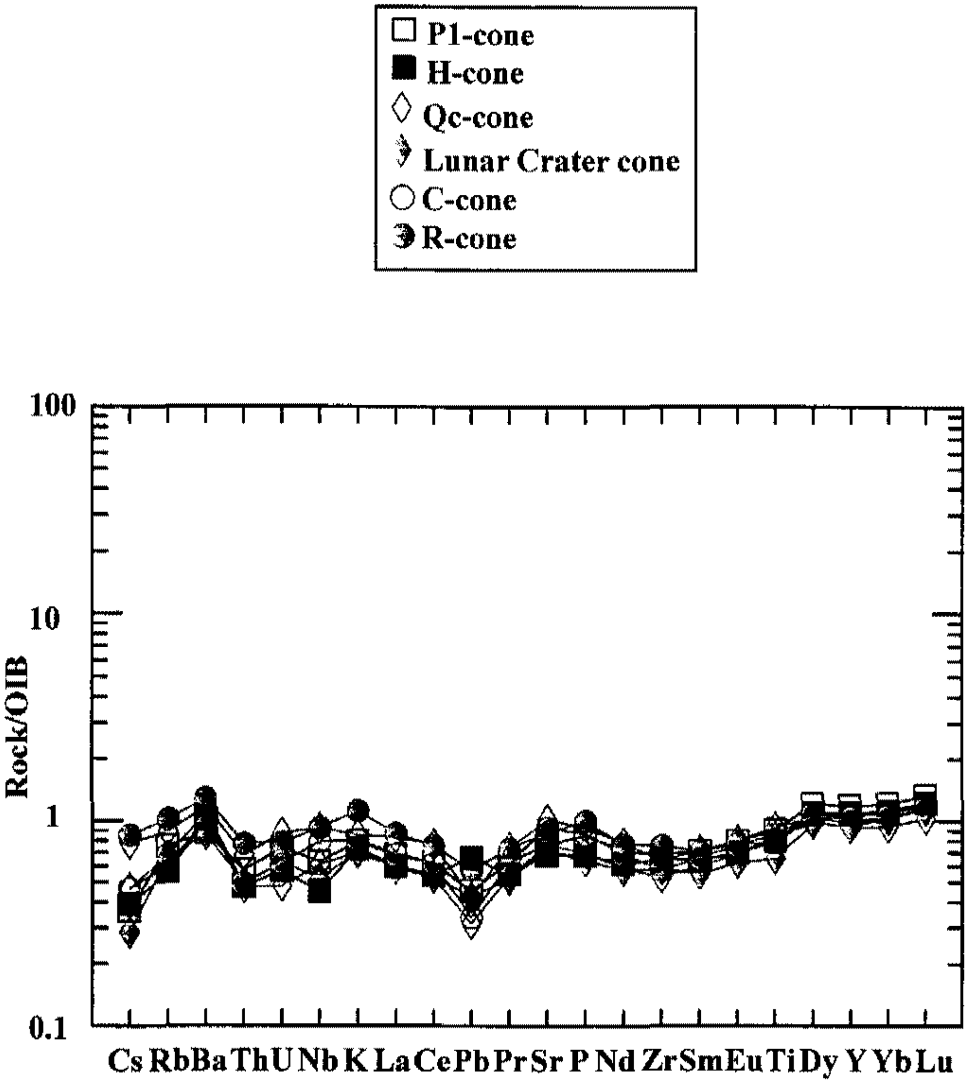

32

Figure [redacted]. OIB-normalized spider diagram shows that alkali basalts on Citadel Mountain are similar to ocean island basalts but are slightly depleted in large ion lithophile elements and light rare earth elements and are slightly heavy rare earth element enriched compared to OIB.

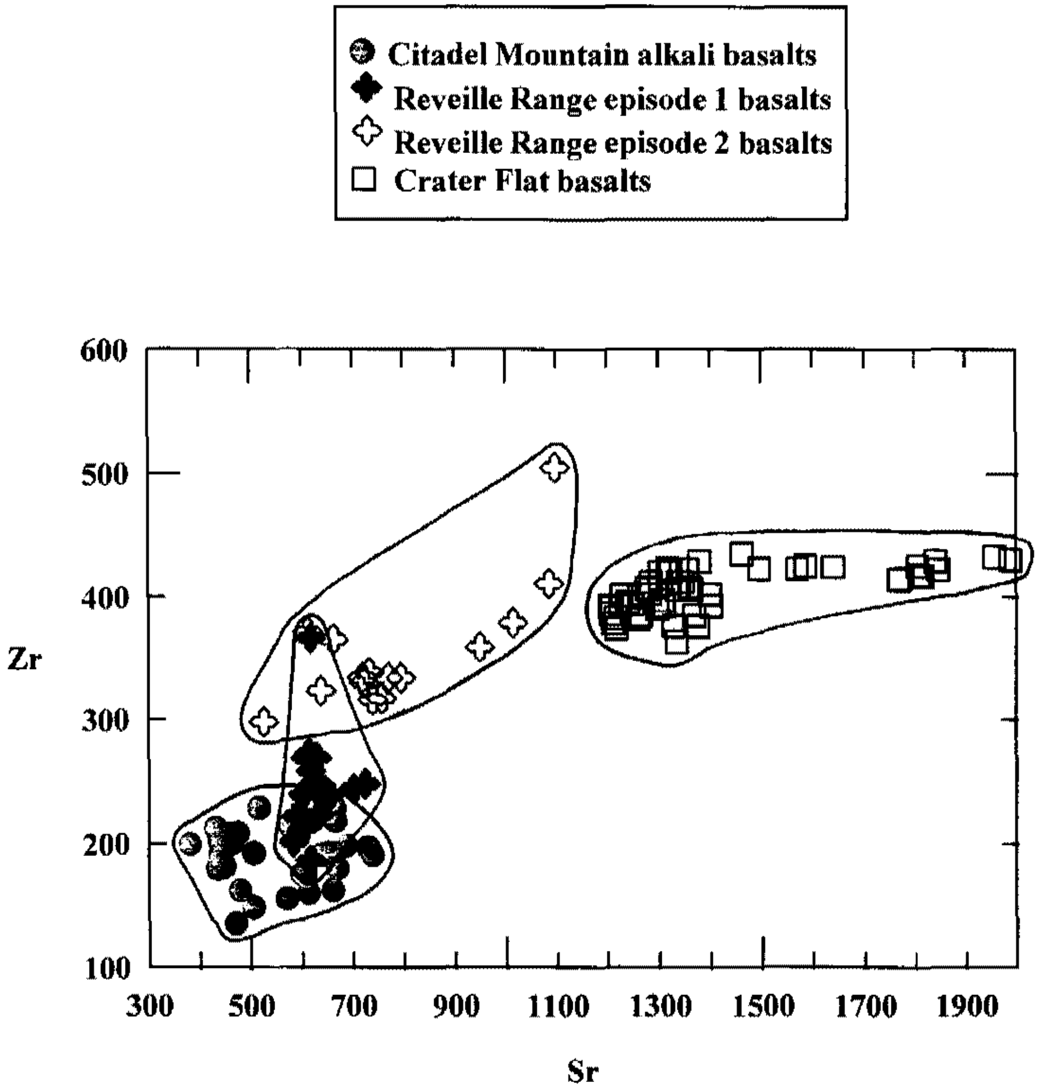

Figure 32. Many alkali basalts on Citadel Mountain are lower in Sr and Zr compared to other alkali basalt fields in the central Great Basin. Data for Reveille Range episode 1 and episode 2 basalts is from Yogodzinski et al. (1996). Data for Crater Flat basalts is from Bradshaw et al. (1994).

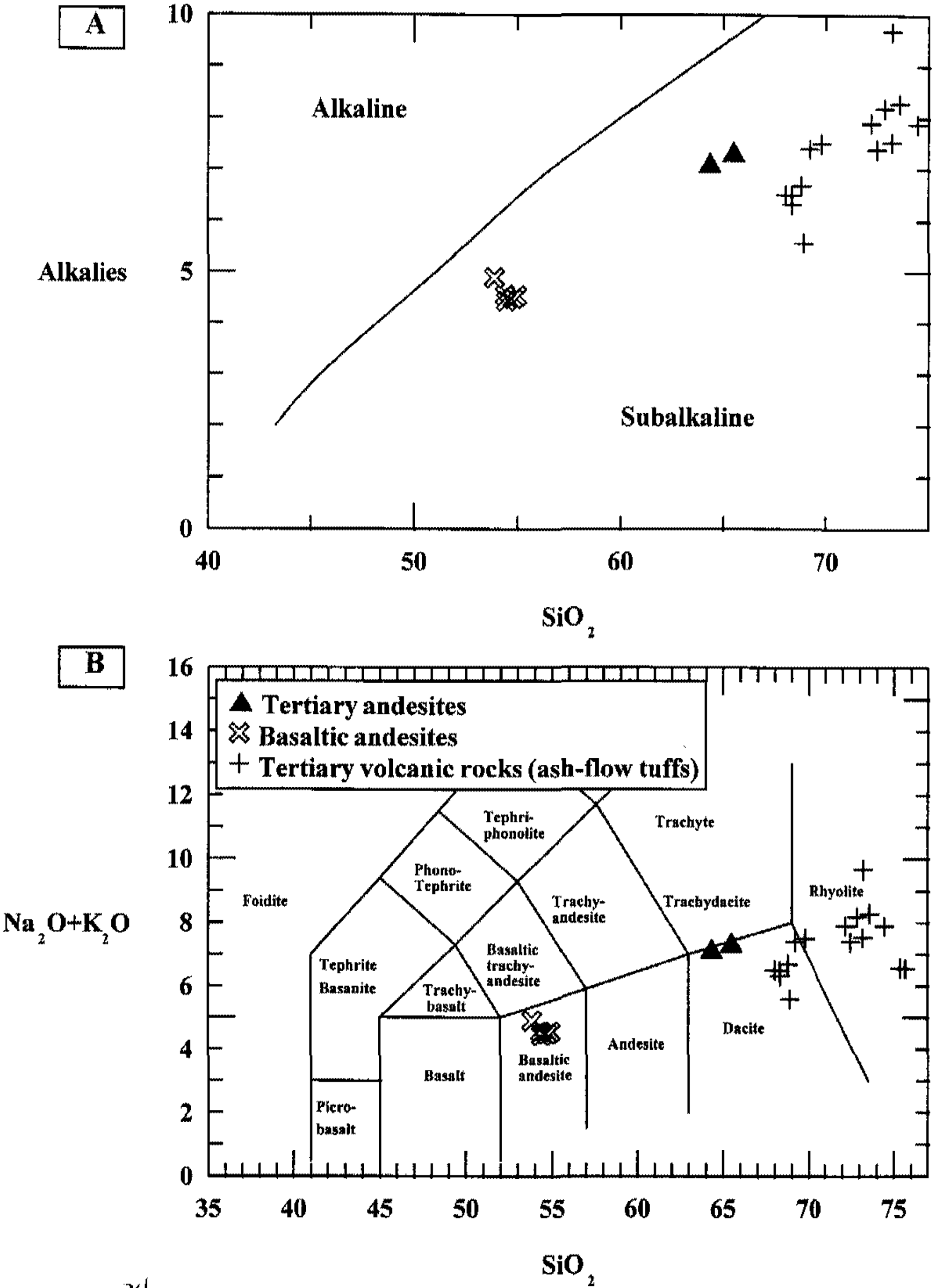

Figure 34a. Intermediate and felsic rocks are subalkaline based on a total alkalies vs. SiO$_2$ diagram. **Figure 34b.** Intermediate and felsic rocks in the LCVF are basaltic andesites, dacites and rhyolites using the classification of Lebas et al. (1986).

~~[illegible]~~ Data sources + sample locations ?

Data for Tertiary volcanic rocks and basaltic andesites [illegible] is from Rash (1995).

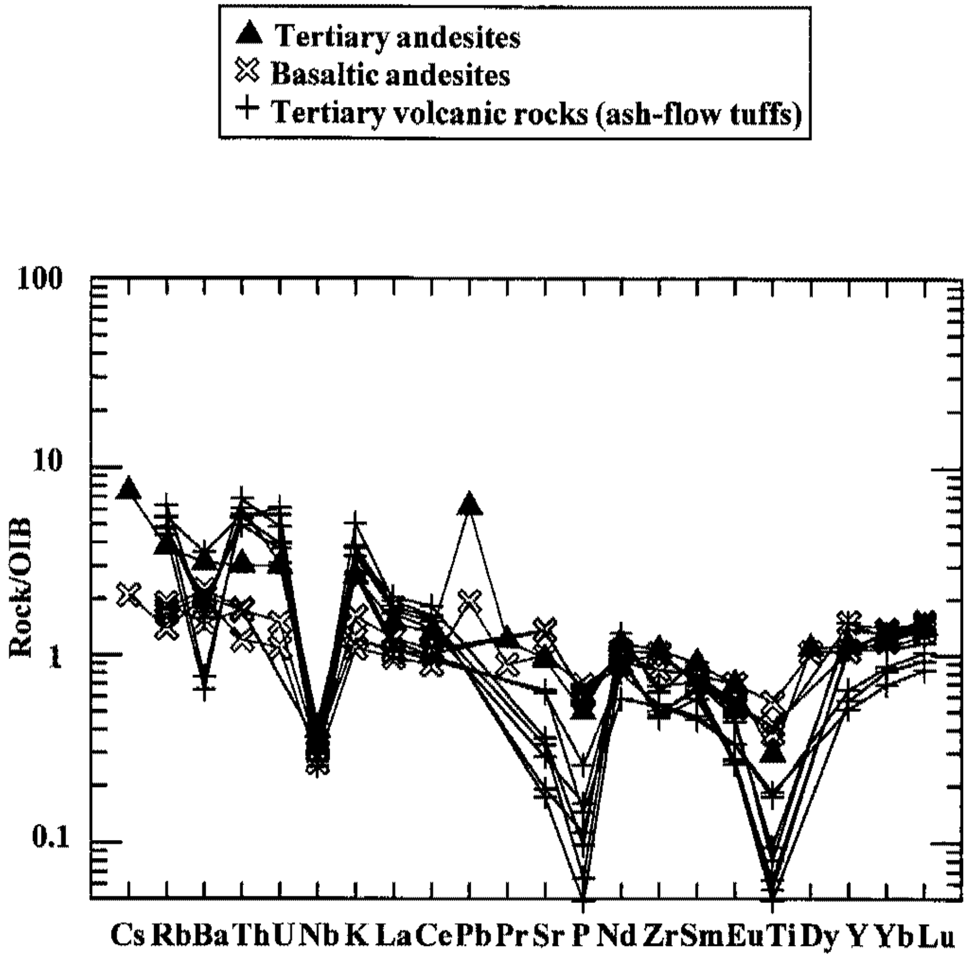

Data sources & locations of the crosses & black plusses ??

35

Figure [illegible]. OIB-normalized spider diagram shows that the intermediate and felsic rocks in the LCVF are enriched in large ion lithophile elements and light rare earth elements and show strong negative Nb, Pb and Ti anomalies.

Data for Tertiary volcanic rocks and basaltic andesites is from Rash (1995).

CHAPTER 6

INTERPRETATION

Geochemical models using fractional crystallization (FC) and assimilation fractional crystallization (AFC) and mixing were developed to explain chemical variation within each magma group and between individual magma groups. Modeling was done using the IGPETWIN computer program written by Carr (1994).

Observations

Geochemical models for Citadel Mountain alkali basalts must honor the following chemical and field observations:

1) Trace elements define three magmatic groups. The first group is formed by P1 and H-cone lavas, the second by C and R-cone lavas and the third group is Qc and Lunar Crater cone lavas.
2) Qc-cone, C-cone and R-cone basalts form a tight cluster at 0.7033 $^{87}Sr/^{86}Sr$ and +5.5 ε_{Nd}. Isotopic and trace element data indicate similarities to OIB; therefore a source in the asthenospheric mantle is likely.

3) P1-cone, H-cone and Lunar Crater cone basalts form an array on ε_{Nd} vs. $^{87}Sr/^{86}Sr$ diagrams that extends from the Qc-cone, C-cone and R-cone cluster to higher values of $^{87}Sr/^{86}Sr$ and lower values of ε_{Nd}.
4) The P1-cone, H-cone and Lunar Crater cone are the oldest cinder cones on Citadel Mountain, and Qc-cone, C-cone and R-cone are among the youngest. P1-cone erupted at 3.82 ± 0.06 Ma, H-cone at 3.82 ± 0.05 Ma and the Lunar Crater cone at 2.97 ± 0.06 Ma. Qc-cone and C-cone erupted at 1.64 ± 0.14 Ma and 1.15 ± 0.14 Ma, respectively (K/Ar whole rock dates; Kargel, 1987). R-cone formed at 0.66 ± 0.34 Ma.
5) The most primitive rocks, defined by high Cr and Ni and low SiO_2, of each magma group have compatible and incompatible element contents different from the most primitive rocks of the other groups (for example Ni, Cr and Sr).
6) The individual magma groups display different trends on compatible element plots of Ni vs. Cr.
7) Olivine, clinopyroxene and plagioclase are common phenocryst phases in all lavas.
8) Tertiary andesites and the Tuff of Buckwheat Rim comprise Citadel Mountain. Ekren et al. (1972) infers that the Tuff of Lunar Cuesta, Shingle Pass Tuff and Monotony Tuff occur in the subsurface. Tertiary volcanic rocks probably lie on Paleozoic carbonate rocks and Precambrian basement. Paleozoic sedimentary rocks are exposed in the Reveille Range to the south and in the northern Pancake Range. No exposures of Precambrian crystalline basement occur within 100 km of the LCVF.

9) Many LCVF alkali basalts are lower in Sr and Zr compared to other alkali basalt fields in the central Great Basin, except for episode 2 lavas in the Reveille Range.

Assumptions

Geochemical modeling is based on the following important assumptions:

1) Citadel Mountain alkali basalt magmas are cogenetic; in other words, magmas share similar chemistry, a similar mantle source and were erupted in a relatively short time span in a restricted geographic region. The cogenetic magmas may or may not share the same magma chamber.
2) Magmas erupted from a single cinder cone are comagmatic. This assumption is based on the observations that each cone erupted a small volume of lava and pyroclastic material over a short time span, lavas associated with each cone are chemically and isotopically similar, and that each cone (except for chemical similarities between C and R-cone lavas) has a different parent composition.
3) The FC and AFC models use distribution coefficients compiled by the Center for Volcanic and Tectonic Studies (CVTS) over a five year period from the following sources: Luhr et al., 1985; Wilson, 1989. Distribution coefficients change with composition, therefore, distribution coefficients used for the models are for mafic rocks (Table 2).
4) Considering the small volume of the LCVF and its nearly 3 million year eruptive history, it is unlikely that single magma chambers can survive the entire life time of the volcanic field. Therefore simple FC or AFC models involving a single magma body are probably not suitable for explaining chemical variations between magma

groups. Production of similar parental magmas by multiple partial melting events over the life of the field, however, is a likely possibility.

Model Descriptions

Preferred Model to Explain Geochemical Differences Between Magma Groups

The preferred model to explain the isotopic differences between magmatic groups is the mixing of asthenospheric derived Qc, C and R-cone type magmas with a lithospheric mantle melt, similar to the Tertiary andesite in isotopic composition, to produce P1, H and Lunar Crater cone magmas. Tertiary andesites on Citadel Mountain are evolved rocks with 65 wt. % SiO_2, elevated LIL and LREE (nearly 200 x chondrite in La), and relatively low Cr (13 ppm) and Ni (48 ppm) compared to typical alkali basalt (150-300 ppm Cr and 100 to 200 ppm Ni). A trough at Nb on OIB normalized spider diagrams combined with high $^{87}Sr/^{86}Sr$, low ε_{Nd} and high $^{206}Pb/^{204}Pb$ and $^{207}Pb/^{204}Pb$ suggests that the Tertiary andesite was originally produced by magmas which at least in part were generated by melting of the lithospheric mantle. Because of its complex and evolved nature, the Tertiary andesite itself was probably not involved in the production of parent magmas for the P1, H and Lunar Crater cone magmas. I suggest instead that the magma that mixed with rising asthenospheric melts was the parent magma for the Tertiary andesite; a typical lithospheric mantle melt with lower SiO_2 and Sr, higher Cr and Ni, and lower or equivalent incompatible element content but with similar isotopic signatures as the Tertiary andesite. The SiO_2 content of the lithospheric melt could not be higher than 60 wt. %. This is based on the calculation that at least 23% by volume lithospheric melt must be added to the rising asthenospheric magmas to produce H-cone lavas, 19% to produce Lunar Crater cone lavas and about 10% to produce P1-cone lavas (Figure 36). Adding this volume of lithospheric melt would produce the observed increase of 5 wt. % SiO_2 in H-cone lavas and 2 wt. % in P1-cone lavas over the SiO_2 content of Qc, C and R-cone lavas. The lower Sr required in the lithospheric melt is a problem; most lithospheric mantle melts (e.g., at Crater Flat) have higher Sr than required in the model lithospheric melt (>1000 rather than 300-400 ppm). Possibly the mantle in the Citadel Mountain area is lower in Sr than in other areas. This contention is supported by the observation that asthenospheric melts represented by the youngest eruptions in the LCVF are lower in Sr than those in most other parts of the central Great Basin (see Chapter 5; Figure 33).

Lithospheric melts may have formed by melting "veinlets[*] " in the mantle lithosphere. Melt metasomatism of the lithospheric mantle to produce basaltic or gabbroic veinlets was originally suggested by Harry and Leeman (1995). In their model melt metasomatism occurred in the Precambrian and produced basaltic or gabbroic veinlets encased by mantle peridotite. Most lithospheric mantle veinlets melted early in the Basin and Range extensional event resulting in large volumes of calc-alkaline andesite and related intermediate volcanic rocks. Because the lithospheric mantle veinlets were isolated from the convecting asthenosphere since the Precambrian, their

---

[*] The lithospheric mantle veinlets represent magmas trapped in the mantle lithosphere from a previous melting event. The shape or geometry of the veinlet is unknown, however, they may take the form of dikes, sills or small intrusions (Harry and Leeman, 1985).

isotopic systems evolved from OIB or MORB values to present day values of $^{87}Sr/^{86}Sr$ = 0.7085 and $\varepsilon_{Nd} = -8$. Therefore, by the late Cenozoic the lithospheric mantle veinlets would have isotopic ratios similar to the Tertiary andesite lavas comprising the basement rock of Citadel Mountain. Assuming some of the lithospheric mantle veinlets survived until Pliocene and Quaternary basaltic volcanism began in the Pancake Range, they may have been melted at the onset of magmatism. Rising asthenospheric melts mixed with the melted lithospheric mantle veinlets in the mantle lithosphere. The remaining lithospheric mantle veinlets would be exhausted during the early melting events and would not be available later; therefore, younger Citadel Mountain basalts would rise through the lithospheric mantle without interacting with lithospheric mantle veinlets and would have compositions directly representing their asthenospheric source. The advantage of this model is that interaction of magmas occurs in the lithospheric mantle were magma mixing can effectively take place. Magma interaction at high temperature in the lithospheric mantle would probably be thorough and the resulting mixed magmas would not show any petrographic or field evidence of this event. The model also satisfactorily explains the reason that early magmas display higher $^{87}Sr/^{86}Sr$ and lower ε_{Nd} than younger magmas and suggests that the chemical transition between older P1, H and Lunar Crater cone eruptions and the younger Qc, C and R-cone eruptions is related to the exhaustion of lithospheric mantle veinlets in the mantle. The validity of this model depends on the presence of lithospheric mantle veinlets in the mantle lithosphere with the proper chemistry and isotopic signature. The question of whether lithospheric mantle veinlets exist in the mantle lithosphere is a matter of speculation. The isotopic character of the lithospheric mantle selected for LCVF models, however, is representative of typical lithospheric mantle in the Great Basin and southern Basin and Range (Fitton et al., 1991; Feuerbach et al., 1993) (Figure 36).

Alternative Models

Alternative models involve the melting of a laterally heterogeneous mantle and the contamination of asthenospheric melts with a variety of types of rocks known to exist in the basement on or near Citadel Mountain. Most of the proposed contaminants have the proper isotopic ratios to serve as a contaminant, but must be eliminated because major and/or trace element contents are either too high or low. Possible contaminants that were considered include average Archean lower crust and Precambrian upper crust (Taylor and McLennan, 1985), Paleozoic carbonate rocks, Tertiary volcanic rocks (ash-flow tuffs), and Miocene basaltic andesites.

Heterogeneous Mantle

Partial melting of a mantle with lateral compositional variability may result in lavas with significantly different isotopic ratios in a single volcanic field. If it is assumed that melting occurred at the same depth in the mantle, but that the mantle is compositionally heterogeneous at the kilometer scale at that depth, differences in isotopic ratios would reflect these lateral differences in mantle lithology and chemistry. The correlation of age with chemistry of lavas and the lack of correlation of age or chemistry with geographic position argue against this model. Younger Qc, C and R-cone magmas are distributed across the entire length of Citadel Mountain, but have similar isotopic and trace element signatures. Older P1, H and Lunar Crater cone lavas are isotopically enriched and also distributed across the mountain. The observation that older lavas are isotopically enriched and younger lavas isotopically depleted wherever they erupt on Citadel Mountain suggests that random lateral compositional variations in the mantle are not the cause of the isotopic variations observed in the rocks. Based on these arguments, lateral heterogeneity of the mantle can be ruled out as the sole cause of the compositional variations between magma groups.

Partial melting of the mantle at various depths may also result in lavas with different isotopic ratios. If it is assumed that older lavas melted shallow isotopically enriched mantle and younger lavas melted deeper, more depleted mantle, differences in mantle depth would be reflected in different isotopic ratios and trace element abundances. Isotopic variation occurs as a single trend from the isotopically depleted Qc, C and R-cone cluster to more isotopically enriched P1, H and Lunar Crater cone lavas (see Chapter 5; Figures 30 and 31); however, trace element abundances are similar (see Chapter 5; Figure 29) and do not suggest both enriched and depleted mantle sources. OIB-normalized spider diagrams for both groups are the same with only small changes in Nb and Pb between older and younger groups (see Chapter 5; Figure 32).

Based on these observations, both heterogeneous mantle models are discounted.

Crustal Contamination

Archean lower crust is characterized by low ε_{Nd} and $^{87}Sr/^{86}Sr$, low $^{206}Pb/^{204}Pb$ and high $^{207}Pb/^{204}Pb$ compared to Proterozoic and younger basement rocks (Taylor and

McLennan, 1985). Archean lower crust is discounted as a possible contaminant because P1, H and Lunar Crater cone alkali basalts trend to higher $^{206}Pb/^{204}Pb$ toward the field of upper crustal material (Figure 37). The trace elements Zr, Sr and Nb are also too low in Archean lower crust to be a contaminant for P1, H and Lunar Crater cone alkali basalts (Figure 38).

Precambrian upper crust of intermediate or felsic composition has high $^{87}Sr/^{86}Sr$, low ε_{Nd}, and high $^{206}Pb/^{204}Pb$; therefore based on isotopes alone, Precambrian upper crust is a possible contaminant. Furthermore, trace element contents of average Precambrian upper crust (Taylor and McLennan, 1985) are suitable to consider these rocks as a contaminant to produce the parent magma of P1, H and Lunar Crater lavas (Figure 39). Precambrian upper crust contains 25 ppm Nb, 350 ppm Sr and 190 Zr compared to 65 ppm Nb, 740 ppm Sr and 230 ppm Zr for the most primitive alkali basalt on Citadel Mountain. P1, H and Lunar Crater parent magmas lie between the primitive alkali basalts and Precambrian upper crust on Zr vs. Sr and Nb vs. Sr diagrams (Figure 39). If Precambrian upper crust were assumed to be a contaminant, these rocks would have to be mafic in composition with no more than 60 wt. % SiO_2; however, there is no evidence that mafic crust lies beneath this area in the Great Basin. I suggest, based on trace element, isotopic and major element data, that Precambrian upper crust is a possible but unlikely contaminant.

Paleozoic carbonates have high $^{87}Sr/^{86}Sr$ (0.7085) and low ε_{Nd} (-10) and may be permissible contaminants (Figure 40). In the Reveille Range, episode 1 basalts produce a trend toward higher $^{87}Sr/^{86}Sr$ and lower ε_{Nd} while the episode-2 basalts cluster at low

$^{87}Sr/^{86}Sr$ and high ε_{Nd}. Yogodzinski et al. (1996) suggested that episode 1 basalts assimilated carbonate in the upper crust while episode 2 basalts represent uncontaminated mantle melts. Citadel Mountain alkali basalts behave in a similar fashion. The younger lavas cluster at low $^{87}Sr/^{86}Sr$ and high ε_{Nd} and the older lavas follow the trend toward the field of the carbonate rocks (Figure 41). Another major argument made by Yogodzinski et al. (1996) for carbonate assimilation is the increase in Sr between uncontaminated (episode 2) and contaminated basalt (episode 1). AFC models developed by Yogodzinski et al. (1996) on $^{87}Sr/^{86}Sr$ vs. Sr plots suggest that episode 1 formed from episode 2 type magmas by assimilation of carbonate ($r = 0.35$) and fractional crystallization with the bulk distribution coefficient varying from 1.15 to 0.85. Younger Citadel Mountain basalts are similar in chemistry to episode 2 magma in the Reveille Range, but older lavas differ by being lower in Sr and falling outside of the AFC envelope calculated for the episode 1 Reveille Range basalts (Figure 42). I suggest that carbonate assimilation is an unlikely explanation of the chemistry of the older (P1, H and Lunar Crater cones) lavas on Citadel Mountain, because Sr is lower, not higher as expected if carbonate contamination occurred, in the more isotopically enriched older basalts. In addition, AFC models (to produce P1, H and Lunar Crater cone magmas from Qc, C and R-cone type magma) involving carbonate contamination would require a bulk distribution coefficient for Sr of about 1.6 (Figure 42). This value is too high considering that feldspar does not appear to be an important fractionated phase in models to explain intragroup variations (see next section).

Although the Shingle Pass and Monotony tuffs representative of the ash-flow section in the basement of Citadel Mountain have suitable isotopic and trace element characteristics to be contaminants (high $^{87}Sr/^{86}Sr$, low ε_{Nd}, high $^{206}Pb/^{204}Pb$ and low Zr, Sr and Nb; Figures 43 and 44), they are eliminated from consideration because nearly 40% by volume of tuff must be added to Qc, C and R-cone magma to produce the isotopic and trace element abundances in P1, H and Lunar Crater cone magmas. The addition of such a large amount of contaminant with SiO_2 ranging from 70-75 wt. % would require considerable heat input in the uppermost crust; an unlikely situation considering the low volume of the LCVF system. Furthermore, the addition of a large amount of tuff would significantly change the major element content of the parental basalts to produce andesite or dacite. Based on these observations, ash-flow tuff can be eliminated as a contaminant.

The 21.79 Ma basaltic andesites which crop out 11 km east of Citadel Mountain have suitable $^{87}Sr/^{86}Sr$ and ε_{Nd} and trace element concentrations (especially Zr, Sr and Nb), but their $^{206}Pb/^{204}Pb$ is too low (Figure 45) to be a contaminant. Furthermore, the basaltic andesite does not occur in the basement of Citadel Mountain. For these reasons, I exclude the basaltic andesites as a contaminant.

I conclude that of these alternative models only mafic Precambrian upper crust is a permissible contaminant. Although permissible, I consider its involvement to be doubtful because mafic Precambrian upper crust is not known to occur in the subsurface of Citadel Mountain.

Fractional Crystallization Models:
Intragroup Variation

FC models use the equation $C_{liq}^{l} = C_{o} F^{Di-1}$ (Neuman et al., 1954) where C_{liq}^{l} is the concentration of the element in the liquid phase, C_{o} is the original concentration of the element in the liquid phase before fractional crystallization, F is the fraction of liquid remaining after fractional crystallization, and Di is the bulk distribution coefficient for that element. FC models were developed using a compatible element plot of Ni vs. Cr. Ni is compatible in olivine and Cr is compatible in clinopyroxene. Compatible elements decrease in abundance with increasing fractional crystallization of mineral phases. Fractionation of olivine results in rapid decrease in Ni concentration until about 20% olivine is fractionated and then in higher Cr abundances for larger amounts of olivine fractionation. Fractionation of clinopyroxene results in rapid decrease in Cr until about 30% clinopyroxene is fractionated and then in lower Ni values with additional fractionation (Figure 46). The olivine and clinopyroxene fractionation vectors define an envelope that contains all possible fractionation models that involve these minerals. If data points for the rocks to be modeled lie within the envelope, the observed chemical variation may be modeled by some proportion of olivine and clinopyroxene fractionation.

Chemical variation of C-cone lavas can be explained by 9% fractionation of 60% clinopyroxene and 40% olivine (Figure 47). The R-cone data can be explained by 5% fractionation of 25% clinopyroxene and 75% olivine (Figure 47). Similar age, geographic proximity, similar mineralogy, comparable chemistry and identical isotopic ratios suggest that C and R-cone lavas may have shared the same magma chamber.

The Qc-cone data is scattered. The scatter may be due to the fact that Qc-cone is composed of four coalesced cinder cones, each with a different evolution history. To model these complex cones, a model envelope was developed rather than a simple model. The boundaries of the model envelope are 5% fractionation of 25% clinopyroxene and 75% olivine and 6% fractionation of 60% clinopyroxene and 40% olivine. The Qc-cone flow data points fall within this model envelope (Figure 48). Lunar Crater cone data can be explained by 8% fractionation of 52% clinopyroxene and 48% olivine (Figure 48).

Chemical variation in P1-cone lavas can be explained by 8% fractionation of 85% clinopyroxene and 15% olivine (Figure 49). H-cone flow data can be explained by 4% fractionation of 65% clinopyroxene and 35% olivine (Figure 49).

It is concluded that magma commingling/mixing is an important event in the petrogenesis of older alkali basalts on Citadel Mountain, as described earlier in this chapter. P1-cone, H-cone and Lunar Crater cone magmas produce an array that points toward the Tertiary andesite isotopic composition on ε_{Nd} vs. $^{87}Sr/^{86}Sr$ and $^{207}Pb/^{204}Pb$ vs. $^{206}Pb/^{204}Pb$ diagrams (Figure 50). P1-cone evolved magmas point toward Tertiary andesite trace element compositions on Cr vs. Ni and Sr vs. Nb plots (Figure 51). Based on trace element observations, small amounts of assimilation ($r = 0.1$ or less; <1% by volume) of Tertiary andesite are permissive, but are not required in the models to produce the evolved P1-cone magmas.

Summary

The fractional crystallization models are based on the assumption of different batches of magma generated from a similar mantle source over a limited period of time. The lavas from individual cinder cones are comagmatic with the exception of C-cone and R-cone lavas which may have shared the same magma chamber. The older P1, H and Lunar Crater cone magmas may have originally been similar to those from Qc, C and R-cones but were contaminated during their rise through the mantle lithosphere. P1-cone magma may have undergone two contamination events. The first event involved mixing of lithospheric mantle veinlets with asthenospheric melts to produce the P1-cone parent magma (Figure 52). A possible second contamination event involved assimilation of <1% by volume of the Tertiary andesite during fractional crystallization to produce the evolved P1-cone rocks (Figure 52). H-cone and Lunar Crater cone magma underwent the first contamination event producing their respective parent magmas, however, additional contamination of H-cone and Lunar Crater cone lavas during evolution can not be evaluated because of a lack of isotope data. The younger C and R-cone magmas (perhaps from the same magma chamber) and Qc-cone magma underwent fractional crystallization but were not contaminated, rather they reflect their asthenospheric mantle source (Figure 52). The alkali basalts on Citadel Mountain represent a simple magmatic system. Magmas of all volcanoes on Citadel Mountain have a similar mantle source, but older magmas underwent small amounts of contamination to produce P1-cone, H-cone and Lunar Crater cone parent magmas followed by fractional crystallization of less than 10%. Younger magmas were probably not contaminated and evolved solely by small amounts of fractional crystallization.

As mentioned on page 66, I am going to insist on seeing the sources of these cited.

Table 2: Bulk Distribution Coefficients

Element	Plagioclase	Clinoproxene	Olivine	Hornblende
Rb	0.07	0.03	0.01	0.05
Ba	0.16	0.02	0.01	0.22
Sr	1.8	0.12	0.01	0.19
Cr	0.01	10.0	0.1	30.0
Ni	0.01	3.5	15.0	8.0
Zr	0.01	0.2	0.1	0.1
Nd	0.14	0.2	0.001	0.76
Y	0.05	0.33	0.001	2.1

Bulk distribution coefficients compiled by the Center for Volcanic and Tectonic Studies (CVTS) from the following sources: Luhr et al. (1985) ; Wilson (1989).

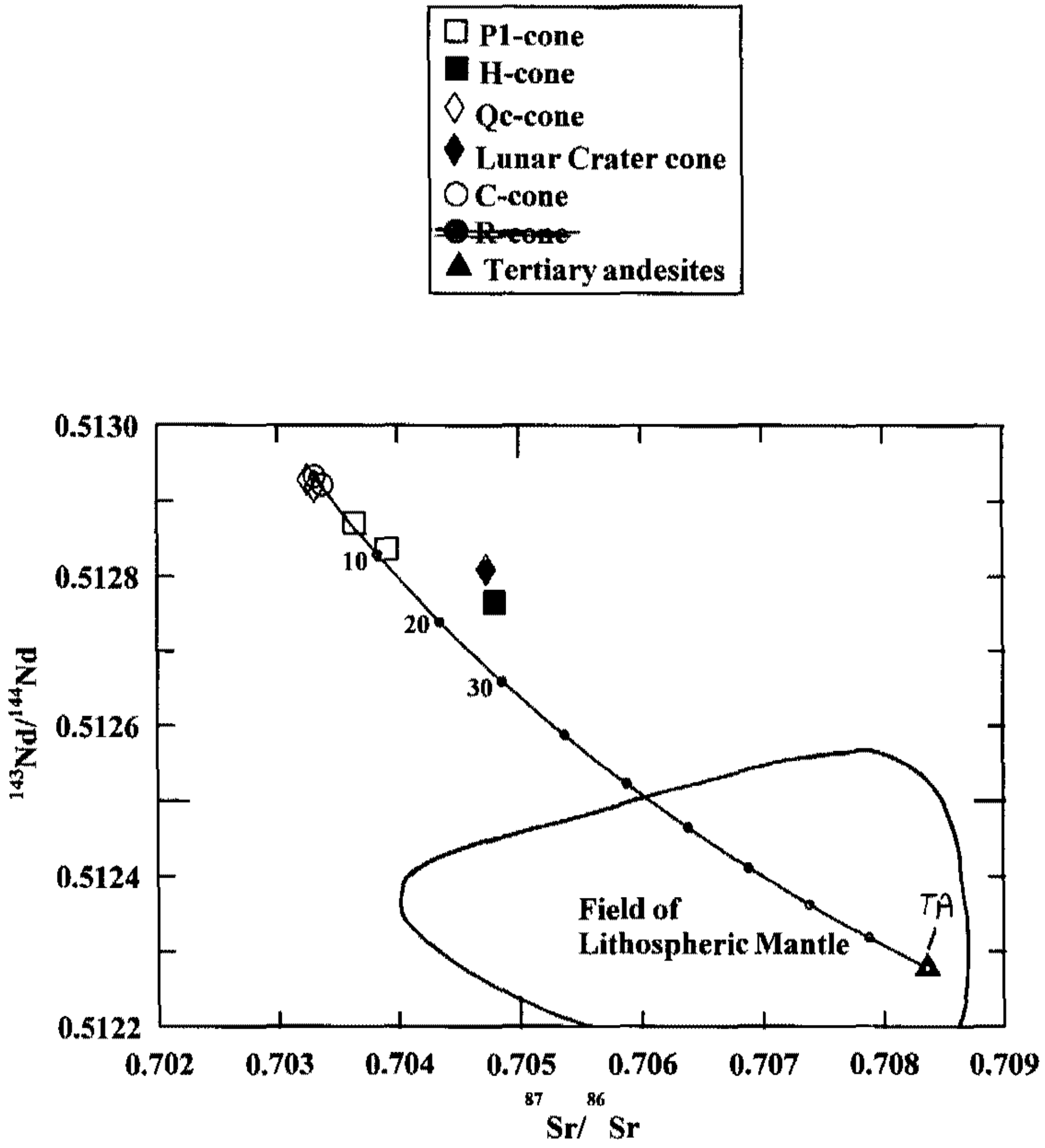

Figure [redacted] 36. The addition of 10% by volume of lithospheric melt to rising asthenospheric magmas may produce P1-cone lavas, 19% to produc Lunar Crater cone lavas or [redacted] 23% may produce H-cone lavas. Note that composition of the lithospheric mantle is approximated by using the Tertiary andesites that crop out on Citadel Mountain. The mixing curve on the figure is just an example, therefore, of the evolutionary process.

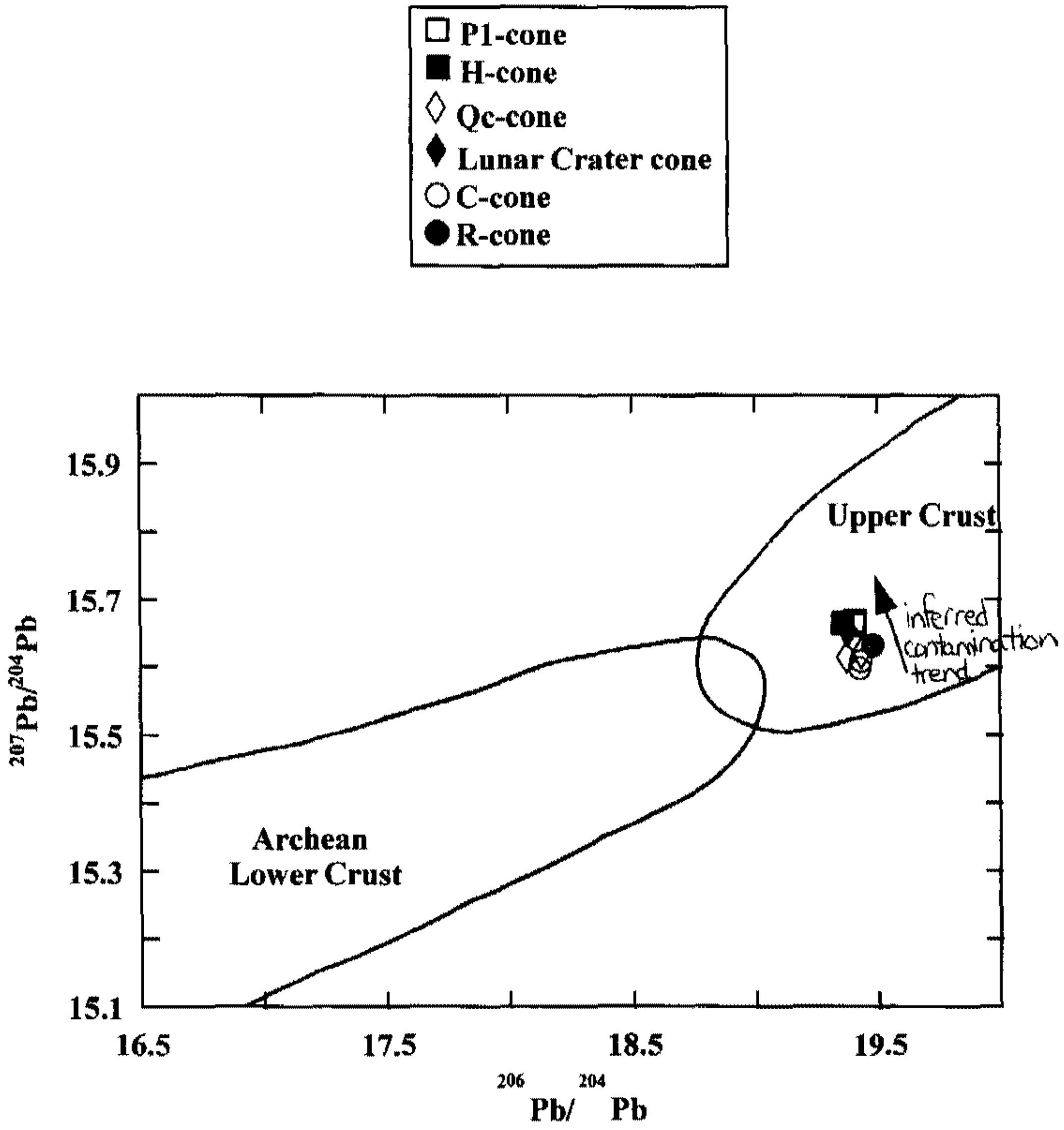

37

Figure [illegible]. Pb isotopic ratios show that alkali basalts on Citadel Mountain trend toward the field of upper crust rather than toward the Archean lower crust field after Wilson (1989).

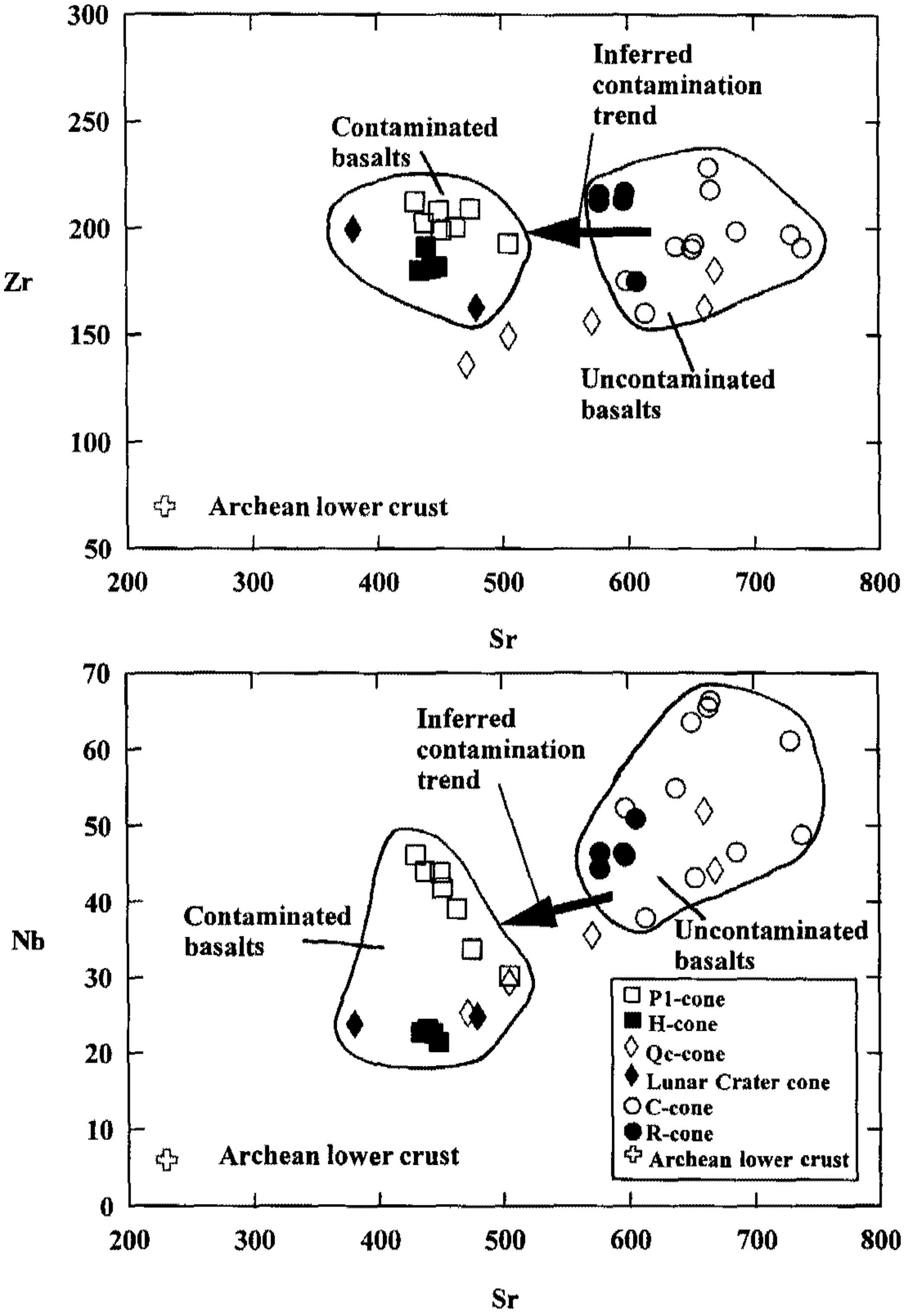

Figure 38. Archean lower crust is too low in Zr, Sr and Nb to be a suitable contaminant for P1, H and Lunar Crater cone basalts. Archean lower crust chemistry is from Taylor and McLennan (1985).

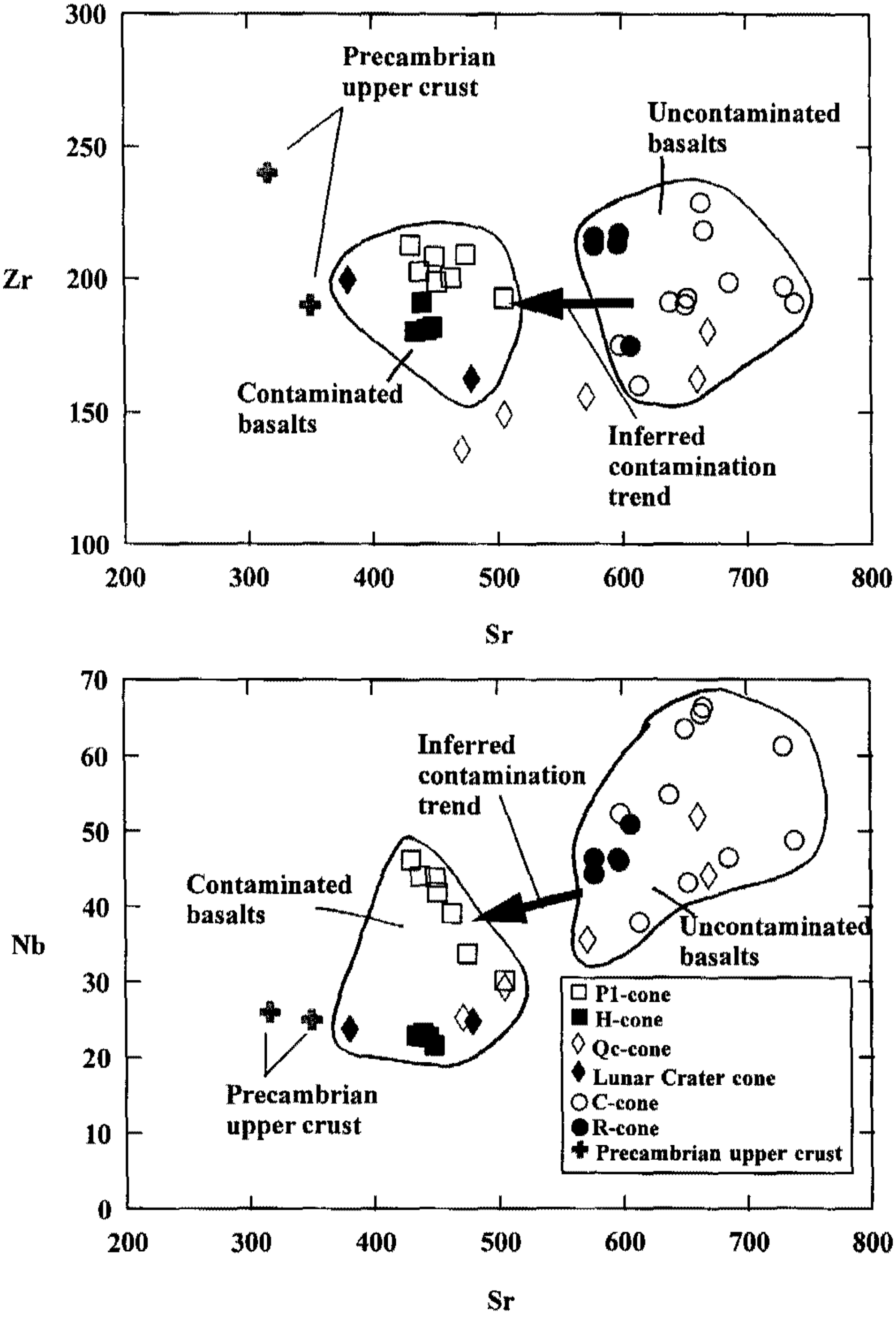

Figure 39. Precambrian upper crust has suitable Zr, Sr and Nb contents to be a contaminant for P1, H and Lunar Crater cone basalts. Precambrian upper crust chemistry is from Taylor and McLennan (1985).

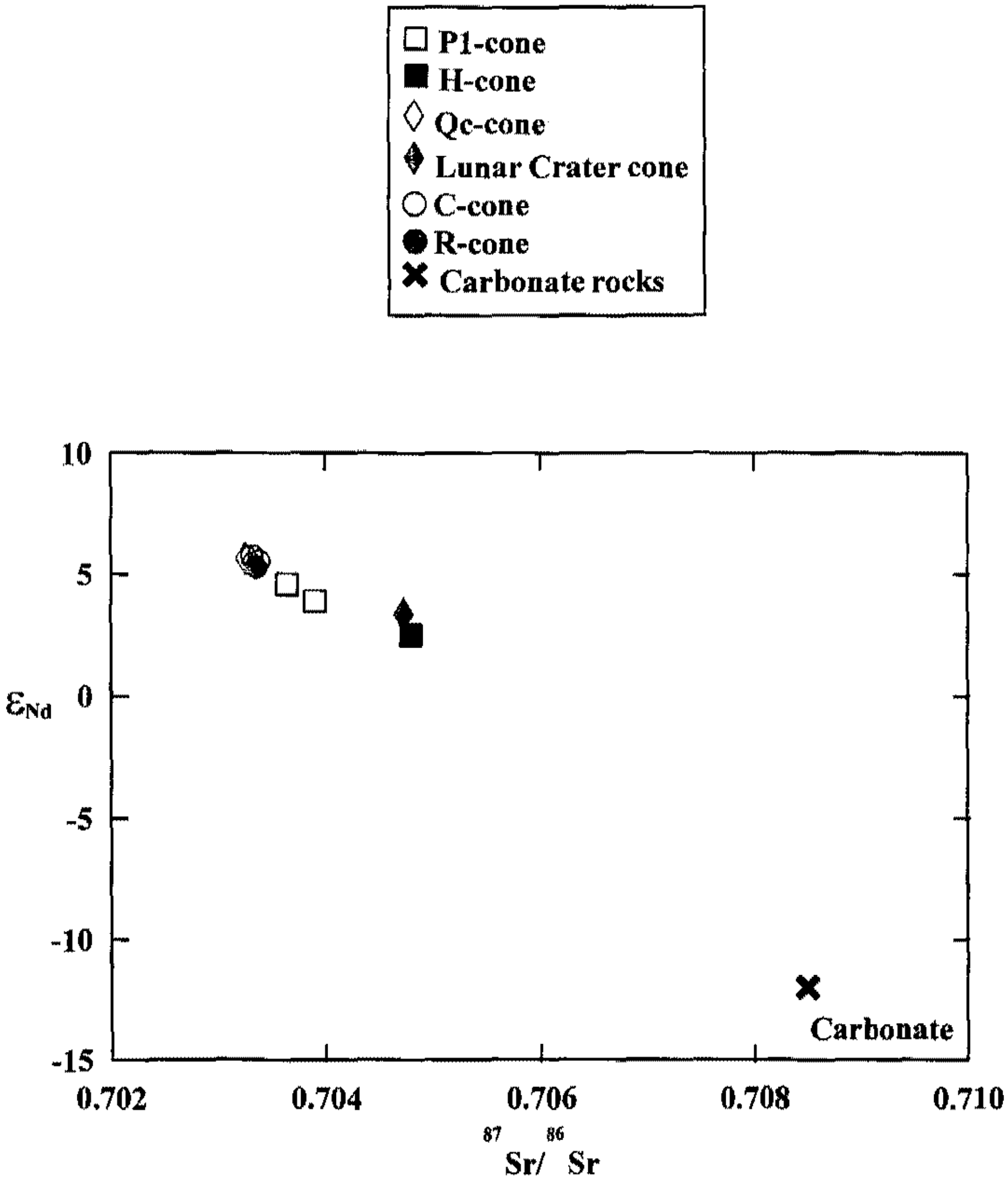

40

Figure[redacted]**.** Carbonate rocks have the proper Nd and Sr isotopic ratios to be a contaminant for P1, H and Lunar Crater cone basalts. Carbonate chemistry is from Yogodzinski et al. (1996).

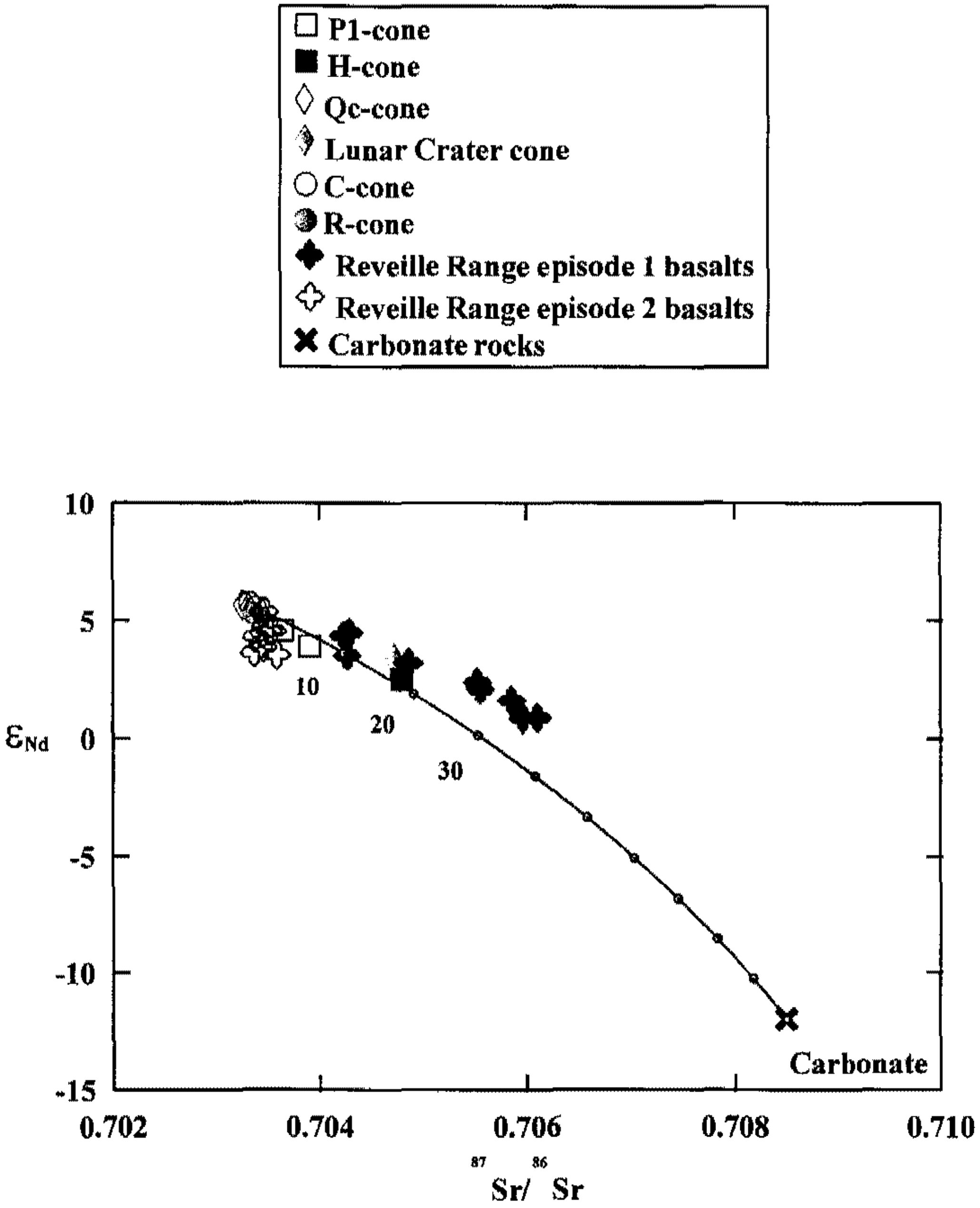

41

Figure [illegible]. Mixing of Reveille Range episode 1 basalts and Citadel Mountain alkali basalts with carbonate rocks. Model and carbonate composition after Yogodzinski et al. (1996).

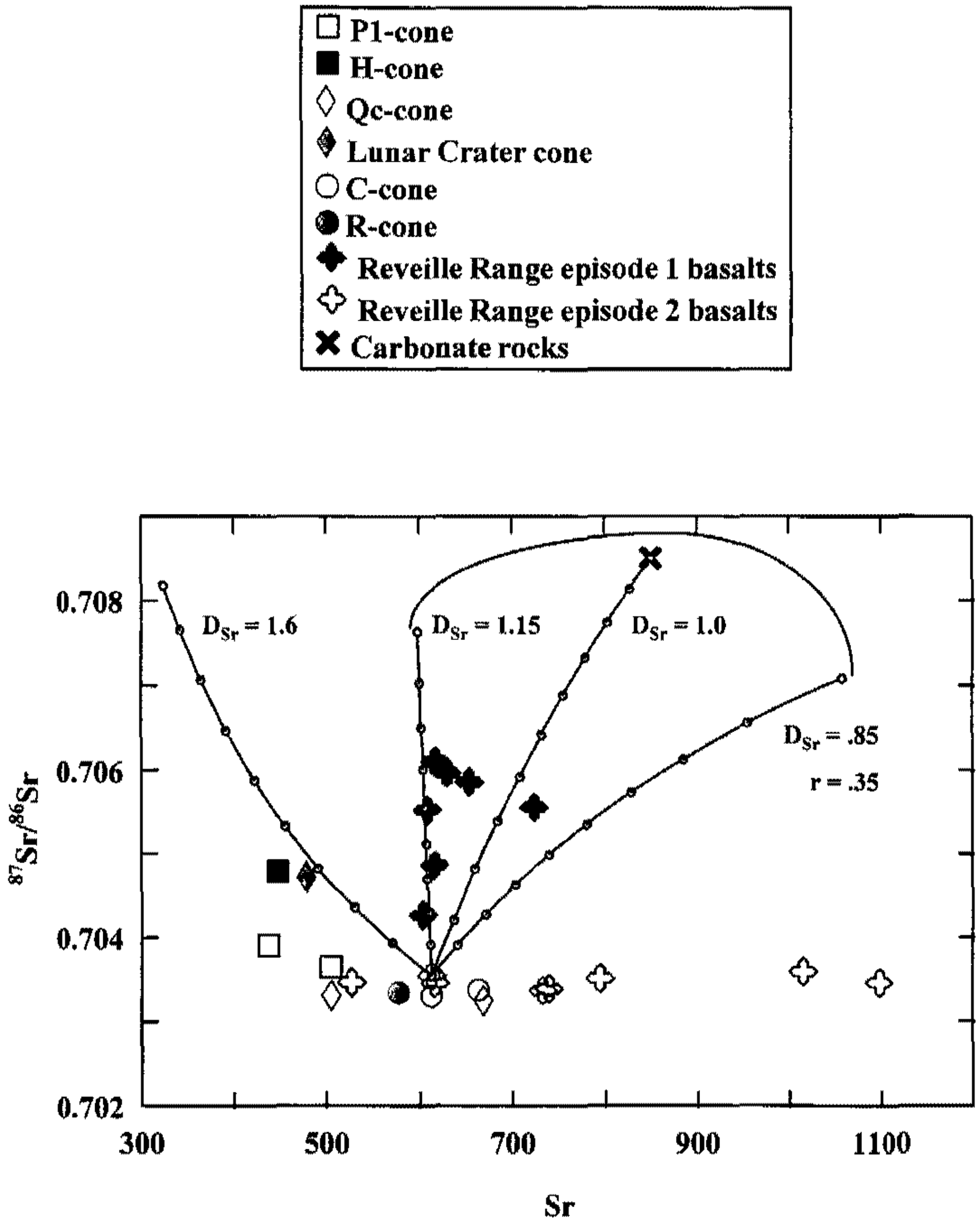

42

Figure [illegible]. Sr contents of Reveille Range episode 1 basalts increase with carbonate assimilation. Sr contents of alkali basalts on Citadel Mountain decrease from Qc, C and R-cone to P1, H and Lunar Crater cone samples and lie outside of the assimilation envelop (between $D_{Sr} = 1.15$ and $D_{Sr} = 0.85$) suggested by Yogodzinski et al. (1996).

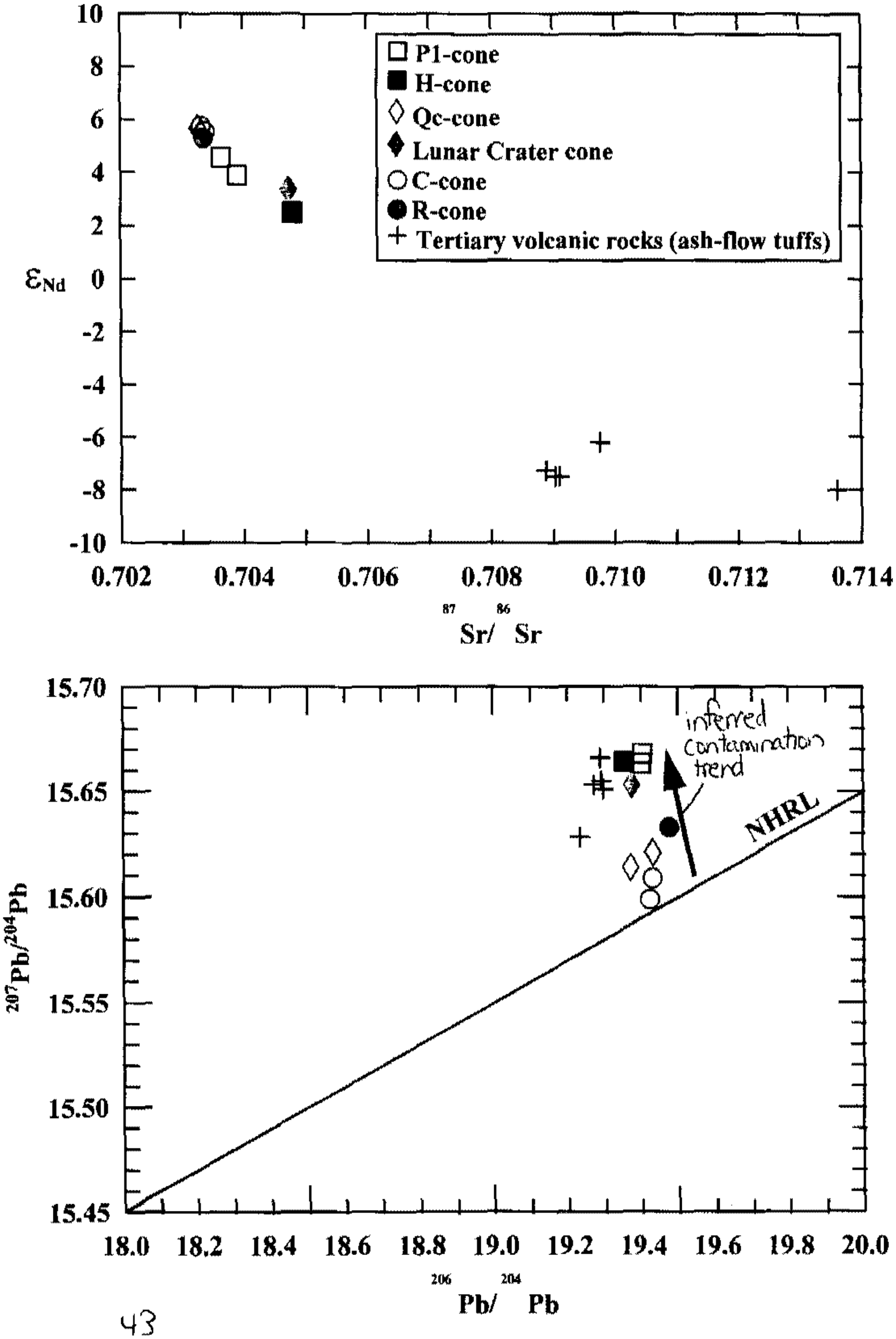

43

Figure . Nd and Sr isotopic ratios for Tertiary volcanic rocks (ash-flow tuffs) are suitable as contaminants for P1, H and Lunar Crater cone basalts, however, ^{206}Pb isotopic ratios are too low. Tertiary volcanic rock chemistry is from Rash (1995).

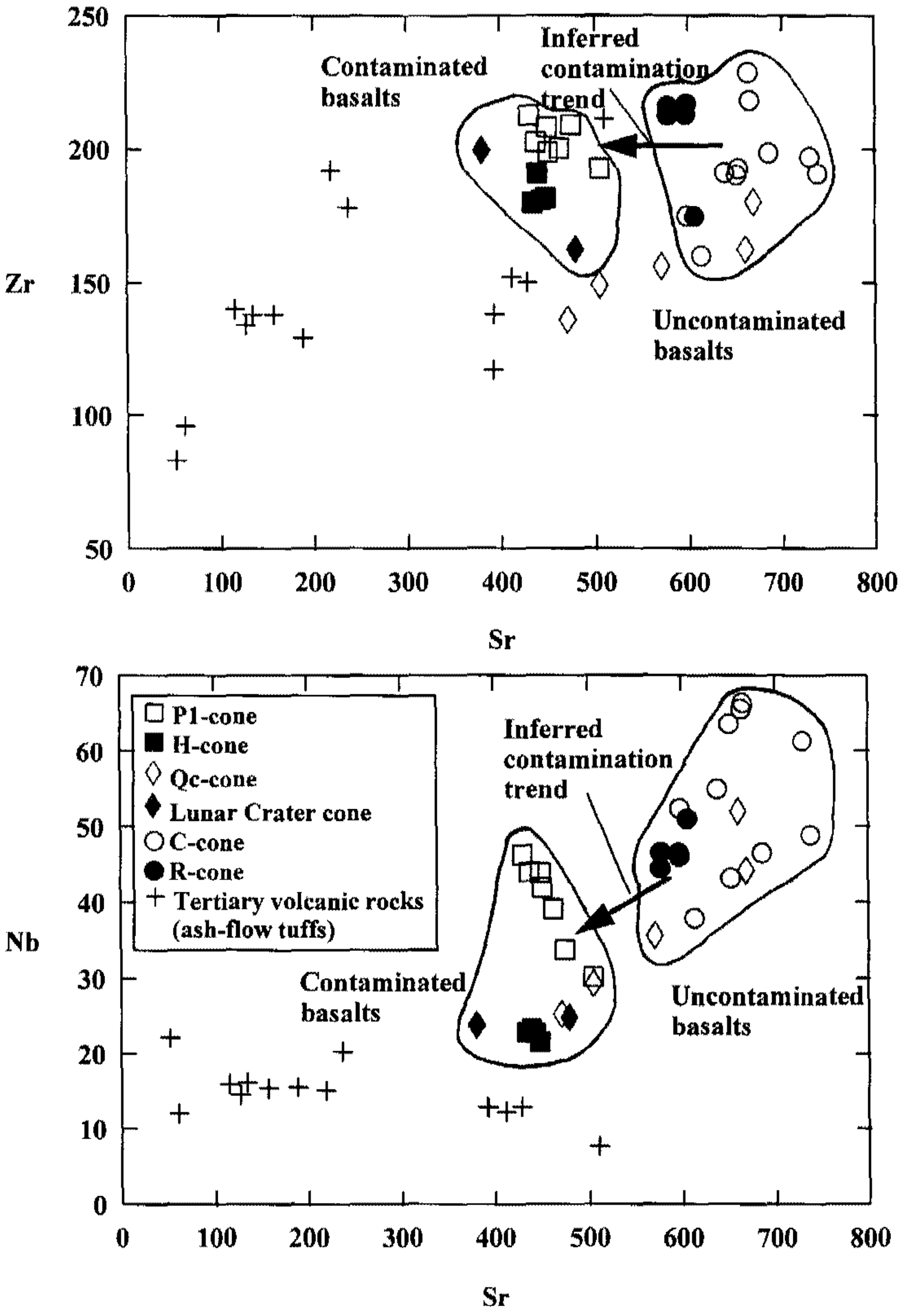

Figure 44. Tertiary volcanic rocks (ash-flow tuffs) are too low in trace elements Zr, Sr and Nb to be a suitable contaminant for the production of P1, H and Lunar Crater cone magmas. Chemistry for Tertiary volcanic rocks is from Rash (1995).

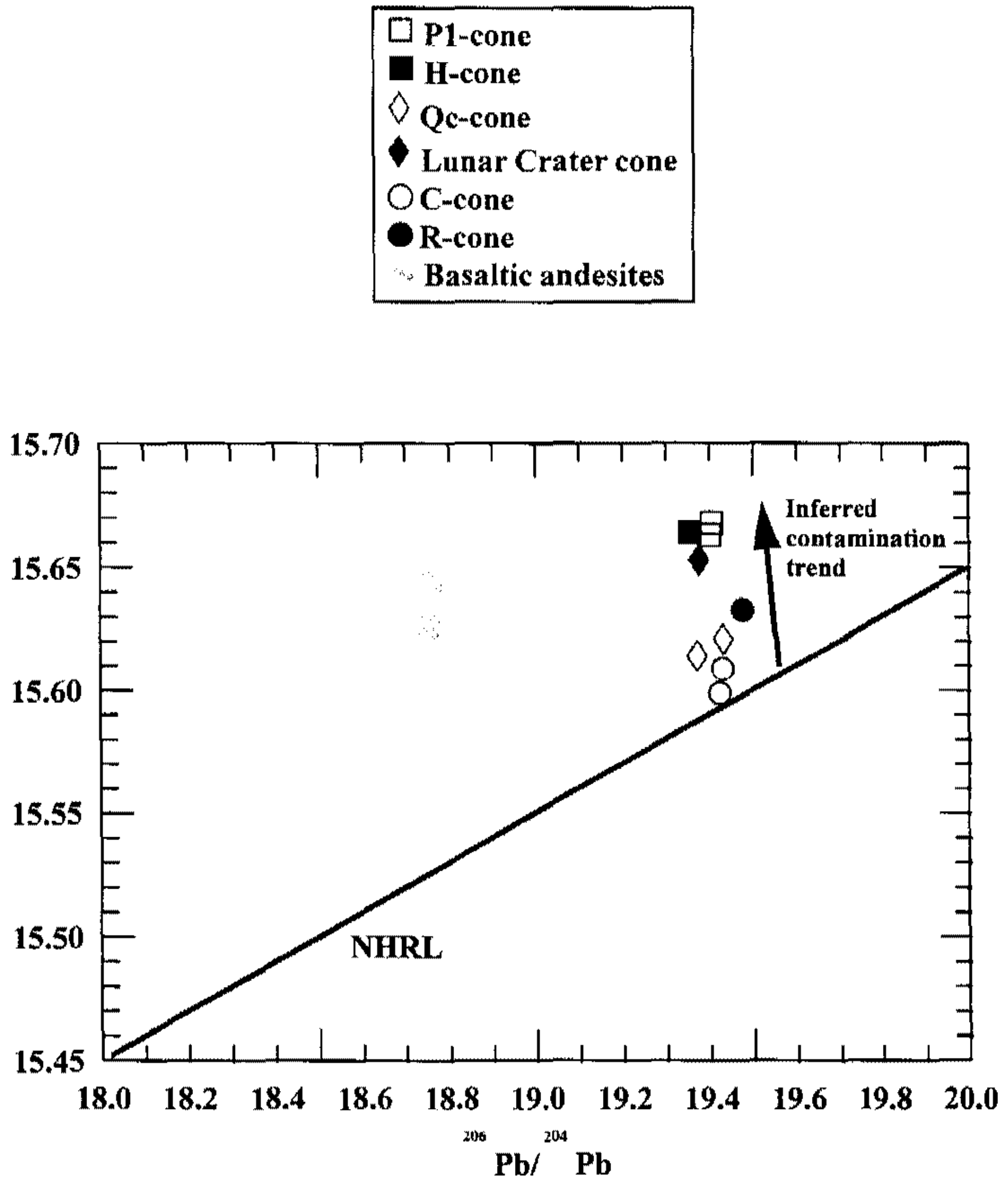

Figure 45. Pb isotopic ratios for basaltic andesites are too low to be a contaminant for P1, H and Lunar Crater cone basalts.

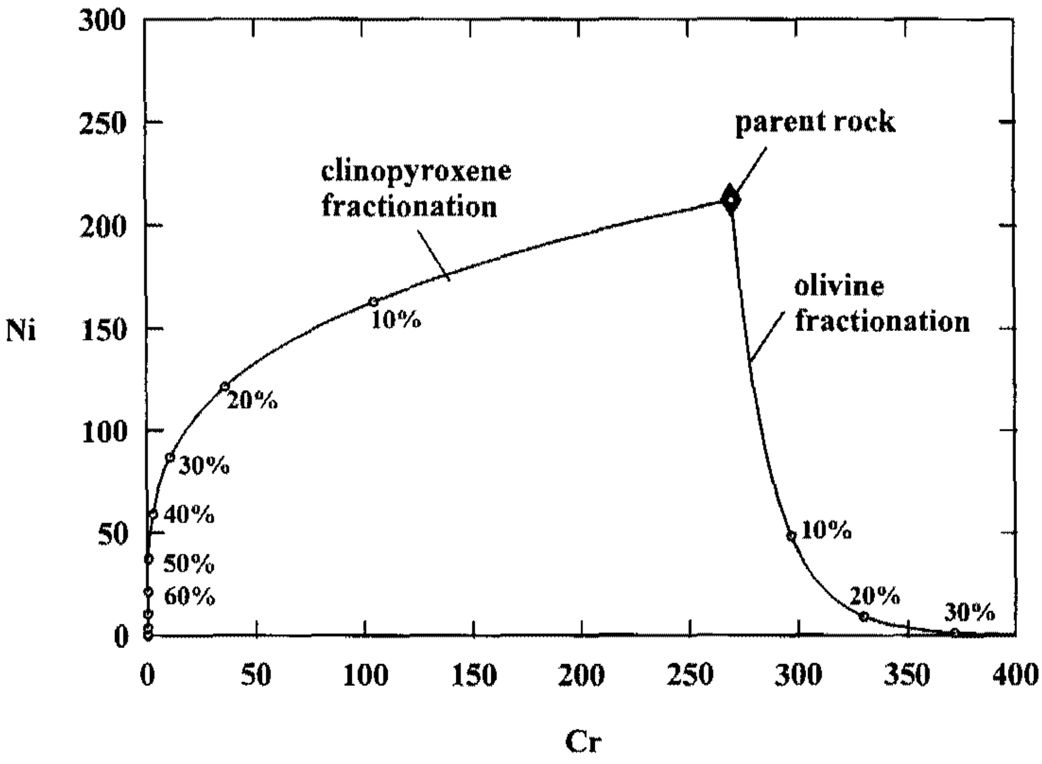

Figure 46. Diagram shows the behavior of Ni and Cr during fractional crystallization (FC). FC of olivine results in rapid decrease in Ni until about 20% olivine is fractionated and then to higher Cr for larger amounts of olivine fractionation. FC of clinopyroxene results in rapid decrease in Cr until 30% clinopyroxene is fractionated and then to lower Ni with additional FC.

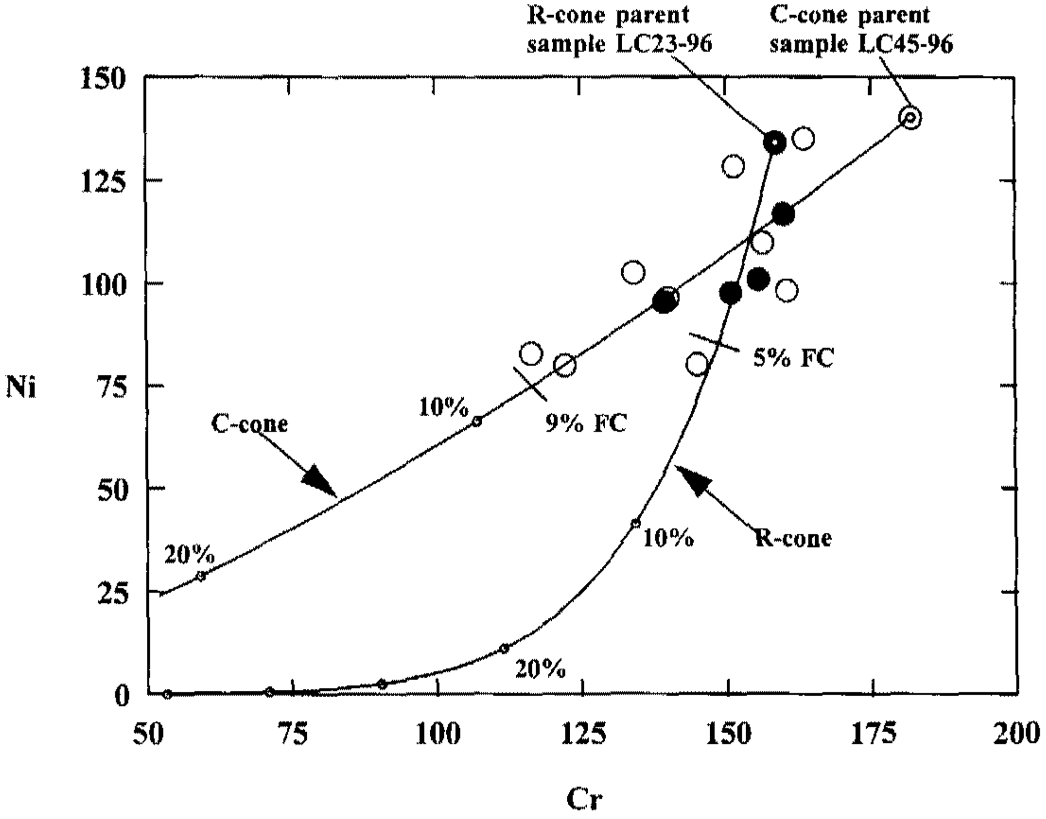

Figure 47. C-cone lavas can be explained by 9% FC of 60% clinopyroxene and 40% olivine. R-cone lavas can be explained by 5% FC of 25% clinopyroxene and 75% olivine. Note the similarity of composition for parental rocks for C and R-cones.

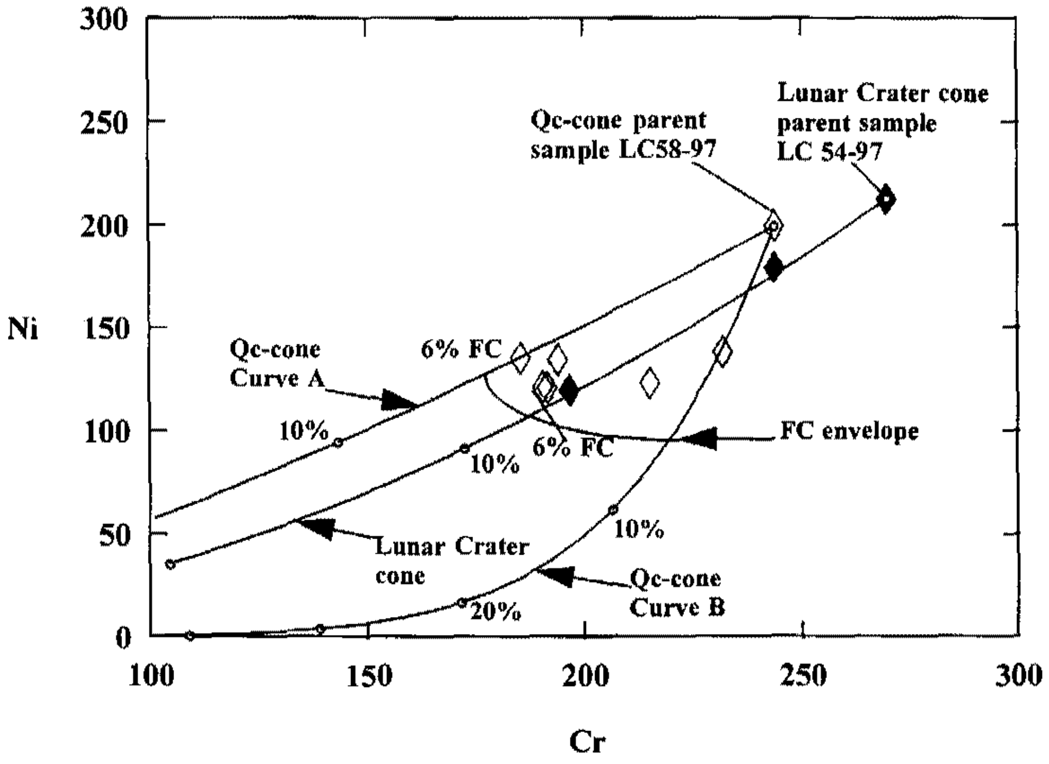

Figure 48. Boundaries for the FC model envelope developed for Qc-cone lavas can be formed by less than 6% FC of 60% clinopyroxene and 40% olivine (curve A) and 25% clinopyroxene and 75% olivine (curve B).

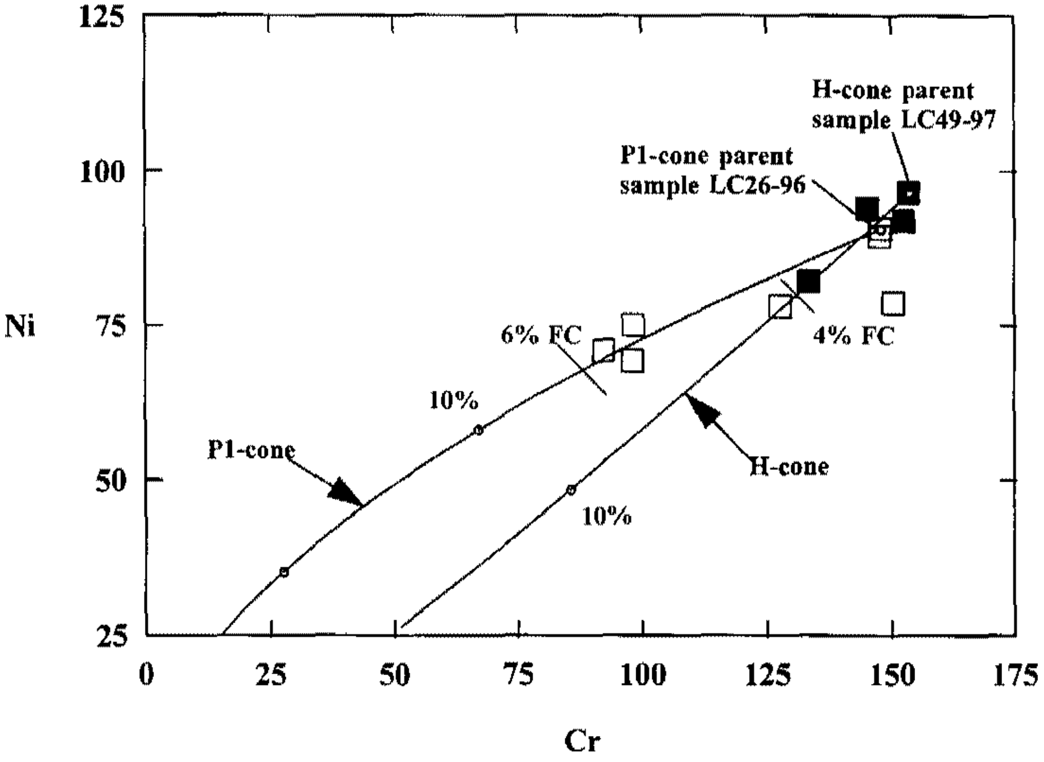

Figure 51. FC model shows that the P1-cone lavas requires 6% fractionation of 85% clinopyroxene and 15% olivine. FC model for H-cone lavas requires only 4% fractionation of 65% clinopyroxene and 35% olivine.

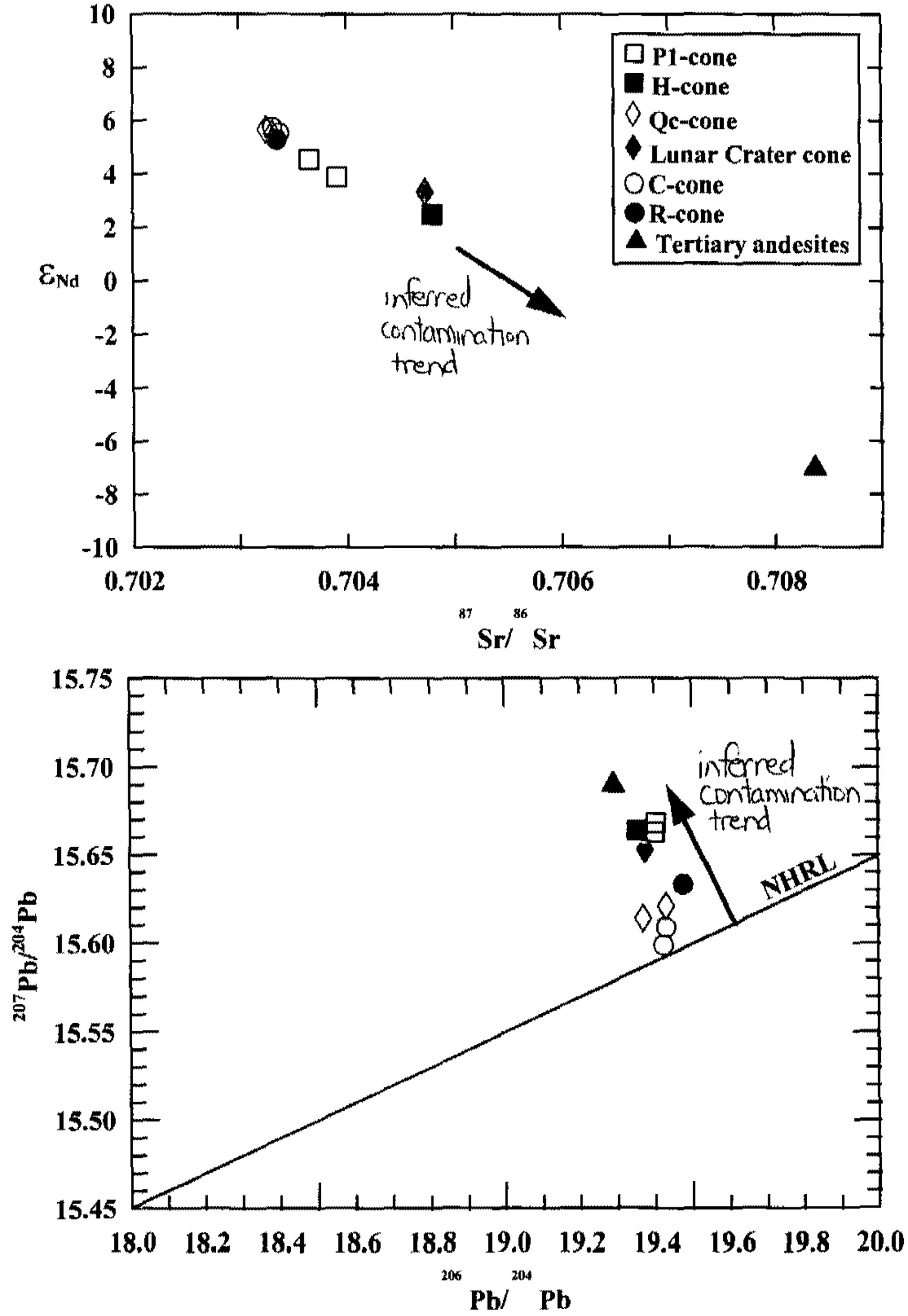

50

Figure [illegible]. Nd, Sr and Pb isotopic ratios of Citadel Mountain alkali basalts produce a data array and trends toward the isotopic compositions of the Tertiary andesites.

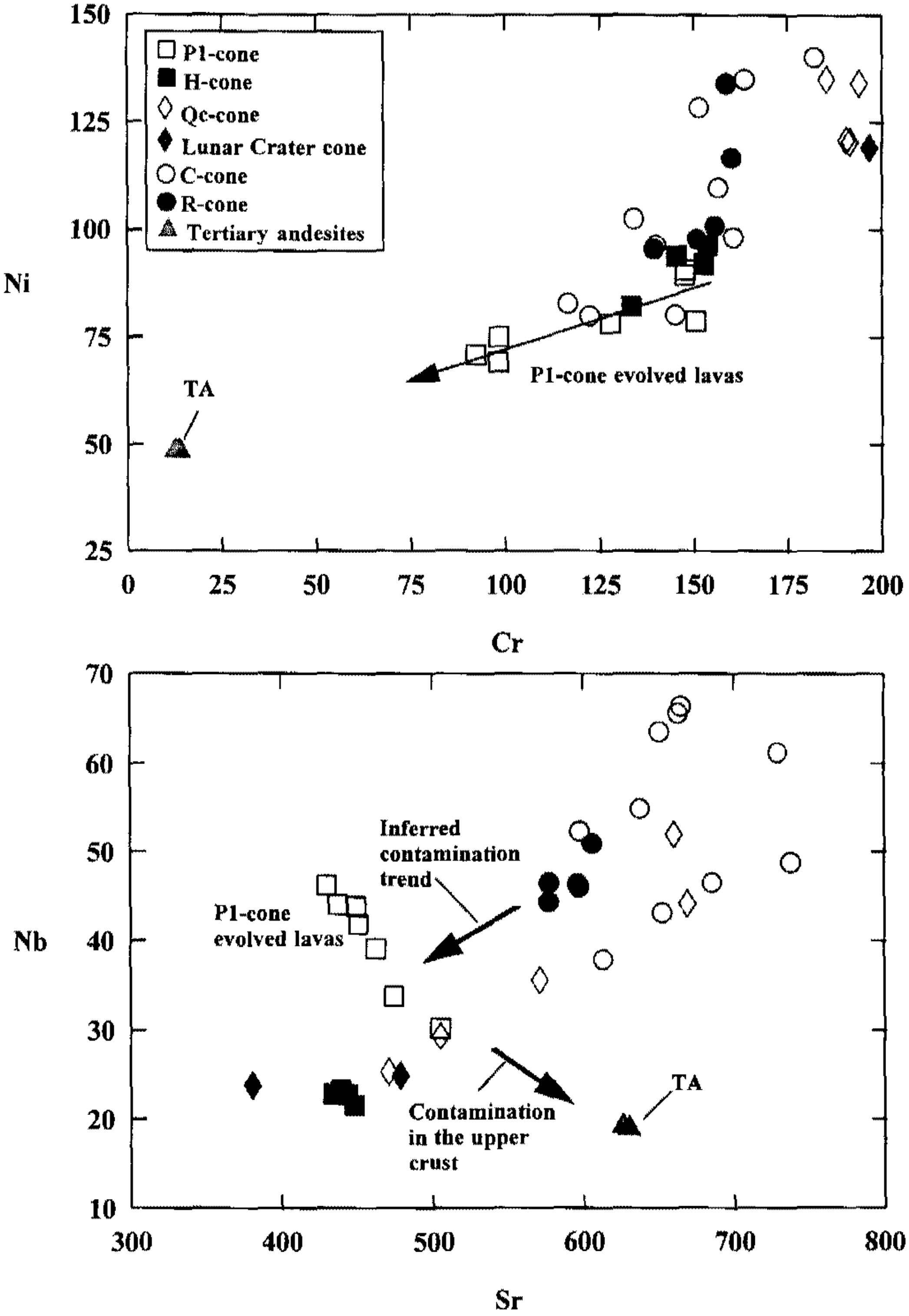

Figure 51. P1-cone lavas are lower in Nb and Sr than Qc, C and R-cone lavas. Tertiary andesite (TA) does not have the proper trace element signature to be a contaminant. P1-cone evolved lavas later evolved to lower Cr and Ni and higher Sr and lower Nb toward TA. The Tertiary andesites may serve as a contaminant during the FC of P1-cone lavas in the upper crust.

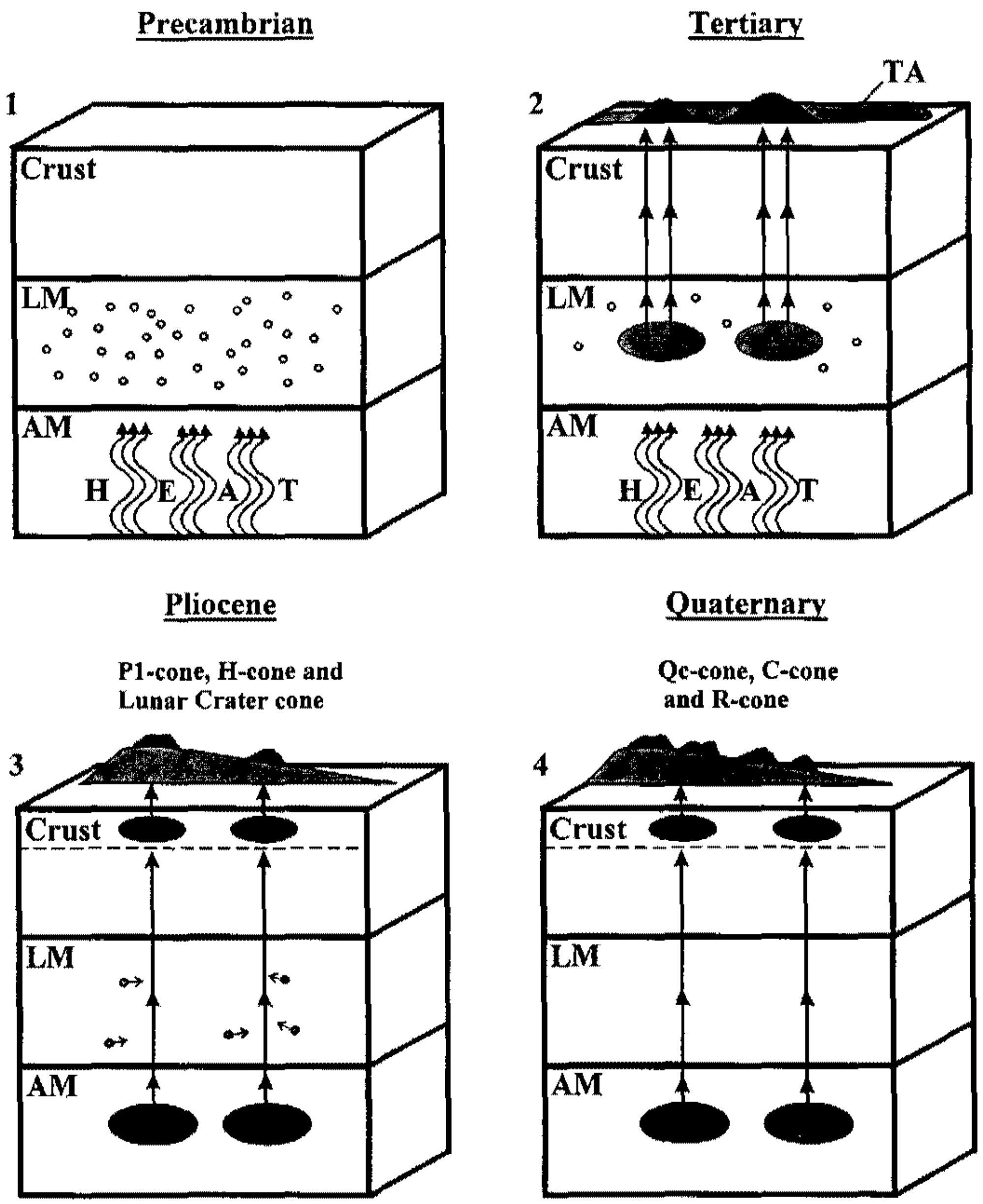

Figure 52. 1. Addition of lithospheric mantle veinlets to the mantle lithosphere (LM) during the Precambrian. **2.** Early calc-alkaline magmatism in the Miocene. Tertiary andesite lavas are produced by melting and fractional crystallization of lithospheric mantle veinlets. **3.** In the Pliocene, asthenospheric magmas rise and mix with the remaining lithospheric mantle veinlets. The resulting magma then rises to the upper crust where they fractionate and possibly assimilate small amounts of Tertiary andesite. **4.** During the Quaternary to Recent, asthenospheric magmas rise through the lithospheric mantle uncontaminated due to no remaining lithospheric mantle veinlets. Magmas fractionate in the upper crust (<10%) and erupt.

CHAPTER 7

MANTLE SOURCES

The transition from a lithospheric mantle to an asthenospheric mantle source for Late Cenozoic basalts has been documented in only a few areas in the Basin and Range (Livaccari and Perry, 1993) and the timing of mantle transitions are poorly constrained. For example, transition from a lithospheric mantle to an asthenospheric mantle source occurred in the Lake Mead area near Las Vegas between 12 and 5 Ma (Feuerbach et al., 1993) and in the Reveille Range between 14 and 6 Ma (Rash, 1995).

A mantle transition was thought to have occurred in the LCVF between 9 and 4 Ma (Foland et al., 1987; Livaccari and Perry, 1993, Rash, 1995). This was based on 9 Ma basalts located approximately 75 km south of the Lunar Crater maar having $\varepsilon_{Nd} = -4$ and $^{87}Sr/^{86}Sr$ of about 0.7080 (Foland and Bergman, 1992) that were interpreted as having a lithospheric mantle source (Livaccari and Perry, 1993). However, Livaccari and Perry's (1993) conclusion that a transition from a lithospheric mantle to an asthenospheric mantle source occurred in the LCVF between 9 and 4 Ma is probably not correct. Foland and Bergman (1992) concluded that the mantle source for LCVF basalts of all ages resembles OIB and may be entirely asthenospheric. Additionally, they concluded that the isotopic variations can be explained by addition of a crustal component similar to Miocene volcanic rocks with higher $^{87}Sr/^{86}Sr$ and lower ε_{Nd}. Although Foland and Bergman (1992) interpreted the 9 Ma sample as contaminated by crust, Livaccari and Perry (1993) used the 9 Ma basalts as evidence for a lithospheric mantle source for an alkali basalt in the LCVF and concluded that the mantle source transition occurred in the LCVF with basalts having $\varepsilon_{Nd} = -4$ at 9 Ma and +6 at 4 Ma.

Further evidence for crustal contamination of alkali basalts is observed in the Reveille Range. Yogodzinski et al. (1996) modeled Reveille Range basalts (hawaiites and basanites) by developing two mixing models. The first model mixed an OIB parent magma with a hypothetical lithospheric endmember (Sr=1400, Nd=97 ppm) and the second model mixed the same OIB parent magma with a carbonate endmember (Sr=850, Nd=10 ppm). Lithospheric mantle sources for alkali basalts in the Reveille Range were discounted. Mixing models showed Episode-1 hawaiites (5-6 Ma) (high $^{87}Sr/^{86}Sr$ and low ε_{Nd}) located in the southern Reveille Range are contaminated by carbonates in the upper crust. Episode-2 hawaiites and basanites (3-4.5 Ma) located in the northern Reveille Range have an asthenospheric mantle source and are not contaminated. The model of Yogodzinski et al. (1996) suggests that the 9 Ma isotopically enriched basalt ($\varepsilon_{Nd} = -4$ and $^{87}Sr/^{86}Sr = 0.7080$) described by Foland and Bergman (1992) and incorrectly interpreted by Livaccari and Perry (1993) is probably contaminated by upper crustal material and does not represent a lithospheric mantle source. Therefore, a mantle source transition is not supported by data from Foland and Bergman (1992).

The mantle source transition in the Reveille Range proposed to have occurred between 14 and 6 Ma (Rash, 1995) is based on the age of Miocene basaltic andesite located 30 km to the southeast of the Reveille Range near Rachel, Nevada. Rash (1995) found that basaltic andesites in the northern tip of the Reveille Range have a lithospheric mantle source and concluded these rocks are of comparable age to the basaltic andesites 30 km to the southeast based on similar rock chemistry. The transition did occur but the date of the basaltic andesites in the northern Reveille Range is suspect because there is no stratigraphic evidence the basaltic andesite units in the northern Reveille Range and southeast of the Reveille Range are the same age.

Geochemical and age data presented in this study indicates a transition in mantle source occurred in the LCVF, however, in a different time interval than suggested by Livaccari and Perry (1993). Alkali basalts on Citadel Mountain are isotopically depleted ($^{87}Sr/^{86}Sr = 0.7033$ to 0.7048 and $\varepsilon_{Nd} = +2.5$ to +5.8) and were produced by partial melting of an OIB-type asthenospheric mantle source. Basaltic andesites (21.79 Ma) located 11 km east of Citadel Mountain are isotopically enriched ($^{87}Sr/^{86}Sr =$ 0.7076 to 0.7077 and $\varepsilon_{Nd} = -7.3$ to -7.6) and show Nb troughs on OIB normalized spider diagrams indicating they were produced by partial melting of the lithospheric mantle. Therefore, I conclude that the transition from lithospheric mantle to asthenospheric mantle source occurred between 21.79 Ma and 3.82 Ma, the age of the oldest alkali basalt (P1-cone flow) on Citadel Mountain.

The data presented in this study is the best age constraint for a mantle source transition because the basaltic andesites are located within a reasonable distance (11 km) of the alkali basalts on Citadel Mountain. Although this estimate for the transition covers a large range of time, it is the best estimate available to date. Since the 21.79 Ma basaltic andesites are the youngest Miocene unit exposed in the area, this time constraint for a mantle source transition is probably the best that can be done.

CHAPTER 8

IMPLICATIONS

Alkali Basalts Used as Mantle Probes

Alkali basalts are often considered mantle probes because their rapid transit through the crust precludes significant contamination or fractional crystallization (Wilson, 1989). According to this interpretation, alkali basalts have isotopic and trace element signatures that directly reflect their mantle source. Several workers have taken precautions when using alkali basalts as mantle probes. For example, Farmer et al. (1989) only used basalts with SiO_2 content of less than 50% in their regional study of mantle heterogeneity in the western U.S. Leeman and Rogers (1970) and Foland and Bergman (1992) suggested that only alkali basalts containing ultramafic nodules should be used as mantle probes. Other authors (Best and Brimhall, 1974) only used samples with a Mg# greater than 60 to characterize the mantle. A Mg# of about 71 indicates that the alkali basalt is in equilibrium with its mantle source and that it probably was unmodified during its ascent from the mantle to the surface.

My work suggests that these precautions are necessary. Based on the results of this thesis, it is clear that although small volume mafic volcanic systems have relatively simple evolutionary histories, alkali basalt can be modified by magma commingling/mixing and by fractional crystallization. Contamination events will alter isotopic ratios and trace element characteristics and fractional crystallization will change trace and major element signatures. This thesis also demonstrates that there can be significant chemical differences between alkali basalts that erupted from cinder cones less than 1 km apart. Based on this information, random sampling of a few alkali basalts from a small volume mafic volcanic field with the purpose of describing the field or as part of a regional study of mantle heterogeneity is dangerous. Instead, understanding of the petrogenetic history, stratigraphy and the scale of chemical variability within the field is important before samples can provide meaningful results. My work in the LCVF suggests that only the youngest samples in the field can be used to obtain information about the mantle. However, even in these samples, fractional crystallization has modified trace and major element contents. In short, alkali basalt can be used to gather information about the mantle but only if proper care is taken.

Future Eruptions

Future volcanism in the LCVF will likely occur in the northern Pancake Range in the vicinity of the Marcath flow. Because ages of cinder cones on Citadel Mountain are not related to geographic position, a future volcanic eruption may occur to the north or south of U.S. Highway 6. The Quaternary and Recent lava flows range from 1 to 3 km long and flow radially or in a single direction from their source; therefore it is possible that U.S. Highway 6, a major transportation route through the Pancake Range, may be disrupted in the event of a future eruption. Recurrence rates calculated by Crowe et al.

(1992) suggest that values for the LCVF fall between 4×10^{-5} events yr^{-1} (vent count) and 1×10^{-5} events yr^{-1} (cluster count) or the equivalent of the formation of a new volcanic center or cluster of centers every 22,000 to 100,000 years. The last eruption in the Pancake Range (LCVF) occurred at 38 ka, therefore based on Crowe's probability estimate another eruption may occur within the next 60,000 years.

CHAPTER 9

SUMMARY AND CONCLUSIONS

Volcanic stratigraphy, $^{40}Ar/^{39}Ar$ dates and geochemistry suggest that alkali basalts on Citadel Mountain represent a simple magmatic system. The alkali basalts have an isotopically similar asthenospheric mantle source that produced similar parental magmas by multiple partial melting events. Although the alkali basalts were derived from the asthenospheric mantle, there may have been several individual magma bodies, each having evolved by different petrogenetic processes. The alkali basalts can be divided into older isotopically enriched lavas (P1, H and Lunar Crater cone) and younger isotopically depleted lavas (Qc, C and R-cone). Two contamination events may have affected the older basalt group; one event occurring in the lithosphere by magma commingling/mixing of rising asthenospheric melts with lithospheric mantle veinlets and another possible event occurring near the surface during fractional crystallization. The preferred model to explain the isotopic differences between the two groups (old and young cones and flows) calls upon magma commingling/mixing of rising asthenospheric melts with lithospheric mantle veinlets trapped within the mantle lithosphere to produce the P1, H and Lunar Crater parent magmas. Further chemical variation of the more evolved P1-cone lavas may have resulted from assimilating very small amounts of the Tertiary andesite near the surface during fractional crystallization of olivine and clinopyroxene. The younger isotopically depleted lavas evolved by fractional crystallization of olivine and clinopyroxene and have isotopic ratios that may reflect their asthenospheric mantle source.

A transition from a lithospheric mantle source to an asthenospheric mantle source occurred in the LCVF between 21.79 Ma (age of basaltic andesites) and 3.82 Ma (age of the P1-cone). The transition is postextensional because basaltic andesites east of Citadel Mountain are faulted and tilted while the earliest basaltic P1-cone flow is not faulted. Although the time constraint for a mantle transition in the LCVF reflects a large range of time, finding a better time constraint may not be possible.

REFERENCES

Albarede, F., 1995, Introduction to geochemical modeling: Cambridge University Press, Cambridge, England, 543 p.

Bergman, S. C., Foland, K. A. and Spera, F. J., 1981, On the origin of an amphibole-rich vein in a peridotite inclusion from the Lunar Crater Volcanic Field, Nevada, U.S.A.: Earth and Planetary Science Letters, v. 56, p. 343-361.

Bergman, S. C., 1982, Petrogenetic aspects of the alkali basaltic lavas and included megacrysts and nodules from the Lunar Crater Volcanic Field, Nevada, U.S.A. [Ph.D. thesis]: Ohio State University, Columbus, Ohio, 374 p.

Best, M. J. and Brimhall, W. H., 1974, Late Cenozoic alkali basaltic magmas in the western Colorado Plateau and the Basin and Range transition zone, USA and their bearing on mantle dynamics: Geological Society of America Bulletin, v. 85, p. 1677-1690.

Best, M. G., Christiansen, E. H., Deino, A. L., Gromme, C. S., McKee, E. H. and Noble, D. C., 1989, Eocene through Miocene volcanism in the Great Basin of the western United States: New Mexico Bureau of Mines and Mineral Resources Memoir 47, p. 91-133.

Blaylock, J., Smith, E. I. and Holm, R., 1996, Geochemical investigation of Sunset Crater, Arizona: Complex petrogenetic history of a low-volume magmatic system, (abs.): Geological Society of America, Abstracts with Programs, v. 28(7), p. 162.

Bradshaw, T. K. and Smith, E. I., 1994, Polygenetic Quaternary volcanism at Crater Flat, Nevada: Journal of Volcanology and Geothermal Research, v.63, p. 165-182.

Carr, M. J., 1994, IGPETWIN: Igpet for Windows petrology software: Somerset, Terra Softa, Inc.

Crowe, B. M., Picard, R., Valentine, G. and Perry, F. V., 1992, Recurrence models of volcanic events: applications to volcanic risk assessment: Proceedings of the International Nuclear Waste Symposium, v. 2, American Nuclear Society and American Society of Civil Engineers, p. 2344-2355.

Crowe, B., Perry, F., Geissman, J., McFadden, L., Wells, S., Murrell, M., Poths, J., Valentine, G. A., Bowker, L. and Finnegan, K., 1995, Status of volcanism studies for the Yucca Mountain site characterization project: Los Alamos National Laboratory.

Daley, E. E. and DePaolo, D. J, 1992, Isotopic evidence for lithospheric thinning during extension: southeastern Great Basin: Geology, v. 20, p. 104-108.

Dohrenwend, J. C., Abrahams, A. D. and Turrin, B. D., 1987, Drainage development on basaltic lava flows, Cima volcanic field, southeast California, and Lunar Crater volcanic field, south-central Nevada: Geological Society of America Bulletin, v. 99, p. 405-413.

Ekren, E. B., Snyder, R. P. and Dixon, G. L., 1972, Geologic map of the Lunar Crater quadrangle, Nye County, Nevada: U.S. Geological Survey Misc. Geol. Inv. Map I-700, scale 1:48,000.

Ekren, E. B., Quinlivan, W. D., Snyder, R. P. and Kleinhampl, F. J., 1974, Stratigraphy, structure, and geologic history of the Lunar Lake Caldera of Northern Nye County, Nevada: Journal of Research, U. S. Geological Survey, v. 2, no. 5, p. 599-608.

Farmer, G. L., Perry, F. V., Semken, S., Crowe, B., Curtis, D. and DePaolo, D. J., 1989, Isotopic evidence on the structure of origin of subcontinental lithospheric mantle in southern Nevada: Journal of Geophysical Research, v. 94, no. B6, p. 7885-7898.

Feuerbach, D. L., Smith, E. I., Walker, J. D. and Tangeman, J. A., 1993, The role of the mantle during crustal extension: constraints from geochemistry of volcanic rocks in the Lake Mead area, Nevada and Arizona: Geological Society of America Bulletin, v. 105, p. 1561-1575.

Fitton, J. G., James, D. and Leeman, W. P., 1991, Basic magmatism associated with Late Cenozoic extension in the western United States: Compositional variations in space and time: Journal of Geophysical Research, v. 96, n. B8, p. 13,693-13,711.

Foland, K. A., Kargel, J. S., Lum, C. L. and Bergman, S. C., 1987, Time-spatial-compositional relationships among alkali basalts in the vicinity of Lunar Crater, south central Nevada, Geological Society of America Abstracts with Programs, v. 19, p. 666.

Foland, K. A., Schucker, D. E., Smith, B. M., Todt, W. and Bergman, S. C.,1991, Isotope geochemistry of Cenozoic alkali basalts in the vicinity of the Lunar Crater Volcanic Field, south central Nevada: O and Pb evidence for crustal components; Geological Society of America Abstracts with Programs, v. 23, n. 5, p. A45.

Foland, K. A. and Bergman, S. C., 1992, Temporal and spatial distribution of basaltic volcanism in the Pancake and Reveille Ranges north of Yucca Mountain: in Proceedings of the International Nuclear Waste Symposium, v. 2, American Nuclear Society and American Society of Civil Engineers, p. 2366-2371.

Harry, D. L. and Leeman, W. P., 1995, Partial melting of melt metasomatized subcontinental mantle and the magma source potential of the lower lithosphere: Journal of Geophysical Research, v. 100, n. B7, p. 10,255-10,269.

Kargel, J. S., 1987, The geochemistry of basalts and mantle inclusions from the Lunar Crater Volcanic Field, Nevada; petrogenetic and geodynamic implications [Master's Thesis]: Ohio State University, Columbus, Ohio, 369p.

LeBas, M.. J., LeMaitre, R. W., Streckeisen, A. and Zanettin, B., 1986, A chemical classification of volcanic rocks based on the total alkali silica diagram: Journal of Petrology, v. 27, p. 745-750.

Leeman, W. P. and Rogers, J. J. W., 1970, Late Cenozoic alkali-olivine basalts of the Basin-Range Province, USA: Contributions to Mineralogy and Petrology, v. 25, p. 1-24.

Livaccari, R. F. and Perry, F. V., 1993, Isotopic evidence for preservation of Cordilleran lithospheric mantle during the Sevier-Laramide orogeny, western United States: Geology, v. 21, p. 719-722.

Lum, C. C. L., 1986, Aspects of the petrogenesis of alkali basalts from the Lunar Crater Volcanic Field, Nevada [Master's Thesis]: Ohio State University, Columbus, Ohio, 140p.

Lum, C. C. L, Leeman, W. P., Foland, K. A., Kargel, J. A. and Fitton, J. G., 1989, Isotopic variations in continental basaltic lavas as indicators of mantle heterogeneity: examples from the western U.S. Cordillera: Journal of Geophysical Research, v. 94, no. B6, p.7871-7884.

Neuman, H., Mead, J. and Vitaliano, C. J., 1954, Trace-element variation during fractional crystallization as calculated from the distribution law: Geochimica et Cosmochimica Acta, v. 6, p. 90-100.

Perry, F. V., Baldridge, W. S. and DePaolo, D. J., 1987, Role of asthenosphere and lithosphere in the genesis of late Cenozoic basaltic rocks from the Rio Grande Rift and adjacent regions of the southwestern United States: Journal of Geophysical Research, v. 92, no. B9, p. 9193-9213.

Rash, K. B., 1995, Geology and geochemistry of Tertiary volcanic rocks in the Northern Reveille and Southern Pancake Ranges, Nye County, Nevada [Master's Thesis]: University of Nevada, Las Vegas, Nevada, 171p.

Scott, D. H. and Trask, N. J., 1971, Geology of the Lunar Crater Volcanic Field, Nye County, Nevada: U. S. Geological Survey Professional Paper 599-I, p. 1-22.

Shepard, M. K., Arvidson, R. E., Caffee, M., Finkel, R. and Harris, L., 1995, Cosmogenic exposure ages of basalt flows: Lunar Crater volcanic field, Nevada: Geology, v. 23, no. 1, p. 21-24.

Simkin, T., Siebert, L., McClelland, L., Bridge, D., Newhall, C. and Latter, J. H., 1981, Smithsonian Institution, Volcanoes of the world, A regional directory, gazetteer, and chronology of volcanism during the last 10,000 years: Hutchinson Ross Publishing Company, Stroudsburg, Pennsylvania, 232 p.

Sinton, J., Rowland, S. and Bergmanis, E., 1997, Maui field trip guide: Geological Society of America 93rd Cordillera Section Meeting, 24 p.

Taylor, S. R. and McLennan, S. M., 1985, The continental crust: its composition and evolution: London, Blackwell Scientific Publications, 312 p.

Trask, N. J., 1969, Ultramafic xenoliths in basalt, Nye County, Nevada; U. S. Geological Survey Professional Paper, no. 650-D, p. 43-48.

Vaniman, D. T., Crowe, B. M. and Gladney, E. S., Petrology and geochemistry of Hawaiite lavas from Crater Flat, Nevada: Contributions to Mineralogy and Petrology, v. 80, p. 341-357.

Vitaliano, C. J. and Harvey, R. D., 1965, Alkali basalts from Nye County, Nevada: American Mineralogist, v. 50, no. 1-2, p. 73-84.

Wilson, M., 1989, Igneous Petrogenesis: London, Unwin Hyman, 466 p.

Yogodzinski, G. M., Naumann, T. R., Smith, E. I., Bradshaw, T. K. and Walker, J. D., 1996, Evolution of a mafic volcanic field in the central Great Basin, south central Nevada: Journal of Geophysical Research, v. 101, no. B8, p. 17,425-17,445.

APPENDIX A: GEOCHEMICAL DATA

Major and Trace Element Abundances

Major elements	**P1-cone Basalt**						
in wt. %	**LC16-96**	**LC19-96**	**LC21-96**	**LC24-96**	**LC26-96**	**LC40-96**	**LC44-96**
SiO_2	48.51	47.73	47.54	48.22	48.34	49.24	48.33
Al_2O_3	15.77	15.56	15.24	15.07	15.35	15.38	14.62
TiO_2	2.59	2.62	2.68	2.66	2.65	2.72	2.82
Fe_2O_3	13.34	12.85	13.03	13.18	13.34	13.29	13.48
MgO	5.59	5.48	5.40	5.86	5.47	5.76	5.70
CaO	8.56	8.41	8.59	8.54	8.58	8.44	8.60
Na_2O	3.42	3.58	3.58	3.51	3.35	3.70	3.35
K_2O	1.15	1.16	1.25	1.25	1.24	1.36	1.27
MnO	0.17	0.16	0.16	0.17	0.16	0.16	0.17
P_2O_5	0.53	0.51	0.54	0.54	0.51	0.51	0.61
Total^{*1}	99.61	98.04	98.02	98.99	98.97	100.56	98.96
Mg#	45.4	45.8	45.1	46.8	44.8	46.2	45.6

Trace elements							
in ppm	**LC16-96**	**LC19-96**	**LC21-96**	**LC24-96**	**LC26-96**	**LC40-96**	**LC44-97**
Zr (XRF)^{*2}	192.6	200.3	208.1	202.6	198.8	212.6	209.1
La (ICP-MS)^{*3}	25.15						
Ce (ICP-MS)	50.27						
Pr (ICP-MS)	6.12						
Nd (ICP-MS)	27.40						
Sm (ICP-MS)	7.08						
Eu (ICP-MS)	2.39						
Gd (ICP-MS)	7.18						
Tb (ICP-MS)	1.14						
Dy (ICP-MS)	6.77						
Ho (ICP-MS)	1.28						
Er (ICP-MS)	3.28						
Tm (ICP-MS)	0.43						
Yb (ICP-MS)	2.62						
Lu (ICP-MS)	0.40						
Ba (XRF, ICP-MS)	307.0						
Th (ICP-MS)	2.29						
Nb (XRF)	30.14	39.05	43.80	43.96	41.81	46.18	33.74
Y (XRF)	34.34	44.58	48.74	44.21	45.49	48.61	48.38
Hf (ICP-MS)	5.11						
Ta (ICP-MS)	2.31						
U (ICP-MS)	0.75						
Pb (ICP-MS)	1.45						
Rb (XRF)	23.30	15.20	18.08	19.35	17.54	35.48	26.87
Cs (ICP-MS)	0.14						
Sr (XRF)	505.0	462.8	449.7	437.7	451.0	430.4	474.6
Sc (ICP-MS)	23.58						
Cr (XRF)	98.37	92.35	98.16	127.8	147.9	147.7	150.5
Ni (XRF)	75.00	70.86	69.20	78.07	90.66	89.43	78.67

APPENDIX A: GEOCHEMICAL DATA

Major and Trace Element Abundances (continued)

Major elements	**H-cone Basalt**			
in wt. %	**LC38-96**	**LC47-97**	**LC48-97**	**LC49-97**
SiO_2	50.64	50.09	50.36	51.51
Al_2O_3	15.35	15.41	15.28	15.74
TiO_2	2.28	2.25	2.33	2.33
Fe_2O_3	12.36	12.21	12.52	12.46
MgO	6.26	9.34	9.12	8.43
CaO	8.50	1.07	1.06	1.17
Na_2O	3.41	0.16	0.17	0.16
K_2O	1.06	0.45	0.40	0.40
MnO	0.16	3.13	3.15	3.20
P_2O_5	0.42	5.65	5.95	5.52
Total	100.43	99.76	100.33	100.93
Mg#	50.1	47.8	48.5	46.7

Trace elements in ppm	**LC38-96**	**LC47-97**	**LC48-97**	**LC49-97**
Zr (XRF)	181.7	180.9	180	191
La (ICP-MS)	22.19			
Ce (ICP-MS)	43.67			
Pr (ICP-MS)	5.35			
Nd (ICP-MS)	23.82			
Sm (ICP-MS)	6.41			
Eu (ICP-MS)	2.09			
Gd (ICP-MS)	6.45			
Tb (ICP-MS)	1.05			
Dy (ICP-MS)	6.14			
Ho (ICP-MS)	1.20			
Er (ICP-MS)	3.03			
Tm (ICP-MS)	0.41			
Yb (ICP-MS)	2.41			
Lu (ICP-MS)	0.37			
Ba (XRF, ICP-MS)	359			
Th (ICP-MS)	1.89			
Nb (XRF)	21.52	22.69	22.80	23.20
Y (XRF)	31.62	41.32	41.90	46.20
Hf (ICP-MS)	4.74			
Ta (ICP-MS)	1.92			
U (ICP-MS)	0.58			
Pb (ICP-MS)	2.11			
Rb (XRF)	17.30	18.23	16.1	18.30
Cs (ICP-MS)	0.15			
Sr (XRF)	448	443.4	434	439
Sc (ICP-MS)	22.84			
Cr (XRF)	133.5	145.4	152.7	153.7
Ni (XRF)	82.15	93.9	91.9	96.4

APPENDIX A: GEOCHEMICAL DATA

Major and Trace Element Abundances (continued)

Major elements	**Lunar Crater cone Basalt**			**Qc-cone Basalt**	
in wt. %	**LC10-96**	**LC17-96**	**LC54-97**	**LC18-96**	**LC33-96**
SiO_2	47.51	48.10	49.11	45.25	45.93
Al_2O_3	14.21	14.30	14.92	14.58	14.89
TiO_2	2.33	1.88	1.81	2.67	2.75
Fe_2O_3	13.89	12.76	12.22	13.10	13.16
MgO	6.15	8.89	8.92	8.75	8.18
CaO	8.45	8.90	1.16	9.77	8.80
Na_2O	2.81	2.87	0.17	2.83	3.33
K_2O	1.01	1.04	0.44	1.24	1.28
MnO	0.17	0.17	3.05	0.17	0.16
P_2O_5	0.45	0.39	9.34	0.58	0.57
Total	96.98	99.29	101.15	98.95	99.06
Mg#	46.7	58	60.2	57	55.2

Trace elements					
in ppm	**LC10-96**	**LC17-96**	**LC54-97**	**LC18-96**	**LC33-96**
Zr (XRF)	199.6	162.7		180.3	162.5
La (ICP-MS)		21.98		30.91	
Ce (ICP-MS)		43.02		61.43	
Pr (ICP-MS)		5.06		7.20	
Nd (ICP-MS)		22.22		30.06	
Sm (ICP-MS)		5.52		7.14	
Eu (ICP-MS)		1.87		2.41	
Gd (ICP-MS)		5.40		6.68	
Tb (ICP-MS)		0.88		1.06	
Dy (ICP-MS)		5.47		5.81	
Ho (ICP-MS)		1.05		1.10	
Er (ICP-MS)		2.75		2.84	
Tm (ICP-MS)		0.37		0.39	
Yb (ICP-MS)		2.21		2.29	
Lu (ICP-MS)		0.35		0.34	
Ba (XRF, ICP-MS)	297.3	300		411	
Th (ICP-MS)		1.98		2.72	
Nb (XRF)	23.81	24.84		44.12	51.95
Y (XRF)	31.66	27.41		28.12	34.56
Hf (ICP-MS)		4.10		4.33	
Ta (ICP-MS)		1.90		3.29	
U (ICP-MS)		0.64		0.89	
Pb (ICP-MS)		1.36		1.36	
Rb (XRF)	13.55	20.60		27.60	16.60
Cs (ICP-MS)		0.11		0.30	
Sr (XRF)	380.5	479		669	660.5
Sc (ICP-MS)		26.17		25.92	
Cr (XRF)	196.7	243.7	269.7	185.4	191.6
Ni (XRF)	119.1	179.3	212.4	135.0	120.5

APPENDIX A: GEOCHEMICAL DATA

Major and Trace Element Abundances (continued)

Major elements	Qc-cone Basalt				
in wt. %	**LC34-96**	**LC55-97**	**LC56-97**	**LC57-97**	**LC58-97**
SiO_2	47.27	47.45	46.47	46.04	46.33
Al_2O_3	14.66	15.08	15.52	15.46	14.66
TiO_2	2.40	2.46	2.89	2.88	2.47
Fe_2O_3	13.46	13.47	13.62	13.56	12.76
MgO	8.33	9.52	9.17	9.27	9.98
CaO	8.77	0.91	1.41	1.40	1.24
Na_2O	3.05	0.17	0.18	0.19	0.19
K_2O	1.01	0.38	0.60	0.63	0.46
MnO	0.17	3.13	3.31	3.07	2.94
P_2O_5	0.43	8.35	7.68	7.48	9.90
Total	99.55	100.93	100.85	99.98	100.92
Mg#	55.1	55.1	52.8	52.2	60.6

Trace elements					
in ppm	**LC34-96**	**LC55-97**	**LC56-97**	**LC57-97**	**LC58-97**
Zr (XRF)	149.1	136			156
La (ICP-MS)	21.75				
Ce (ICP-MS)	42.59				
Pr (ICP-MS)	5.18				
Nd (ICP-MS)	22.77				
Sm (ICP-MS)	5.98				
Eu (ICP-MS)	2.07				
Gd (ICP-MS)	5.91				
Tb (ICP-MS)	0.94				
Dy (ICP-MS)	5.52				
Ho (ICP-MS)	1.02				
Er (ICP-MS)	2.55				
Tm (ICP-MS)	0.33				
Yb (ICP-MS)	2.03				
Lu (ICP-MS)	0.31				
Ba (XRF, ICP-MS)	358				
Th (ICP-MS)	1.88				
Nb (XRF)	29.29	25.30			35.60
Y (XRF)	26.96	34.10			30.70
Hf (ICP-MS)	3.74				
Ta (ICP-MS)	2.17				
U (ICP-MS)	0.49				
Pb (ICP-MS)	1.01				
Rb (XRF)	18.80	13.80			22.30
Cs (ICP-MS)	0.18				
Sr (XRF)	505	471			571
Sc (ICP-MS)	24.31				
Cr (XRF)	194.0	231.7	190.6	215.2	243.8
Ni (XRF)	134.1	137.8	121.0	122.8	199.2

APPENDIX A: GEOCHEMICAL DATA

Major and Trace Element Abundances (continued)

Major elements	**C-cone Basalt**				
in wt. %	**LC14-96**	**LC22-96**	**LC27-96**	**LC28-96**	**LC29-96**
SiO_2	45.60	46.93	47.07	46.64	46.48
Al_2O_3	14.43	16.37	16.40	15.59	15.21
TiO_2	2.68	2.59	2.58	2.59	2.54
Fe_2O_3	12.52	12.37	12.19	12.36	12.57
MgO	8.10	6.24	6.34	7.18	8.23
CaO	10.01	8.90	8.78	8.92	9.07
Na_2O	3.46	3.66	3.70	3.49	3.36
K_2O	1.52	1.67	1.75	1.52	1.21
MnO	0.17	0.17	0.17	0.17	0.16
P_2O_5	0.73	0.62	0.59	0.59	0.52
Total	99.21	99.53	99.55	99.06	99.35
Mg#	56.2	50	50.7	53.5	56.5

Trace elements					
in ppm	**LC14-96**	**LC22-96**	**LC27-96**	**LC28-96**	**LC29-96**
Zr (XRF)	191.0	218.3	228.8	192.8	175.1
La (ICP-MS)					
Ce (ICP-MS)					
Pr (ICP-MS)					
Nd (ICP-MS)					
Sm (ICP-MS)					
Eu (ICP-MS)					
Gd (ICP-MS)					
Tb (ICP-MS)					
Dy (ICP-MS)					
Ho (ICP-MS)					
Er (ICP-MS)					
Tm (ICP-MS)					
Yb (ICP-MS)					
Lu (ICP-MS)					
Ba (XRF, ICP-MS)					
Th (ICP-MS)					
Nb (XRF)	48.82	66.37	65.56	43.17	52.31
Y (XRF)	39.04	40.64	39.54	39.92	37.86
Hf (ICP-MS)					
Ta (ICP-MS)					
U (ICP-MS)					
Pb (ICP-MS)					
Rb (XRF)	26.44	25.92	28.54	31.82	17.35
Cs (ICP-MS)					
Sr (XRF)	738.0	665.2	663.2	652.1	597.6
Sc (ICP-MS)					
Cr (XRF)	156.3	122.2	116.4	160.5	163.4
Ni (XRF)	109.9	79.99	82.91	98.28	135.2

APPENDIX A: GEOCHEMICAL DATA

Major and Trace Element Abundances (continued)

Major elements	C-cone Basalt				
in wt. %	**LC30-96**	**LC36-96**	**LC39-96**	**LC45-96**	**LC46-96**
SiO_2	46.52	46.31	46.41	46.94	45.03
Al_2O_3	15.65	15.57	15.62	15.02	14.56
TiO_2	2.58	2.66	2.67	2.48	2.76
Fe_2O_3	12.69	12.72	12.49	13.29	13.37
MgO	7.30	6.95	7.43	8.44	8.43
CaO	8.99	9.10	9.12	9.20	9.50
Na_2O	3.68	3.47	3.80	3.50	3.30
K_2O	1.42	1.52	1.48	1.17	1.49
MnO	0.17	0.18	0.17	0.17	0.18
P_2O_5	0.60	0.64	0.61	0.54	0.69
Total	99.57	99.12	99.79	100.74	99.31
Mg#	53.3	52	54.1	55.7	55.6

Trace elements					
in ppm	**LC30-96**	**LC36-96**	**LC39-96**	**LC45-96**	**LC46-96**
Zr (XRF)	191.3	198.6	190.4	160.1	197.1
La (ICP-MS)				25.53	
Ce (ICP-MS)				50.12	
Pr (ICP-MS)				6.09	
Nd (ICP-MS)				26.76	
Sm (ICP-MS)				6.64	
Eu (ICP-MS)				2.28	
Gd (ICP-MS)				6.46	
Tb (ICP-MS)				1.00	
Dy (ICP-MS)				5.97	
Ho (ICP-MS)				1.13	
Er (ICP-MS)				2.87	
Tm (ICP-MS)				0.38	
Yb (ICP-MS)				2.26	
Lu (ICP-MS)				0.35	
Ba (XRF, ICP-MS)				385	
Th (ICP-MS)				1.96	
Nb (XRF)	54.89	46.51	63.57	37.88	61.27
Y (XRF)	39.71	40.70	40.94	29.49	41.56
Hf (ICP-MS)				4.00	
Ta (ICP-MS)				2.64	
U (ICP-MS)				0.64	
Pb (ICP-MS)				1.08	
Rb (XRF)	17.06	28.17	22.23	21.30	21.40
Cs (ICP-MS)				0.18	
Sr (XRF)	637.6	685.4	650.3	613	729.4
Sc (ICP-MS)				25.91	
Cr (XRF)	134.0	144.9	139.9	182	151.4
Ni (XRF)	102.7	80.15	96.46	140.2	128.5

APPENDIX A: GEOCHEMICAL DATA

Major and Trace Element Abundances (continued)

Major elements	R-cone Basalt				
in wt. %	**LC23-96**	**LC37-96**	**LC50-97**	**LC51-97**	**LC52-97**
SiO_2	46.54	48.41	48.95	48.87	48.75
Al_2O_3	15.46	15.84	16.09	16.27	16.29
TiO_2	2.57	2.23	2.25	2.28	2.37
Fe_2O_3	13.07	12.20	12.14	12.21	12.45
MgO	7.68	7.05	8.51	8.43	8.44
CaO	9.21	8.49	1.75	1.75	1.74
Na_2O	3.39	3.93	0.17	0.17	0.17
K_2O	1.27	1.62	0.59	0.60	0.63
MnO	0.17	0.17	3.93	3.96	3.82
P_2O_5	0.52	0.62	6.55	6.69	6.38
Total	99.87	100.6	100.9	101.2	101.0
Mg#	53.8	53.4	51.7	52.1	50.4

Trace elements *in ppm*	**LC23-96**	**LC37-96**	**LC50-97**	**LC51-97**	**LC52-97**
Zr (XRF)	174.9	212.7	217	216	213
La (ICP-MS)		32.06			
Ce (ICP-MS)		60.99			
Pr (ICP-MS)		7.14			
Nd (ICP-MS)		29.56			
Sm (ICP-MS)		7.05			
Eu (ICP-MS)		2.33			
Gd (ICP-MS)		6.49			
Tb (ICP-MS)		1.03			
Dy (ICP-MS)		6.03			
Ho (ICP-MS)		1.15			
Er (ICP-MS)		2.96			
Tm (ICP-MS)		0.40			
Yb (ICP-MS)		2.35			
Lu (ICP-MS)		0.36			
Ba (XRF, ICP-MS)		451			
Th (ICP-MS)		3.09			
Nb (XRF)	50.92	44.41	46.00	46.50	46.40
Y (XRF)	36.32	30.56	40.90	42.10	41.60
Hf (ICP-MS)		5.08			
Ta (ICP-MS)		3.21			
U (ICP-MS)		0.80			
Pb (ICP-MS)		1.84			
Rb (XRF)	16.51	31.70	32.50	33.10	32.00
Cs (ICP-MS)		0.33			
Sr (XRF)	605.9	577	597	577	596
Sc (ICP-MS)		22.09			
Cr (XRF)	158.5	150.8	155.6	159.9	139.3
Ni (XRF)	134.1	97.80	126.9	114.8	65.62

APPENDIX A: GEOCHEMICAL DATA

Major and Trace Element Abundances (continued)

	Cinder cones around Citadel Mountain (Figures 4 and 6)				
Major elements	Marcath Flow	SKB	Blue Jay	cone N of LC	B-cone
in wt. %	**LC5-96**	**LC7-96**	**LC8-96**	**LC9-96**	**LC11-96**
SiO_2	42.95	43.84	44.92	43.25	43.50
Al_2O_3	14.33	14.39	15.49	14.19	13.50
TiO_2	2.56	2.83	3.19	2.86	2.66
Fe_2O_3	12.80	13.86	11.84	13.60	15.39
MgO	8.03	7.64	6.74	8.48	10.42
CaO	10.08	9.73	8.85	10.03	9.42
Na_2O	3.59	3.16	2.87	2.80	2.69
K_2O	1.93	1.49	1.59	1.32	0.71
MnO	0.19	0.18	0.16	0.17	0.18
P_2O_5	0.76	0.65	0.59	0.63	0.39
Total	97.22	97.79	96.24	97.33	98.85
Mg#	55.4	52.2	53	55.3	57.3

Trace elements					
in ppm	**LC5-96**	**LC7-96**	**LC8-96**	**LC9-96**	**LC11-96**
Zr (XRF)	269.2	213.5	262.7	186.9	123.7
La (ICP-MS)					16.72
Ce (ICP-MS)					34.03
Pr (ICP-MS)					4.23
Nd (ICP-MS)					19.16
Sm (ICP-MS)					5.26
Eu (ICP-MS)					1.88
Gd (ICP-MS)					5.38
Tb (ICP-MS)					0.84
Dy (ICP-MS)					4.77
Ho (ICP-MS)					0.92
Er (ICP-MS)					2.24
Tm (ICP-MS)					0.30
Yb (ICP-MS)					1.75
Lu (ICP-MS)					0.26
Ba (XRF, ICP-MS	580.5	424.8	340.1	385.6	227
Th (ICP-MS)					1.16
Nb (XRF)	68.64	47.25	47.88	46.69	24.64
Y (XRF)	25.07	24.18	20.64	21.32	23.78
Hf (ICP-MS)					2.82
Ta (ICP-MS)					1.85
U (ICP-MS)					0.36
Pb (ICP-MS)					0.95
Rb (XRF)	39.08	23.72	17.48	19.73	12.5
Cs (ICP-MS)					0.16
Sr (XRF)	946.2	722.2	802.4	702.3	518
Sc (ICP-MS)					26.62
Cr (XRF)	288.5				248.8
Ni (XRF)	168.3				260.7

APPENDIX A: GEOCHEMICAL DATA

Major and Trace Element Abundances (continued)

	Cinder cones around Citadel Mountain (Figures 4 and 6)					
Major elements	Smith Twins	cone S of CM	J-cone	J-cone	WKB	Smith Twins
in wt. %	**LC12-96**	**LC13-96**	**LC15-96**	**LC20-96**	**LC25-96**	**LC32-96**
SiO_2	43.42	45.05	47.36	48.24	49.05	45.13
Al_2O_3	14.32	14.82	14.98	15.45	15.89	14.02
TiO_2	3.11	2.54	2.39	2.24	2.24	2.76
Fe_2O_3	14.05	14.28	13.79	12.09	11.71	13.80
MgO	8.12	7.18	7.82	6.01	5.83	9.48
CaO	10.11	8.96	8.77	8.14	7.90	9.67
Na_2O	2.83	3.26	3.27	4.00	3.72	2.92
K_2O	1.29	1.37	1.14	1.58	1.73	1.25
MnO	0.17	0.19	0.17	0.17	0.16	0.18
P_2O_5	0.52	0.62	0.49	0.59	0.59	0.55
Total	97.94	98.26	100.2	98.49	98.83	99.75
Mg#	53.4	49.9	52.9	49.6	49.7	57.7

Trace elements ***in ppm***	**LC12-96**	**LC13-96**	**LC15-96**	**LC20-96**	**LC25-96**	**LC32-96**
Zr (XRF)	178.2	185.8	158.6	229.0	240.3	156.5
La (ICP-MS)						
Ce (ICP-MS)						
Pr (ICP-MS)						
Nd (ICP-MS)						
Sm (ICP-MS)						
Eu (ICP-MS)						
Gd (ICP-MS)						
Tb (ICP-MS)						
Dy (ICP-MS)						
Ho (ICP-MS)						
Er (ICP-MS)						
Tm (ICP-MS)						
Yb (ICP-MS)						
Lu (ICP-MS)						
Ba (XRF, ICP-MS)	360.3	317.7				
Th (ICP-MS)						
Nb (XRF)	40.82	40.50	33.51	57.24	45.21	39.17
Y (XRF)	22.97	22.99	37.07	43.10	43.79	36.88
Hf (ICP-MS)						
Ta (ICP-MS)						
U (ICP-MS)						
Pb (ICP-MS)						
Rb (XRF)	18.33	19.66	19.27	26.93	31.31	22.60
Cs (ICP-MS)						
Sr (XRF)	655.9	535.5	544.4	514.9	547.0	628.6
Sc (ICP-MS)						
Cr (XRF)			186.5	117.3	122.9	219.0
Ni (XRF)			123.5	82.27	81.57	160.3

APPENDIX A: GEOCHEMICAL DATA

Major and Trace Element Abundances (continued)

	Cinder cones around Citadel Mountain (Figures 4 and 6)			
Major elements	cone E of LC	ECC	Lunar Lake maar	Spatter Rampart
in wt. %	**LC35-96**	**LC41-96**	**LC42-96**	**LC53-97**
SiO_2	46.27	45.87	46.26	49.64
Al_2O_3	14.93	14.99	15.08	15.65
TiO_2	2.63	2.43	2.46	2.69
Fe_2O_3	13.32	11.62	14.74	13.33
MgO	7.49	8.10	7.37	8.48
CaO	8.88	9.03	8.90	1.21
Na_2O	3.58	3.59	3.62	0.17
K_2O	1.33	1.65	1.19	0.55
MnO	0.17	0.16	0.19	3.58
P_2O_5	0.58	0.59	0.85	5.83
Total	99.17	98.02	100.6	101.1
Mg#	52.7	58	49.8	46.4

Trace elements *in ppm*	**LC35-96**	**LC41-96**	**LC42-96**	**LC53-97**
Zr (XRF)	185.8	200.8	168.5	
La (ICP-MS)				
Ce (ICP-MS)				
Pr (ICP-MS)				
Nd (ICP-MS)				
Sm (ICP-MS)				
Eu (ICP-MS)				
Gd (ICP-MS)				
Tb (ICP-MS)				
Dy (ICP-MS)				
Ho (ICP-MS)				
Er (ICP-MS)				
Tm (ICP-MS)				
Yb (ICP-MS)				
Lu (ICP-MS)				
Ba (XRF, ICP-MS)				
Th (ICP-MS)				
Nb (XRF)	49.04	65.35	55.15	
Y (XRF)	38.78	36.53	43.68	
Hf (ICP-MS)				
Ta (ICP-MS)				
U (ICP-MS)				
Pb (ICP-MS)				
Rb (XRF)	18.62	29.50	14.95	
Cs (ICP-MS)				
Sr (XRF)	594.7	657.7	748.9	
Sc (ICP-MS)				
Cr (XRF)	132.3	171.1	128.1	155.5
Ni (XRF)	104.3	134.4	100.7	100.4

APPENDIX A: GEOCHEMICAL DATA

Major and Trace Element Abundances (continued)

Major elements	Tertiary Andesites		Tuff of Lunar Cuesta	Basaltic Andesites	
in wt. %	LC2-95	LC3-95	LC6-96	LC31-96	LC43-96
SiO_2	64.34	65.49	72.48	54.94	54.38
Al_2O_3	15.47	15.90	14.94	16.94	16.73
TiO_2	0.85	0.68	0.36	1.60	1.58
Fe_2O_3	5.10	5.18	2.37	9.44	9.49
MgO	1.59	1.53	0.75	4.11	4.25
CaO	3.78	3.71	2.53	7.89	7.84
Na_2O	3.24	3.44	3.21	2.97	2.93
K_2O	3.83	3.84	4.19	1.57	1.62
MnO	0.10	0.10	0.05	0.13	0.13
P_2O_5	0.31	0.30	0.09	0.43	0.39
Total	98.60	100.2	101.0	100.0	99.33
Mg#	38.1	36.9	38.6	46.3	47

Trace elements					
in ppm	LC2-95	LC3-95	LC6-96	LC31-96	LC43-96
Zr (XRF)	298.8	309.0	211.2	233.5	233.3
La (ICP-MS)	55.09			35.93	
Ce (ICP-MS)	105.2			71.09	
Pr (ICP-MS)	11.7			8.65	
Nd (ICP-MS)	44.64			35.37	
Sm (ICP-MS)	9.03			7.81	
Eu (ICP-MS)	2.08			2.11	
Gd (ICP-MS)	7.03			6.79	
Tb (ICP-MS)	1.06			1.00	
Dy (ICP-MS)	6.10			5.79	
Ho (ICP-MS)	1.16			1.14	
Er (ICP-MS)	3.01			2.97	
Tm (ICP-MS)	0.44			0.41	
Yb (ICP-MS)	2.71			2.57	
Lu (ICP-MS)	0.43			0.41	
Ba (XRF, ICP-MS)	1092			718	
Th (ICP-MS)	12.16			4.79	
Nb (XRF)	18.90	19.19	7.62	12.75	16.36
Y (XRF)	32.41	44.99	16.67	30.64	34.88
Hf (ICP-MS)	7.36			5.76	
Ta (ICP-MS)	2.14			1.21	
U (ICP-MS)	3.04			1.11	
Pb (ICP-MS)	20.00			6.22	
Rb (XRF)	117.5	127.4	138.4	42.90	53.62
Cs (ICP-MS)	2.88			0.81	
Sr (XRF)	630	626.2	510.4	659	610.4
Sc (ICP-MS)	9.63			24.01	
Cr (XRF)	13.72	12.61	8.85	38.42	8.83
Ni (XRF)	48.41	48.41	48.41	48.41	ND

*1. Totals do not include LOI.

*2. XRF = X-ray Fluorescence Spectrometer

*3. ICP-MS = Inductively Coupled Plasma - Mass Spectrometer

APPENDIX A: GEOCHEMICAL DATA

Precision and Accuracy

Primary calibration standards for the Rigaku 3030 X-ray Fluorescence Spectrometer. Standards are United States Geological Survey, National Bureau of Standards and French standards.

Major Elements	Trace Elements
DNC-1	G-2
BHVO-1	W-2
PCC-1	BIR-1
AGV-1	BHVO-1
GS-N	DNC-1
GA	RGM-1
W-2	QLO-1
BR	PCC-1
SCo-1	SCo-1
STM-1	AGV-1
GSP-1	GSP-1
RGM-1	AN-G
QLO-1	DR-N
AL-1	GS-N
	MAG-1
	Mica Mg
	NBS-688

Accuracy for the Rigaku 3030 X-ray Fluorescence Spectrometer using NBS standard NBS-688 (major elements), USGS standard MAG-1 (trace elements) and Rh X-ray tube installed Aug. 1994.

Element	% error
SiO_2	0.7
Al_2O_3	0.5
TiO_2	0.7
Fe_2O_3	2.6
MgO	2.4
CaO	1.5
Na_2O	0.9
K_2O	2.3
MnO	8.2
P_2O_5	18.6 ← !!
Rb	0.9
Sr	2.1
Zr	1.8
Y	11.2
Nb	13.3
Cr	27.5
Ni	3.5

APPENDIX A: GEOCHEMICAL DATA

Precision and Accuracy (continued)

Precision for the Rigaku 3030 X-ray Fluorescence Spectrometry.
Precision is determined using NBS standard NBS-688 (major elements),
USGS standard MAG-1 (trace elements) and Rh X-ray tube installed Aug. 1994.

Element	Published concentration	Mean of 4 replicate analyses	Standard deviation	uncertainty
SiO_2	50.36	47.99	0.45	0.9
Al_2O_3	16.37	17.44	0.2	1.2
TiO_2	0.751	1.16	0.02	1.8
Fe_2O_3	6.8	10.07	0.14	1.3
MgO	3.0	8.66	0.15	1.7
CaO	1.37	11.99	0.11	0.9
Na_2O	3.83	2.14	0.06	2.6
K_2O	3.55	0.186	0.003	1.4
MnO	0.098	0.153	0.005	3.2
P_2O_5	0.163	0.158	0.018	11.4
Rb	149	150.4	4.33	2.9
Sr	146	143	3.11	2.2
Zr	126	128.3	2.22	1.7
Y	28	31.14	2.65	8.5
Nb	12	13.6	2.44	17.9 ←
Cr	97	70.3	4.57	6.5
Ni	53	51.1	2.39	4.7

% or ppm or ??

20% / ppm ?

APPENDIX A: GEOCHEMICAL DATA

Precision and Accuracy (continued)

Accuracy for the Inductively Coupled Plasma - Mass Spectrometer (ICP-MS). U.S.G.S. standard BHVO-1 was used as a reference.

Element ppm	Published value	WSU ICP-MS value	% error
Ba	139	133	4.32
La	15.8	15.65	0.95
Ce	39	37.07	4.95
Sm	6.2	6.2	0
Eu	2.06	2.12	2.91
Tb	0.96	0.96	0
Yb	2.02	2.02	0
Lu	0.29	0.28	3.45
Hf	4.38	4.34	0.91
Ta	1.23	1.25	1.63
Th	1.08	1.25	15.74

Precision for the Inductively Coupled Plasma - Mass Spectrometer (ICP-MS). Data reported is from twenty-four replicate analysis of Washington State in-house standards BCR-P.

Element ppm	Mean of 24 replicate analysis	Standard deviation	Mean relative % error
Ba	670	13	1.89
La	26.26	0.49	1.86
Ce	51.67	0.62	1.2
Sm	7.03	0.15	2.07
Eu	2.13	0.05	2.48
Tb	1.17	0.01	1.12
Yb	3.36	0.03	0.94
Lu	0.52	0.01	1.9
Hf	4.67	0.07	1.47
Ta	0.82	0.02	2.7
Th	5.13	0.49	9.5

APPENDIX B: GEOCHEMICAL DATA

Sr, Nd and Pb Isotopic Ratios

	Sample	Nd (ppm)	^{147}Sm/^{144}Nd	Error	^{143}Nd/^{144}Nd	Error	ε_{Nd}	Error	^{87}Sr/^{86}Sr	% error
TA	LC2-95	37.9048	0.10789	±0.00111	0.512278	±0.000027	-7.03	±0.37	0.708368	0.0014
B	LC11-96	21.7192	0.14586	±0.00139	0.512905	±0.000025	5.20	±0.34	0.703200	0.0013
Pl	LC16-96	23.6129	0.14139	±0.00146	0.512871	±0.000018	4.55	±0.25	0.703650	0.0010
Lc	LC17-96	23.1495	0.13484	±0.00140	0.512810	±0.000015	3.35	±0.21	0.704728	0.0011
Qc	LC18-96	26.3975	0.12740	±0.00142	0.512928	±0.000015	5.66	±0.21	0.703253	0.0010
Pl	LC24-96	31.1509	0.14009	±0.00149	0.512837	±0.000015	3.88	±0.21	0.703910	0.0015
C	LC27-96	35.7237	0.12527	±0.00146	0.512922	±0.000015	5.55	±0.21	0.703379	0.0013
BA	LC31-96	36.3462	0.12066	±0.00138	0.512247	±0.000015	-7.63	±0.21	0.707650	0.0010
Qc	LC34-96	25.9124	0.14140	±0.00156	0.512919	±0.000015	5.49	±0.21	0.703313	0.0009
R	LC37-96	33.7308					5.29	±0.23	0.703351	0.0016
H	LC38-96	25.8101	0.14419	±0.00139	0.512766	±0.000015	2.49	±0.21	0.704802	0.0017
BA	LC43-96	37.6565	0.11820	±0.00121	0.512265	±0.000015	-7.27	±0.21	0.707617	0.0013
C	LC45-96	23.0977	0.13384	±0.00140	0.512933	±0.000015	5.76	±0.21	0.703311	0.0010

APPENDIX B: GEOCHEMICAL DATA

Sr, Nd and Pb Isotopic Ratios (continued)

Sample	Pb (ppm)	$^{206}Pb/^{204}Pb$	Error (± %)	$^{207}Pb/^{204}Pb$	Error (± %)	$^{208}Pb/^{204}Pb$	Error (± %)
LC2-95	18.715	19.291	0.1	15.690	0.15	39.142	0.2
LC11-96	827.39	19.482	0.101	15.634	0.151	38.948	0.201
LC16-96	1.6643	19.400	0.108	15.663	0.156	39.043	0.204
LC17-96	1.6021	19.375	0.101	15.653	0.151	39.005	0.201
LC18-96	1.2462	19.370	0.101	15.614	0.151	38.825	0.201
LC24-96	1.9147	19.404	0.101	15.668	0.151	39.071	0.201
LC27-96	1.8956	19.422	0.103	15.599	0.152	38.852	0.202
LC31-96	6.7581	18.753	0.101	15.626	0.15	38.976	0.2
LC34-96	1.3096	19.431	0.128	15.621	0.171	38.938	0.216
LC37-96	2.0286	19.475	0.101	15.633	0.151	38.999	0.201
LC38-96	2.2282	19.354	0.101	15.664	0.151	39.033	0.201
LC43-96	5.5268	18.761	0.101	15.645	0.15	39.037	0.2
LC45-96	1.3914	19.428	0.107	15.609	0.155	38.857	0.204

APPENDIX C

GEOCHRONOLOGY

$^{40}Ar/^{39}Ar$ Analytical Techniques

use Block Quote format

The following description of analytical techniques was provided by Richard Esser and Matthew Heizler of New Mexico Geochronological Research Laboratory (NMGRL). "The whole rock samples were crushed, sieved, treated with dilute HCL, washed in distilled water and hand-picked to remove phenocrysts, weathered material, etc., leaving as pure a groundmass concentrate as possible. They were then placed in a machined Al disc and sealed in an evacuated Pyrex tube along with interlaboratory standard Fish Canyon Tuff (Age = 27.84 Ma). The standard was used to monitor the neutron dose received during the 1 hour irradiation in the D-3 position of the reactor at the Nuclear Science Center, College Station, TX. The whole rock samples were step-heated in a double vacuum Mo resistance furnace. The gas was cleaned during heating with a SAES GP-50 getter, and additionally cleaned following heating with another GP-50. The flux monitor crystals were placed in a copper planchet and fused within an ultra-high vacuum argon extraction system with a 10W Synrad CO_2 continuous laser. Evolved gases were purified for two minutes using a SAES GP-50 getter operated at ~450° C. Argon isotopic compositions for both samples and monitors were determined with a MAP 215-50 mass spectrometer operated in electron multiplier mode with an overall sensitivity of approximately 3.0×10^{-17} moles/pA. Extraction system and mass spectrometer blanks and backgrounds were measured numerous times throughout the course of the analyses. Typical blanks (including mass spectrometer backgrounds) were; 570, 4, 0.3, 0.8, 2.6×10^{-18} moles at masses 40, 39, 38, 37, 36 respectively. J-factors were determined to a precision of 0.10% by analyzing 4 single-crystal aliquots from each of 4 radial positions around the irradiation vessel. Correction for interfering nuclear reactions were determined using K-glass and CaF_2. These values are $(^{40}Ar/^{39}Ar)_K = 0.0002 \pm 0.0002$, $(^{36}Ar/^{37}Ar)_{Ca} = 0.00026 \pm 0.00002$ and $(^{39}Ar/^{37}Ar)_{Ca} = 0.00070 \pm 0.00005$. All errors are reported at the two sigma confidence level and the decay constant and isotopic abundances are those suggested by Steiger and Jager (1977)."

Summary of $^{40}Ar/^{39}Ar$ Results

The following results and discussion were provided by Richard Esser and Matthew Heizler of New Mexico Geochronological Research Laboratory (NMGRL). "Age spectra diagrams are given for each sample and a table of the analytical data is also provided. The age spectrum is generated by incrementally heating the sample starting at relatively low temperature and raising the temperature until the sample is fused. The argon isotopic composition of each gas increment is measured in a mass spectrometer and an apparent age is calculated. The apparent age of each gas fraction is plotted versus the cumulative $\%^{39}Ar$. When all apparent ages are the same within analytical error, the sample is said to have a plateau spectrum. A plateau age spectrum usually indicates that the sample is homogeneous with respect to K and Ar and has had a simple thermal and geological history. Commonly, not all heating steps will yield identical ages, but a plateau is defined if 3 or more contiguous heating steps, comprising at least 50% of the ^{39}Ar agree within error (Fleck, et al., 1997). The plateau age is calculated in various ways, but in this report is given by weighting each step on the plateau by the inverse of its variance (Samson and Alexander, 1987). This insures that the heating steps with the lowest analytical error will dominate the final age calculation. Excess argon (initial argon trapped within the sample which has an $^{40}Ar/^{36}Ar$ ratio greater than the atmospheric value of 295.5) contributed by one or more phases of a wholerock or groundmass separate can result in disturbed age spectra particularly at the lowest and highest temperature steps. In order to test for excess argon, the analyses were plotted on isochron diagrams. The diagram plots the measured $^{36}Ar/^{40}Ar$ versus the $^{39}Ar/^{40}Ar$ ratio and is often a better method (relative to the age spectrum) of data handling as there is no need to assume an initial argon composition. In fact, the isochron can provide a quantitative measure of the initial argon composition. However, in the case of the LC wholerocks, isochron analysis does not indicate significant excess argon contamination. Therefore, in each case, the plateau age is interpreted to represent the eruption age of the basalts."

USE BLOCK QUOTE

Sample	age analysis	n	$\%^{39}Ar$	MSWD	$^{40}Ar/^{36}Ar_i$	±Err	K/Ca	Age	±2σ
LC37-96	isochron	7		0.5	306.7	7.0	0.5	0.66	0.34
LC40-96	plateau	4	73.6				0.5	3.82	0.06
LC17-96	isochron	8		1.2	298.7	2.6	0.3	2.97	0.06
LC43-96	isochron	7		0.7	291.2	3.6	0.2	21.79	0.36
LC38-96	plateau	5	74.5				0.3	3.82	0.05
LC18-96	N.A.						N.A.	N.A.	N.A.
LC45-96	plateau	5	86.9				0.5	1.56	0.64

Where n = number of steps in step heating of the sample.

Results and Discussion

<u>LC37-96</u> (R-cone flow) has a discrepancy between its plateau age and isochron age. The lowest (step A) and highest (step I) temperature steps have higher apparent ages forming a "saddle-shaped" age spectrum. Almost 91% of the ^{39}Ar was released during steps B through H, and each step yields concordant age data. The apparent age of the inverse isochron is 0.66 ± 0.34 Ma. The larger margin of error is due to the clustering of data points on the inverse isochron, however because a "saddle-shaped" age spectrum indicates excess argon, the inverse isochron age is the best estimate for the eruption of the R-cone flow.

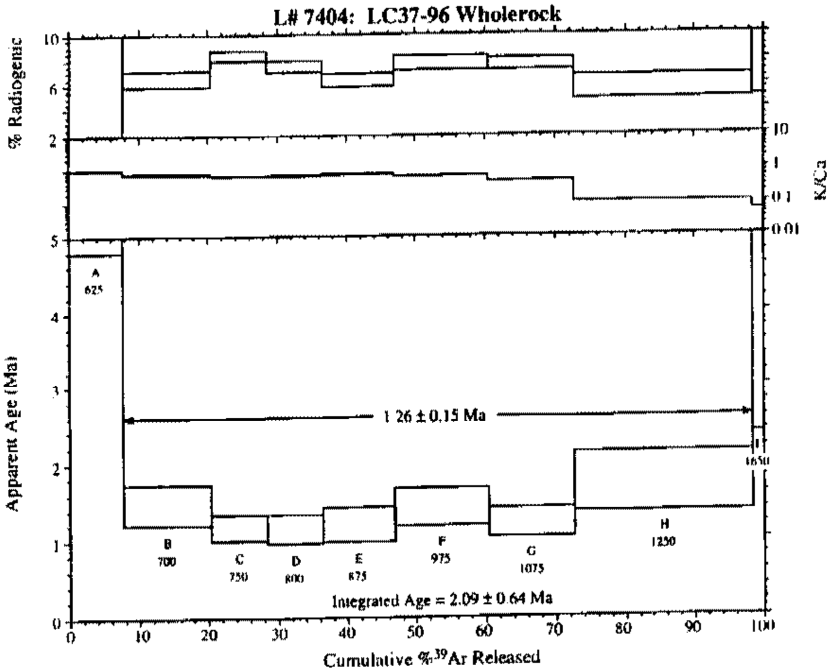

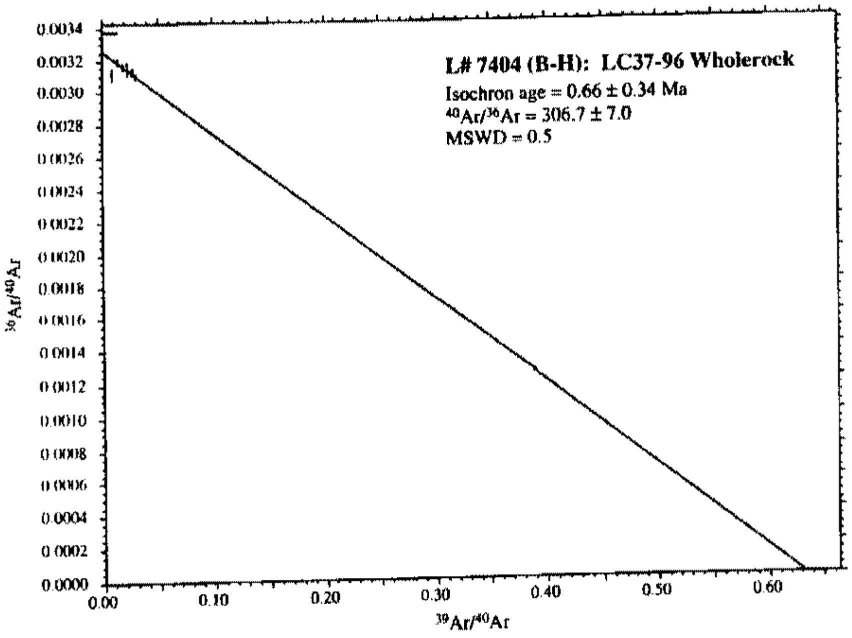

LCAD40-96 (P1-cone flow) also has a saddle-shaped age spectrum, however the isochron does not indicate significant quantities of trapped ^{36}Ar. The trapped Ar appears to be essentially equal to that of atmosphere (295.5) so the plateau and isochron ages are equivalent. The isochron data points are scattered so the plateau age (3.82 ± 0.06 Ma) is the best estimate for the eruption of the P1-cone flow.

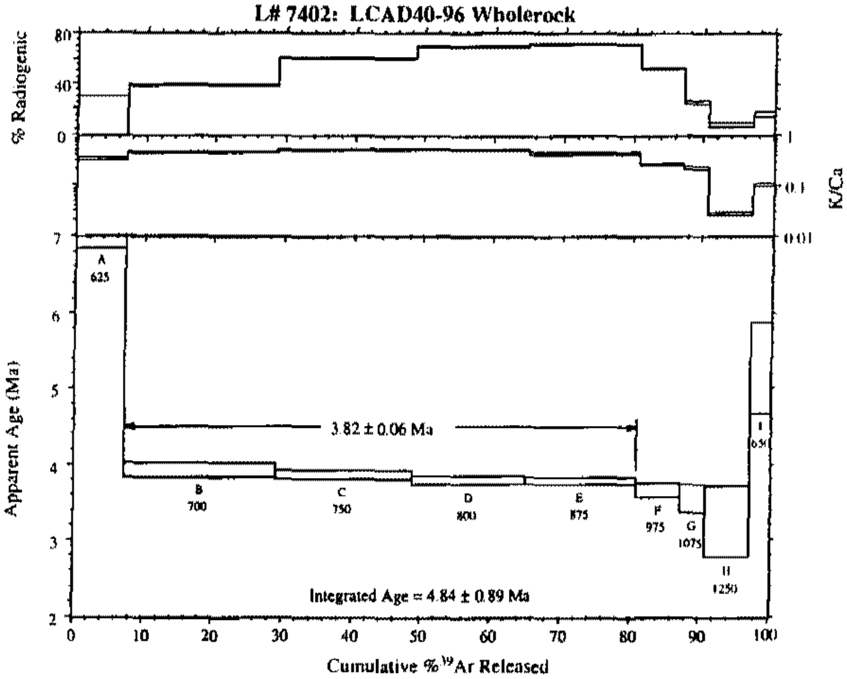

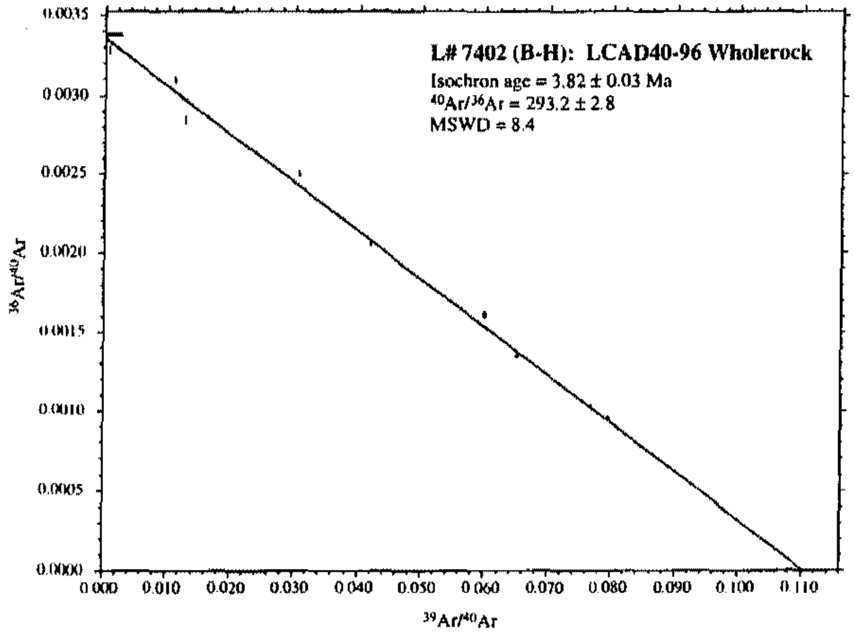

<u>LC17-96</u> (Lunar Crater flow) shows a saddle-shaped age spectrum but the inverse isochron suggests that the trapped $^{40}Ar/^{36}Ar$ component is not significantly above atmosphere. The goodness of fit measure, MSWD is below 2.0, which indicates statistically meaningful results. Therefore, the isochron age of 2.97 ± 0.06 Ma is the preferred eruption age of the Lunar Crater flow.

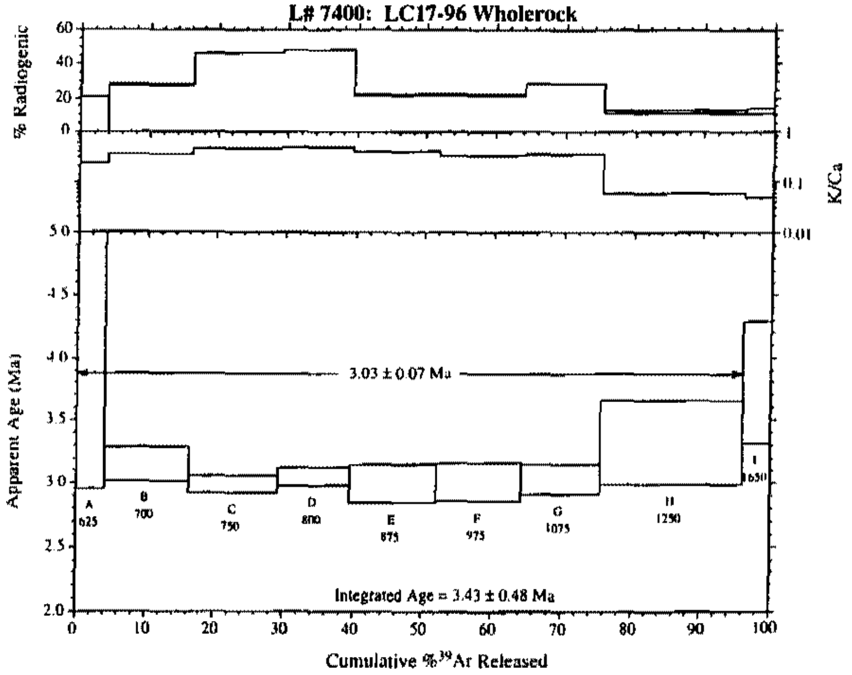

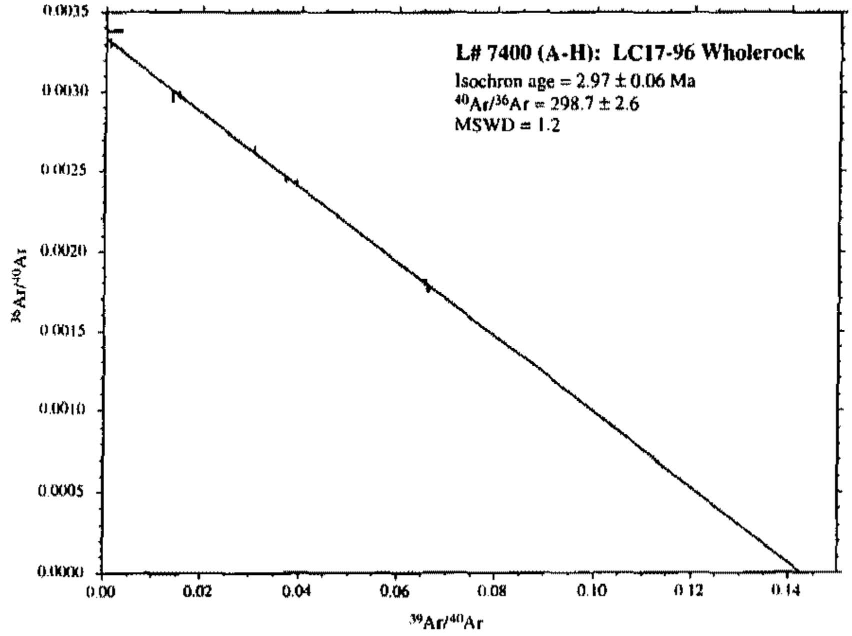

LCAD43-96 (Basaltic andesite) has a much more discordant age spectrum than other Lunar Crater samples. Although the age spectrum is disturbed, a plateau age of 21.43 ± 0.32 Ma can be calculated. This apparent age is analytically equivalent to the isochron age of 21.79 ± 0.36 Ma indicating that excess argon is not present in significant quantities. The isochron age is the preferred age estimate for the eruption of the basaltic andesites.

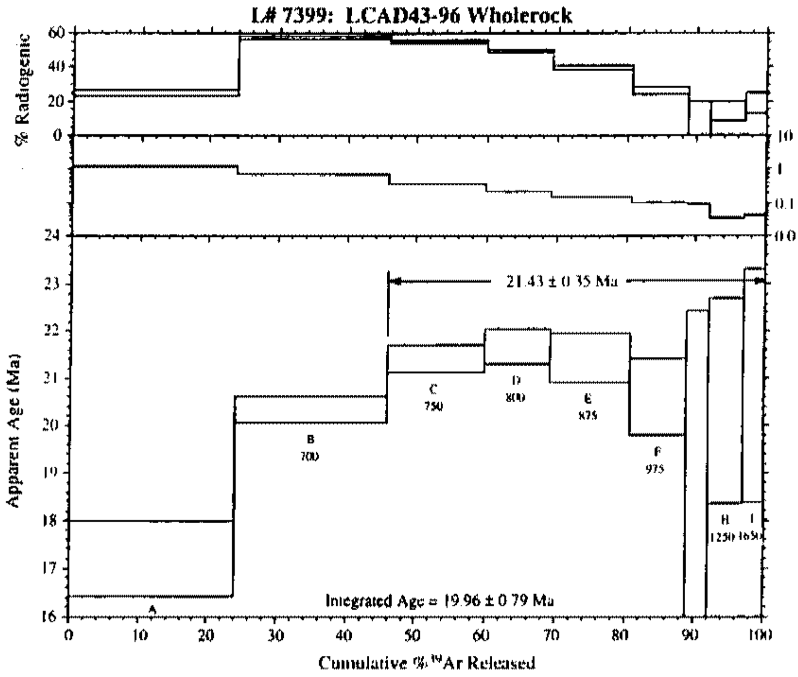

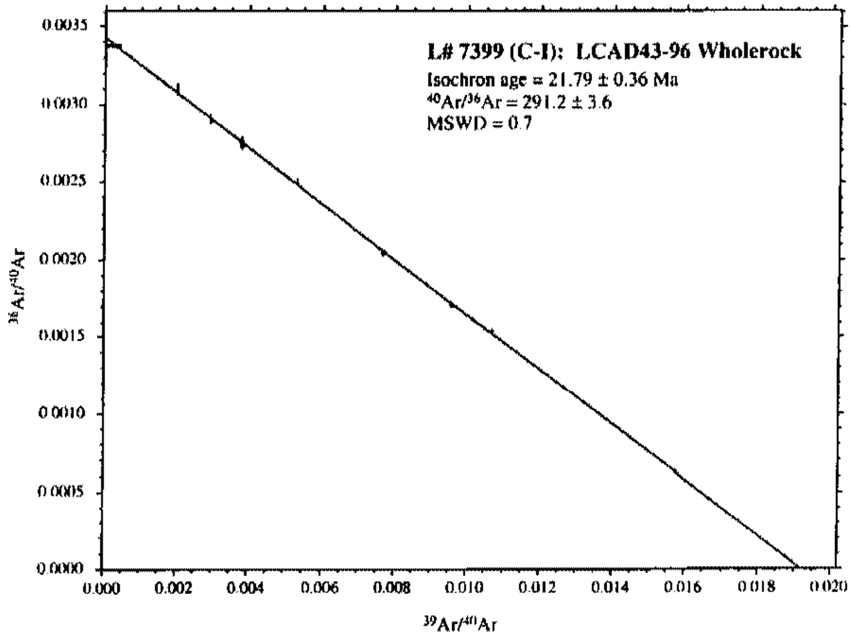

LC38-96 (H-cone flow) has an age spectrum and isochron very similar to those for LCAD40-96 (P1-cone flow). The isochron has a MSWD greater than two so the plateau age (3.82 ± 0.05 Ma) is the preferred estimate for the eruption of the H-cone flow.

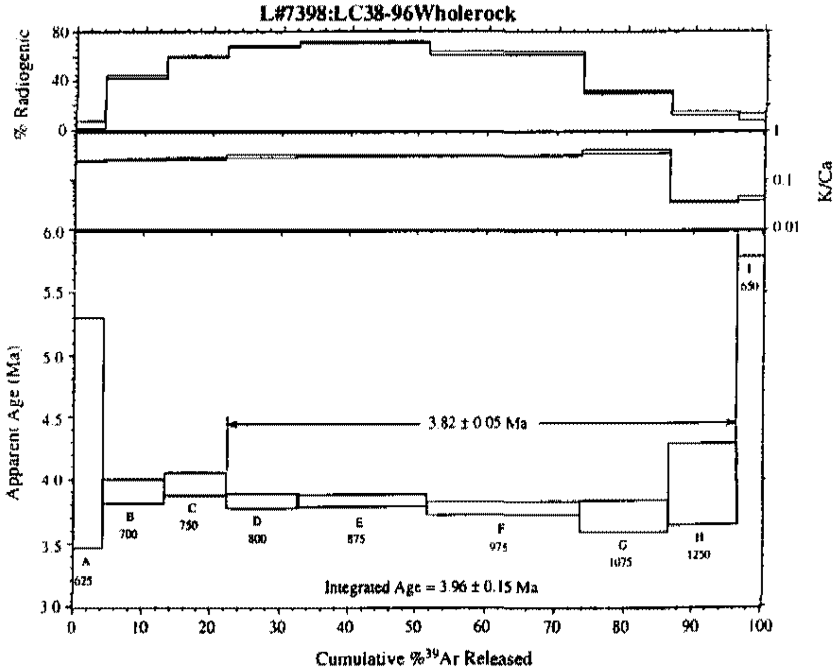

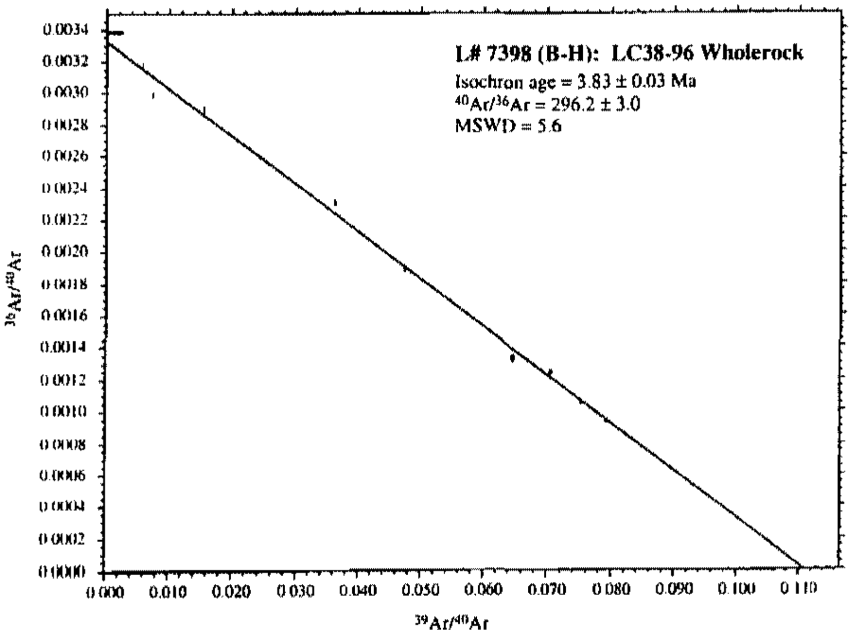

LC18-96 (Qc-cone flow) has extreme atmospheric contamination and was aborted after two heating steps.

LC45-96 (C-cone flow) has an age spectrum and isochron that appear reasonable with respect to plateau and MSWD, however the $^{40}Ar/^{39}Ar$ analysis itself was poor. Some basalts contain large quantities of atmospheric argon that can be detrimental to the mass spectrometer. Six steps were obtained for the sample, but the data quality did not improve and the sample was aborted. The six steps yield a plateau age of 1.56 ± 0.64 Ma and an isochron age of 0.39 ± 0.64 Ma, however due to the large uncertainty, it is not appropriate to assign an eruption age for the C-cone flow.

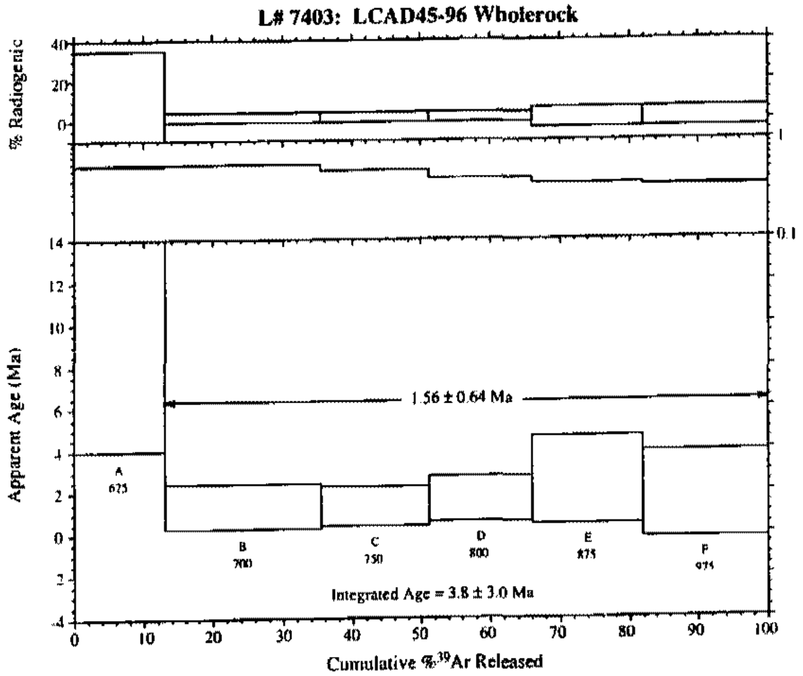

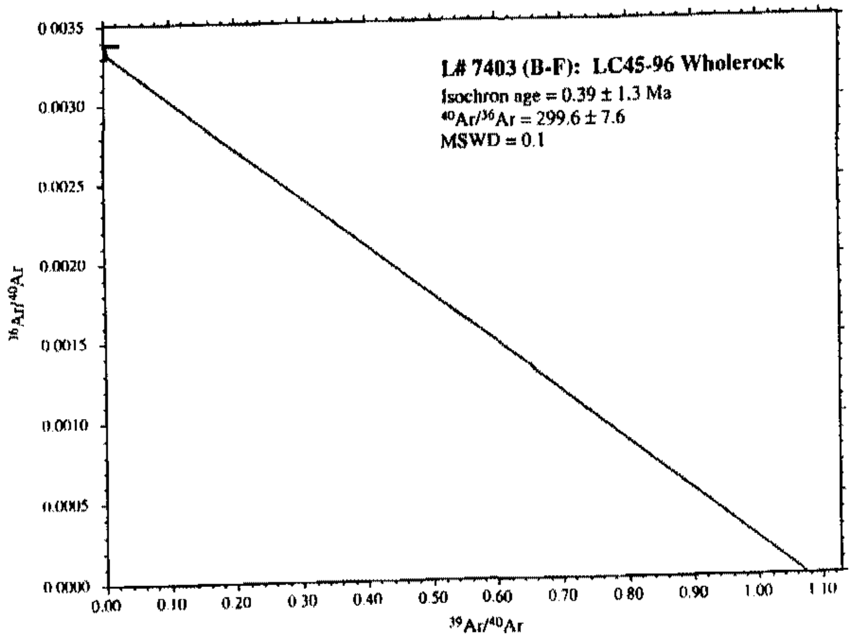

APPENDIX D: SAMPLE LOCATIONS FOR GEOCHEMICAL DATA

Sample #	Sample Description	Latitude	Longitude
LC2-95	Tertiary andesites		
LC3-95	Tertiary andesites		
LC5-96	Marcath Flow		
LC6-96	Tuff of Lunar Cuesta		
LC7-96	South Kidney Butte		
LC8-96	BlueJay basalt flow		
LC9-96	cone north of Lunar Crater		
LC10-96	Lunar Crater flow		
LC11-96	B-cone flow		
LC12-96	Smith Twins flow		
LC13-96	cone south of Citadel Mountain		
LC14-96	C-cone flow		
LC15-96	J-cone lava lake material		
LC16-96	P1-cone flow at Lunar Crater		
LC17-96	Lunar Crater flow in crater		
LC18-96	Qc-cone flow at Lunar Crater		
LC19-96	P1-cone flow		
LC20-96	J-cone flow		
LC21-96	P1-cone at vent (dike)		
LC22-96	C-cone flow		
LC23-96	R-cone flow		
LC24-96	P1-cone flow		
LC25-96	West Kidney Butte		
LC26-96	P1-cone flow		
LC27-96	C-cone flow		
LC28-96	C-cone flow		
LC29-96	C-cone flow		
LC30-96	C-cone flow		

not complete

APPENDIX D: SAMPLE LOCATIONS FOR GEOCHEMICAL DATA

Sample #	Sample Description	Latitude	Longitude
LC31-96	Basaltic andesite		
LC32-96	Smith Twins flow		
LC33-96	Qc-cone flow		
LC34-96	Qc-cone flow		
LC35-96	cone east of Lunar Crater		
LC36-96	C-cone flow		
LC37-96	R-cone flow		
LC38-96	H-cone flow		
LC39-96	C-cone flow		
LCAD40-96	P1-cone flow		
LC41-96	Easy Chair Crater maar		
LC42-96	Lunar Lake maar		
LCAD43-96	Basaltic andesite		
LC44-96	P1-cone flow		
LC45-96	C-cone flow		
LC46-96	C-cone flow		
LC47-97	H-cone flow		
LC48-97	H-cone flow		
LC49-97	H-cone flow		
LC50-97	R-cone flow		
LC51-97	R-cone flow		
LC52-97	R-cone flow		
LC53-97	Small spatter rampart		
LC54-97	Lunar Crater cone basalt		
LC55-97	Qc-cone flow		
LC56-97	Qc-cone flow		
LC57-97	Qc-cone flow		
LC58-97	Qc-cone flow		

APPENDIX D: SAMPLE LOCATIONS FOR GEOCHEMICAL DATA

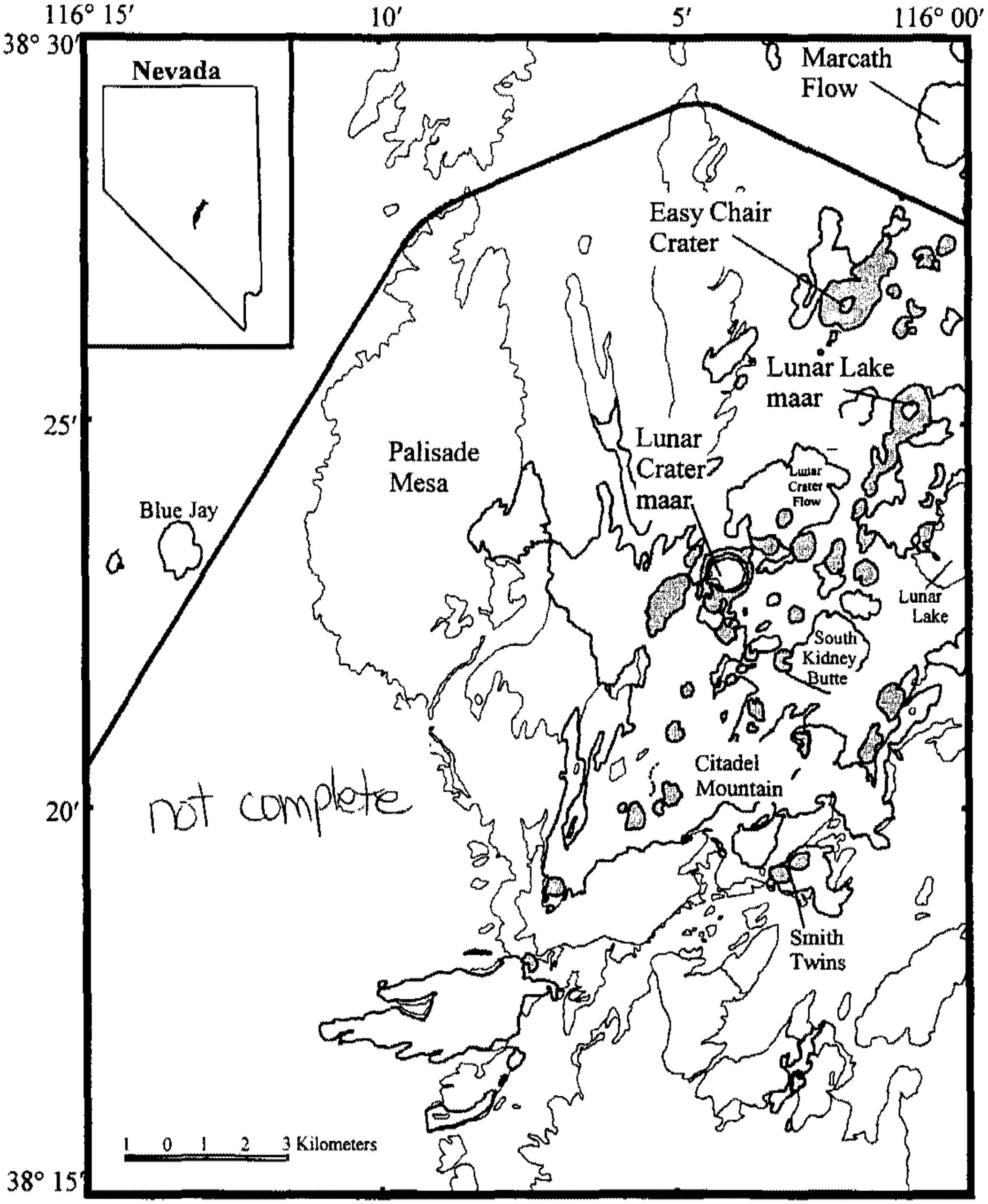

not complete

Figure D1. Lunar Crater quadrangle map after Ekren et al. (1972). Map shows the location of samples collected in the LCVF for geochemical data.

APPENDIX ~~E~~ D: SAMPLE LOCATIONS FOR GEOCHEMICAL DATA

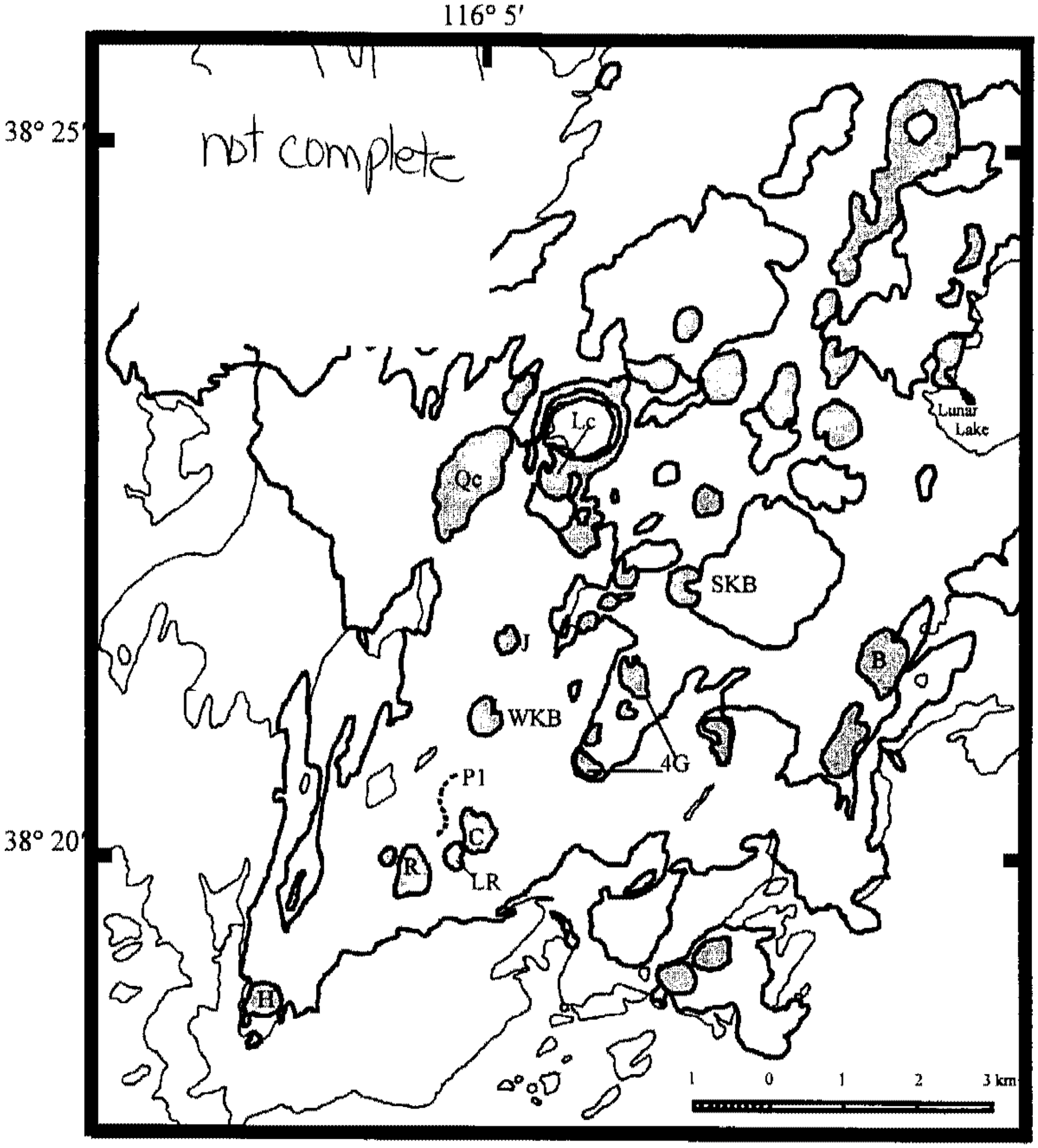

Figure D2. Map shows the location of samples collected on Citadel Mountain for geochemical data, after Ekren et al. (1972).